12-2008

Structural and Magnetic Properties of Manganites $Pr_{1-x}Ca_{1+x}MnO_4$, Oxypnictides $CeFeAsO_{1-x}F_x$, and Filled Skutterudite $PrOs_4As_{12}$

Songxue Chi
University of Tennessee - Knoxville

To the Graduate Council:

I am submitting herewith a dissertation written by Songxue Chi entitled "Structural and Magnetic Properties of Manganites $Pr_{1-x}Ca_{1+x}MnO_4$, Oxypnictides $CeFeAsO_{1-x}F_x$, and Filled Skutterudite $PrOs_4As_{12}$." I have examined the final electronic copy of this dissertation for form and content and recommend that it be accepted in partial fulfillment of the requirements for the degree of Doctor of Philosophy, with a major in Physics.

Pengcheng Dai, Major Professor

We have read this dissertation and recommend its acceptance:

Elbio Dagotto, Norman Mannella, Takeshi Egami, Jaime A. Fernandez-Baca

Accepted for the Council:

Carolyn R. Hodges

Vice Provost and Dean of the Graduate School

(Original signatures are on file with official student records.)

To the Graduate Council:

I am submitting herewith a dissertation written by Songxue Chi entitled "Structural and magnetic properties of manganites $Pr_{1-x}Ca_{1+x}MnO_4$, oxypnictides $CeFeAsO_{1-x}F_x$, and filled skutterudite $PrOs_4As_{12}$." I have examined the final electronic copy of this dissertation for form and content and recommend that it be accepted in partial fulfillment of the requirements for the degree of Doctor of Philosophy, with a major in Physics.

Pengcheng Dai

Major Professor

We have read this dissertation
and recommend its acceptance:

Elbio Dagotto

Norman Mannella

Takeshi Egami

Jaime A. Fernandez-Baca

Accepted for the Council:

Carolyn R. Hodges
Vice Provost
and Dean of the Graduate School

(Original signatures are on file with official student records.)

Structural and magnetic properties of manganites $Pr_{1-x}Ca_{1+x}MnO_4$, oxypnictides $CeFeAsO_{1-x}F_x$, and filled skutterudite $PrOs_4As_{12}$

A Dissertation

Presented for the

Doctor of Philosophy

Degree

The University of Tennessee, Knoxville

Songxue Chi

December 2008

Dedication

To my wife Xuehua and my parents.

Acknowledgments

First I wish to express my gratitude to my supervisor, Professor Pengcheng Dai. His extraordinary passion for research, weariless endeavor, great knowledge and resourcefulness have been such a inspiration. I want to thank him for all the opportunities he has given me, invaluable suggestions and so many midnight calls during experiments. In this I also thank Feng Ye who has taken many trips with me to NIST and trained me in my early days of neutron scattering experience. I would like to acknowledge my committee members for their time and advice, especially some valuable personal advice from Dr. Fernandez Baca and Dr. Mannella.

I am deeply grateful to my colleagues at UTK that have provided the environment for sharing their experiences about the problem issues involved as well as participated in stimulating discussions. I would like to thank Shiliang, Stephen, Jun, Clarina and Leland for their valuable experiences and support. This is also extended to Professor Ted Barnes, whose great knowledge and insight has tremendously helped me in understanding the concept of crystal field. Furthermore I would like to recognize the industrious effort from Dr. Adroja Dr. Bewley and Dr. Guidy at ISIS through our collaboration.

Most of my research work has been conducted at the NIST Center for Neutron Research (NCNR). I am deeply indebted to Dr. Jeff Lynn who has provided so many opportunities. I also would like to express my gratitude to Hye Jung, Ying, William, Sung and Yiming for their help and kindness. My gratitude is also due to our sample providers: professor Tokura's group at Univ. of Tokyo, professor Maple's group at UC San Diego and professor Wang's group at Chinese Academy of Science.

Finally I want to thank my family. The love, encouragement and support from my beloved wife Xuehua has made everything so enjoyable. A very special thought is devoted

to my parents, my brother and sister.

This work was supported in part by the U.S. DOE under contract DE-FG02-05ER46202. ORNL is managed by UT-Battelle, LLC, for the U.S. DOE under contract DE-AC05-00OR22725.

Abstract

We present neutron scattering, with triple-axis and time-of-flight spectrometers, to study the structural and magnetic properties of the layered manganites $Pr_{1-x}Ca_{1+x}MnO_4$ (PCMO), and to determine the crystalline electric field (CEF) levels in iron pnictides $CeFeAsO_{1-x}F_x$ and filled skutterudite compound $PrOs_4As_{12}$.

For the single-layered manganites PCMO, four dopings (x=0.5, 0.45, 0.40 and 0.35) have been studied. At half-doping, the system first becomes charge- and orbital- ordered (CO/OO) near $T_{CO} = 300$ K and then develops CE-type antiferromagnetic (AF) order below $T_N = 130$ K. At temperatures $T_N < T < T_{CO}$, the appearance of short-range AF spin correlations suppresses the CO/OO induced orthorhombic strain. These results suggest that a strong spin-lattice coupling.

In less hole-doped PCMO ($x < 0.5$) compounds, the long-range, three-dimensional antiferromagnetic (AF) correlations at $x = 0.5$ are suppressed. Most remarkably, the magnetic correlations appear in the form of coexisting commensurate (CM) and incommensurate (ICM) fluctuations with strong temperature and doping dependence.

The spin-wave measurement on PCMO ($x = 0.5$) shows good agreement with a magnetic interaction model based on the CE-type arrangement. The magnetic excitations are dominated by ferromagnetic exchange along the zig-zag chain, while the antiferromagnetic coupling between the chains is relatively weak. The INS measurement on the $x = 0.45$ system reveals both symmetric and asymmetric magnetic excitations about the CM peak positions: one dispersive spin wave indicative of the $x = 0.5$ system; and another localized mode at about 1 meV. This strongly suggests two types of spin dynamics originated from separated phases: the CE-type magnetic phase and an additional electronic phase caused by extra electrons introduced into the CE template.

INS has also been used to measure the CEF excitations in the iron pnictides $CeFeAsO_{1-x}F_x$ and filled skutterudite compound $PrOs_4As_{12}$. Two different methods, though, were employed to determine the CEF levels in these two systems.

For nonsuperconducting CeFeAsO, the Ce CEF levels have three magnetic doublets in the paramagnetic state, but these doublets split into six singlets when Fe ions order antiferromagnetically. For superconducting $CeFeAsO_{0.84}F_{0.16}$ ($T_c = 41$ K), where the static AF order is suppressed, the Ce CEF levels have three magnetic doublets at $\hbar\omega = 0, 18.7, 58.4$ meV at all temperatures. Careful measurements of the intrinsic linewidth Γ and the peak position of the 18.7 meV mode reveal clear anomaly at T_c, consistent with a strong enhancement of local magnetic susceptibility below T_c. These results suggest that CEF excitations in the rare-earth oxypnictides can be used as a probe of spin dynamics in the nearby FeAs planes.

For $PrOs_4As_{12}$, a new model was used to fit the energy levels and transition probabilities using first principle calculations. The CEF potential on the Pr3+ ions exerted by two sublattices are treated separately and combined. We identify the Pr^{3+} CEF levels, and show that the ground state is a magnetic triplet, and the excited states are at 0.4, 13 and 23 meV, respectively. A comparison of the observed CEF levels in $PrOs_4As_{12}$ with the heavy fermion superconductor $PrOs_4Sb_{12}$ reveals the microscopic origin of the differences in the ground states of these two filled skutterudites.

The magnetic structure of the $PrOs_4As_{12}$ system and its field-induced phase transitions were also studied. The magnetic unit cell is *A*-type with spins lying along the antiferromagnetic *c*-direction. The critical magnetic field that suppresses the AFM order is anisotropic. We provide evidence that the field causes low-lying CEF level-crossing that is responsible for the field induced phases.

Preface

Portions of this dissertation are derived from published work. The publication information of each work is listed with its corresponding chapter.

Chapter 2:

Songxue Chi, F. Ye, Pengcheng Dai, J. A. Fernandez-Baca, Q. Huang, J. W. Lynn, E. W. Plummer, R. Mathieu, Y. Kaneko and Y. Tokura, "Effect of antiferromagnetic spin correlations on lattice distortion and charge ordering in $Pr_{0.5}Ca_{1.5}MnO_4$". PNAS **104**, 10796 (2007).

Chapter 5:

Songxue Chi, D. T. Adroja, T. Guidi, R. Bewley, Shiliang Li, Jun Zhao, J. W. Lynn, C. M. Brown, Y. Qiu, G. F. Chen, J. L. Lou, N. L. Wang, Pengcheng Dai, "The crystalline electric field as a probe for long range antiferromagnetic order and superconductivity in $CeFeAsO_{1-x}F_x$". Phys. Rev. Lett. (to be published 2008).

Chapter 6:

Songxue Chi, Pengcheng Dai, T. Barnes, H. J. Kang, J. W. Lynn, R. Bewley, F. Ye, M. B. Maple, Z. Henkie, A. Pietraszko, "Inelastic neutron scattering studies of Crystal Field Levels in $PrOs_4As_{12}$", Phys. Rev. B **77**, 094428 (2008).

Contents

List of Tables

List of Figures

Chapter 1

Introduction

1.1 Introduction to neutron scattering

The neutron scattering technique is one of the most invaluable and versatile microscopic probes in condensed matter. This is because of several unique fundamental properties of neutrons. First, the relatively large mass of a neutron ($1.674928 \times 10^{-24} g$) allows thermal neutrons of energy range 5 to 100 meV to have a wavelength of 1 to 3Å, which is comparable to interatomic distance in solids. The energy of thermal neutrons is of the same order as of the fundamental excitations in solids. Also, because a neutron carries no charge. it can penetrate deeply into the bulk and come close to the nuclei. Moreover, it has a magnetic moment. This means that neutrons interact with the unpaired electrons in magnetic ions in magnetic atoms. This property is perfect for the research of magnetic structure. Elastic scattering from this interaction gives information on the arrangement of electron spins and the density distribution of unpaired electrons. Inelastic magnetic scattering gives the energy and wave vector dependencies of magnetic excitations.

When neutrons are scattered, the number of scattered neutrons that enter a given solid angle at a known energy and momentum is measured. The laws of momentum and energy conservation that govern all scattering and diffraction experiments are:

$$\vec{Q} = \vec{k}_f - \vec{k}_i \tag{1.1}$$

$$|\vec{Q}| = \vec{k}_f^2 + \vec{k}_i^2 - 2k_i k_f \cos\theta_s \tag{1.2}$$

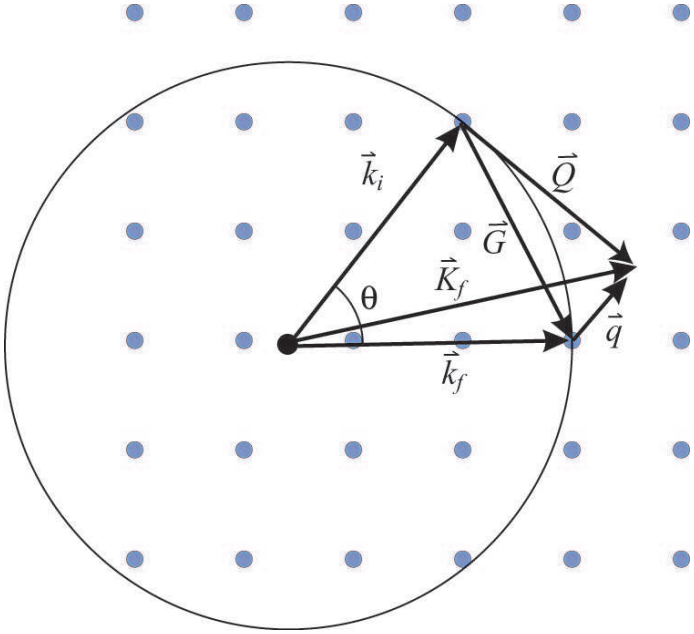

Figure 1.1: Two dimensional representation of reciprocal space showing the Ewald circle and the vector representation for elastic and inelastic scattering.

$$\hbar\omega = E_i - E_f = \frac{\hbar^2}{2m_n}(\vec{k}_f^2 - \vec{k}_i^2) \tag{1.3}$$

In these equations, the wave vector magnitude $k = 2\pi/\lambda$, where λ is the wavelength of the neutron beam, m_n is the mass of neutron, and the momentum transferred to the crystal is $\hbar\vec{Q}$. The subscripts i and f refer to the beam incident on the sample and the diffracted (final) beam.

Fig. 1 shows a Ewald circle in two dimensions. In this diagram, $\vec{k}_i$ is the direction of the incident beam relative to the crystal and $\vec{k}_f$ is the direction of the diffracted beam. If a circle with radius k passes through two points on the circle, one of which is the origin of reciprocal space, the condition for Bragg scattering from the crystal is satisfied. We then have:

$$\vec{Q} = \vec{G} = \vec{k}_f - \vec{k}_i \tag{1.4}$$

,where $\vec{G}$ is a reciprocal-lattice vector. By Bragg's law $\lambda = 2dsin\theta$, we know

$$|\vec{Q}| = |\vec{G}| = 2|\vec{k}_i|sin\theta \tag{1.5}$$

In a diffraction experiment, the magnitude of $\vec{Q}$ is controlled by adjusting the angle 2θ between $\vec{k}_f$ and $\vec{k}_i$. The orientation of $\vec{Q}$ within the reciprocal lattice is set by rotating the sample. Thus, any point in reciprocal space can be measured by an appropriate choice of $\vec{k}_i$, 2θ and the orientation ϕ of the sample relative to $\vec{k}_i$.

For inelastic neutron scattering, $|\vec{k}_i| \neq |\vec{k}_f|$ since a difference is needed for neutrons to gain or loss energy from the sample. For a single crystal sample, energies depend on the relative momentum defined within a Brillouin zone. It is therefore convenient to reference the momentum transfer to the nearest reciprocal lattice vector, ie.,

$$\vec{Q} = \vec{G} + \vec{q} \tag{1.6}$$

During the experiment energy transfer is varied while $\vec{Q}$ is held constant. In neutron scattering, we measure the number of neutron scattered per second into a given solid angle $d\Omega_f$, in the direction of the wave vector $\vec{k}_i$ with a final energy between E_f and $E_f + dE_f$. This is given by the partial differential cross section, $d^2\sigma/d\Omega_f dE_f$. It is expressed as a sum of coherent and incoherent parts. The coherent scattering depends on the correlation between the positions of the same nucleus at different times, and on the correlation between the positions of different nuclei at different times. It therefore gives interference effects and contains information about the cooperative effects among different atoms, such as elastic Bragg scattering or inelastic scattering by phonons or magnons. While the incoherent scattering depends only on the correlation between the positions of the same nucleus at different times and does not give interference effects. It is proportional to the time correlation of an atom with itself and provides information about individual particle motion.

The partial differential cross section due to magnetic interaction V_m for unpolarized neutrons is given by

$$\frac{d^2\sigma}{d\Omega_f dE_f} = \frac{\vec{k}_f}{\vec{k}_i}(\frac{m_n}{2\pi\hbar^2})^2|\langle\vec{k}_f\sigma_f|V_m|\vec{k}_i\sigma_i\rangle|^2\delta(\hbar\omega + E_i - F_f) \tag{1.7}$$

The interaction between the neutron and an unpaired electron is written as

$$V_m(\vec{r}) = -\vec{\mu_n} \cdot \vec{B}(\vec{r}) \tag{1.8}$$

In this equation $\vec{\mu}_n$ is the magnetic dipole moment of the neutron and $\vec{B}(\vec{r})$ is the magnetic field due to the magnetic dipole moment of an unpaired electron. Magnetic field due to the magnetic dipole moment of an electron as

$$\vec{B}(\vec{r}) = \vec{\nabla} \times \vec{A} = \vec{\nabla} \times \frac{\vec{\mu}_e \times \vec{r}}{r^2} \tag{1.9}$$

, where $\vec{\mu}_e$ is the magnetic dipole moment of an electron. By using these expressions, the partial differential cross section of localized spins (1.4) can be expressed as

$$\vec{B}(\vec{r}) = \vec{\nabla} \times \vec{A} = \vec{\nabla} \times \frac{\vec{\mu}_e \times \vec{r}}{r^2} \tag{1.10}$$

, where $\vec{\mu}_e$ is the magnetic dipole moment of an electron. By using these expressions, the partial differential cross section of localized spins can be expressed as

$$\frac{d^2\sigma}{d\Omega_f dE_f} = \frac{\vec{k}_f}{\vec{k}_i} p^2 f^2(\vec{Q}) e^{-2W} \sum_{\alpha,\beta} (\delta_{\alpha\beta} - \vec{Q}_\alpha \vec{Q}_\beta) S^{\alpha\beta}(\vec{Q}, \omega) \tag{1.11}$$

where

$$p = \frac{\gamma e^2}{2 m_e c^2} \tag{1.12}$$

and α, β=x, y, z, and $f^2(\vec{Q})$ is the magnetic form factor, which is the Fourier transform of the spin density.

The scattering function $S^{\alpha\beta}(\vec{Q}, \omega)$ is define as

$$S^{\alpha\beta}(\vec{Q}, \omega) = \frac{1}{2\pi} \sum_{\vec{r}} \int_0^\infty dt e^{i\vec{Q}\cdot\vec{r} - \omega t} \langle S_0^\alpha(0) S_{\vec{r}}^\beta(t) \rangle \tag{1.13}$$

where $\langle S_0^\alpha(0) S_{\vec{r}}^\beta(t) \rangle$ is the time-dependent spin-spin correlation function describing how α component at position 0 correlates with β component of another spin at position $\vec{r}$ after time t.

Since the scattering function is the Fourier transform in space and time of spin-spin correlation function, the evolution of the system of spins in space and time can be directly measured in a neutron scattering. In a magnetically ordered system, the differential cross

section for coherent elastic scattering can be written as

$$\frac{d\sigma}{d\Omega} = N_M \frac{(2\pi)^3}{V_M} \sum_{\vec{G}_M} \delta(\vec{Q} - \vec{G}_M) |\vec{F}_M(\vec{G}_M)|^2 \tag{1.14}$$

, where N_M, V_M and $\vec{G}_M$ are the volume of the magnetic unit cell, the number of such cells in the sample, and the reciprocal lattice vector of the magnetic unit cell. The term $\vec{F}_M(\vec{G}_M)$ is the magnetic structure factor and it is defined as

$$\vec{F}_M(\vec{G}_M) = p \sum_j f_j \vec{G}_M \times (\langle \vec{M}_j \rangle \times \vec{G}_M) e^{i\vec{G}_M \cdot \vec{r}} e^{-W_j} \tag{1.15}$$

, where f_j and $\langle \vec{M}_j \rangle$ are the magnetic form factor and the thermal-averaged magnetic moment of $j-$th ion, respectively. The sum in the above equation is over all sites within the magnetic unit cell. The integrated intensity of a magnetic Bragg peak for unpolarized neutron is given by

$$I = C \frac{|\vec{F}_M(\vec{G}_M)|^2}{sin2\theta} \tag{1.16}$$

, where C is a constant depending on the incident neutron flux, sample volume, and counting time and θ is the scattering angle. Therefore, the magnetic spin structure can be determined from the elastic magnetic peak intensity measurement.

There exist two main types of neutron sources: reactor and spallation neutron sources. For this doctoral research, the manganites have been studied with reactor-based triple axis spectrometers, while the CEF excitations have been mainly studied with spallation-based time-of-flight spectrometers.

As shown in fig. 1.2(a), the three axes correspond to the axes of rotation of the monochromator, the sample and the analyzer. The monochromator defines the direction and magnitude of the momentum of the incident beam and the analyzer performs a similar function for the scattered or final beam. In an elastic scattering event, neutron is deflected but loses or gains no energy. In an inelastic event, neutron loses or gain energy during the interaction. In both cases, neutron is scattered through the 2θ angle.

For time of flight spectrometer, a single incoming energy is selected, and the final energy and momentum transfer is analyzed by time of flight and detector angle ϕ. The neutrons

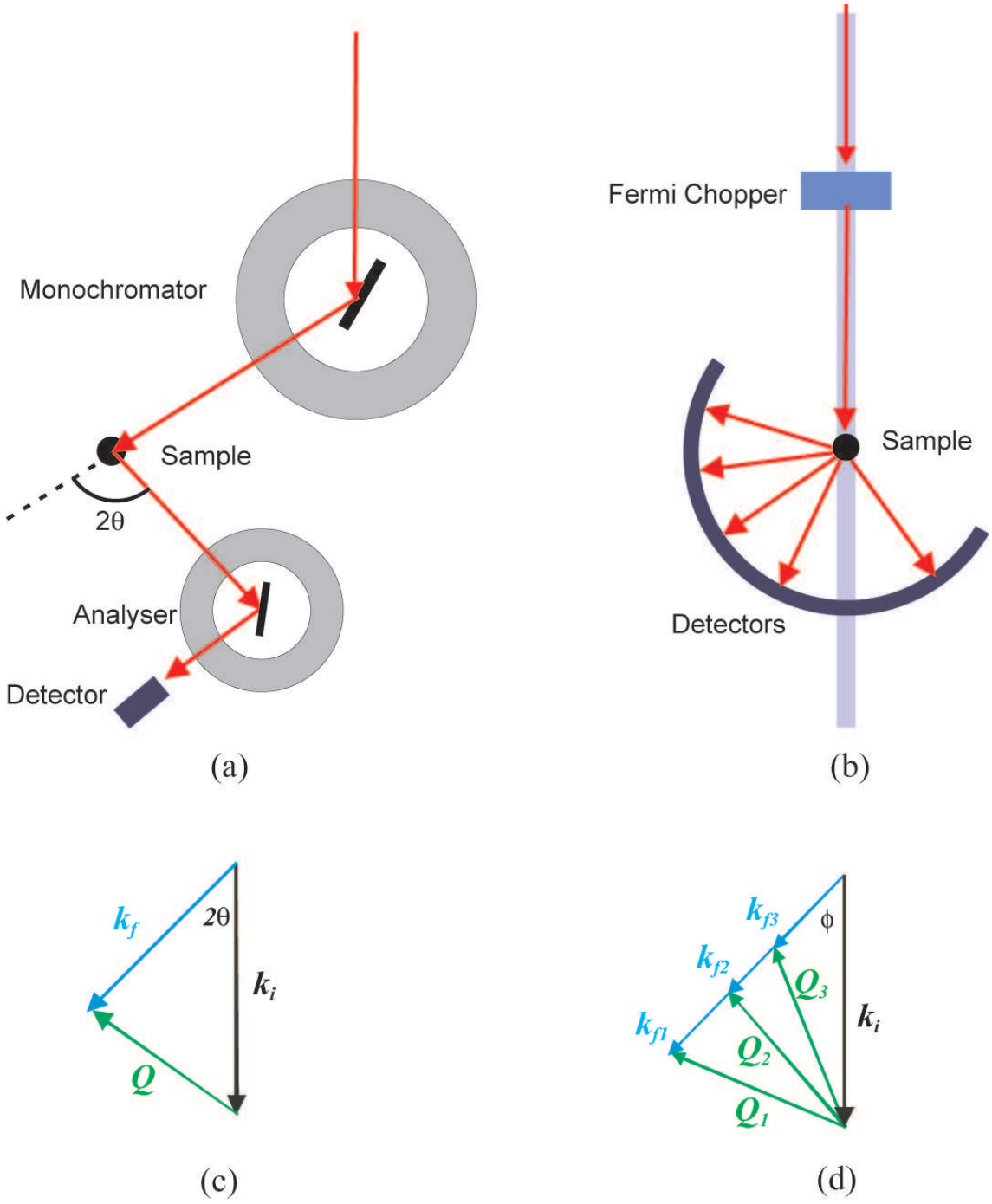

Figure 1.2: (a) The schematic of the fundamental components of a triple axis spectrometer. (b) Schematic for the time ordered processed in a time-of-flight spectrometer. (c) The scattering triangle shows that neutron is scattered through angle 2θ. The elastic neutron scattering event occurs when neutrons do not gain or lose momentum. Otherwise, it is elastic neutron scattering. (d) With time-of-flight spectrometer, energy spectrum over a wide range of wave vector can be measured simultaneously.

arrive at the sample in monochromatic pulses of known energy. After scattering from the sample they are detected in fixed arrays of detectors as a function of their total time of flight. With the knowledge of the sample detector distances and the incident beam energy, the final energy can be calculated. For all energies the final wave vector will lie along the same direction, however the magnitude will decrease with the velocity of the incident energy neutrons. The scattering triangle is thus altered in time.

The main disadvantage of triple axis spectrometer is that it can only examine one position at a time in the (Q, E) space. Time-of-flight spectrometers are capable of collecting energy spectra for a wide range of wave vectors simultaneously, as shown in fig. 1.2(d).

1.2 Description and determination of the CEF

In a solid, a rare-earth (RE) ion experiences an electrostatic crystalline electric field (CEF) potential $V_{CEF}(\mathbf{r})$. This potential is set up by the neighboring ions that gives charge distribution $\rho(\mathbf{r'})$, which can be expressed as the multipolar expansion centered on that RE ion.

$$V_{CEF}(\mathbf{r}) = \sum_k V^{(k)}(\mathbf{r}) \tag{1.17}$$

The potential reflects the point symmetry of the RE ion site. If there is no overlap between the charge distribution and the $4f$ wave functions, the potential fulfils Laplace's equation $\Delta V_{CEF}(\mathbf{r}) = 0$. Then it can be expanded in terms of spherical harmonics as

$$V_{CEF}(\theta, \phi) = Y^l(\theta, \phi) \tag{1.18}$$

where the individual contributions $Y^l(\theta, \phi)$ can be expressed as the sums (over q) of numerical factors times the functions $\langle r^l \rangle Y_{l,q}(\theta, \phi)$, where $\langle r^l \rangle$ is the expectation of the r^k for an open-shell electron, and can be expressed as a radial integral.

In 1952, Stevens *et al.* [115] developed the so called "'operator equivalent" techniques, which enable one to calculate quantitatively the effect of CEF on the total angular momentum J of the magnetic ion in a simple manner. In this method one replaces successive terms in eq.(5.2) by suitable angular momentum operator. The number of terms needed

is decided by the local point group symmetry and the finite value of the orbital angular momentum of individual magnetic electrons. For the $f-$electron wave function terms up to the sixth degree are sufficient. They act on the $4f-$ shell as a whole instead of on the individual $4f-$electrons as do the polynomials in the x_l, y_l, z_l in eq.(1).

The following rules hold when transforming an expression $f(x_l, y_l, z_l)$ into its J-operator-equivalent. (1) Replace any polynomial in x, y, z by the corresponding product of J_x, J_y, J_z written in a symmetrized form, for instance, $xy \rightarrow \frac{1}{2}(J_x J_y + J_y J_x)$. (2) The constants of proportionality depend on the degree l of the polynomial and on L, S and J, which include the average $\left\langle r^k \right\rangle$ over the $4f$ wave functions. The resulting form for H_{CEF} is then expressed as

$$H_{CEF} = \sum_{l,m} B_l^m O_l^m, \tag{1.19}$$

or,

$$H_{CEF} = \sum_{l,m} A_l^m \left\langle r^l \right\rangle \theta_l O_l^m \tag{1.20}$$

where the θ_l are $\alpha_l, \beta_l, \gamma_l$ for l=2,4 and 6. The B_l^m (or A_l^m) are CEF parameters which are either measured experimentally or calculated by means of a simple model.

The differential cross-section for magnetic scattering is related to the imaginary part of the magnetic susceptibility $\chi(\mathbf{Q}, \omega)$ through

$$\frac{d^2\sigma}{d\Omega_f d\omega} \sim \frac{1}{1 - exp(-\beta\omega)}) Im\chi(\mathbf{Q}\omega), \tag{1.21}$$

where $\beta = (k_B T)^{-1}$. For a system of N non-interacting dilute RE ions, $Im\chi(\omega)$ consists of a sequence of δ-functions provided that lifetime effects are neglected. Specifically for small Q and for unpolarized neutrons, the intensies are given by the matrix elements $|\langle n\,|J_z|\,m\rangle|^2$ following the diagonalization of the CEF Hamiltonian [116, 117]. This results in

$$S(\mathbf{Q},\omega,T)=\frac{1}{2}(g_N r_e)^2\frac{\omega}{1-e^{-\beta\omega}}[g_J f(\mathbf{Q})]^2\times\sum_{nm}\rho_m\left|\langle n\left|J_z\right|m\rangle\right|^2\frac{1-exp(-\beta\Delta_{nm})}{\Delta_{nm}}P(\mathbf{Q},\omega-\Delta_{nm},T) \tag{1.22}$$

where $\mathbf{Q}$ and ω are the momentum and energy transfer, $f(\mathbf{Q})$ is the magnetic form factor, and Δ_{nm} is the transition energy from the nth level to the mth level. $\rho_m = Z^{-1}exp(-\beta\Delta_{1m})$, where Z sums over all the states and indicates the occupation of the mth level at temperature T. The CEF case in the limit of δ-functions is given by

$$S(\mathbf{Q},\omega,T)=\frac{1}{2}(g_N r_e)^2[g_J f(\mathbf{Q})]^2\times\sum_{nm}\rho_m\left|\langle n\left|J_z\right|m\rangle\right|^2\delta(\mathbf{Q},\omega-\Delta_{nm},T) \tag{1.23}$$

Here $\left|\langle n\left|J_z\right|m\rangle\right|^2=\frac{1}{2}\left|\langle n\left|J_\perp\right|m\rangle\right|^2$, where $J_\perp$ is the perpendicular moment operator used in many literatures.

As shown in eq. (1.23), the intensity of the CEF excitations decreases with $\mathbf{Q}$ for the magnetic form factor term $|f(\mathbf{Q})|^2$. This can be useful in distinguishing the CEF peaks from phonon peaks, whose intensity is usually proportional to $\mathbf{Q}^2$.

1.3 Introduction to CMR effect in manganites

Soon after discovery of high-T_c superconductivity in copper oxides in the late 80s, there were reports that some manganites, such as $Nd_{0.5}Pb_{0.5}MnO_3$ [1] and $La_{2/3}Ba_{1/3}MnO_x$ [2], showed a huge change in electrical resistivity when a magnetic field was applied. This effect is generally known as magnetoresistance, a phenomenon that has been known since the 50s. But the resistivity change observed in these oxides was so much larger than any other forms of magnetoresistance previously discovered. The MR ratio, defined as $\Delta R/R = (R_H - R_0)/R_H$ (R_0 is the resistance without a magnetic field, and R_H is that with $H = 6T$, reached as high as $1\times10^5\%$ in $La_{0.67}Ca_{0.33}MnO_x$ [3]. The effect observed in the manganese perovskites, was therefore called "colossal" magnetoresistance to distinguish it from the giant magnetoresistance (GMR) observed in magnetic multilayers. The MR ratio record was later reset to $1\times10^6\%$ with thin film of $Nd_{0.7}Sr_{0.3}MnO_\delta$ near 60 K under a field of 8 T [4]. It was not until then did the real excitement over the manganese

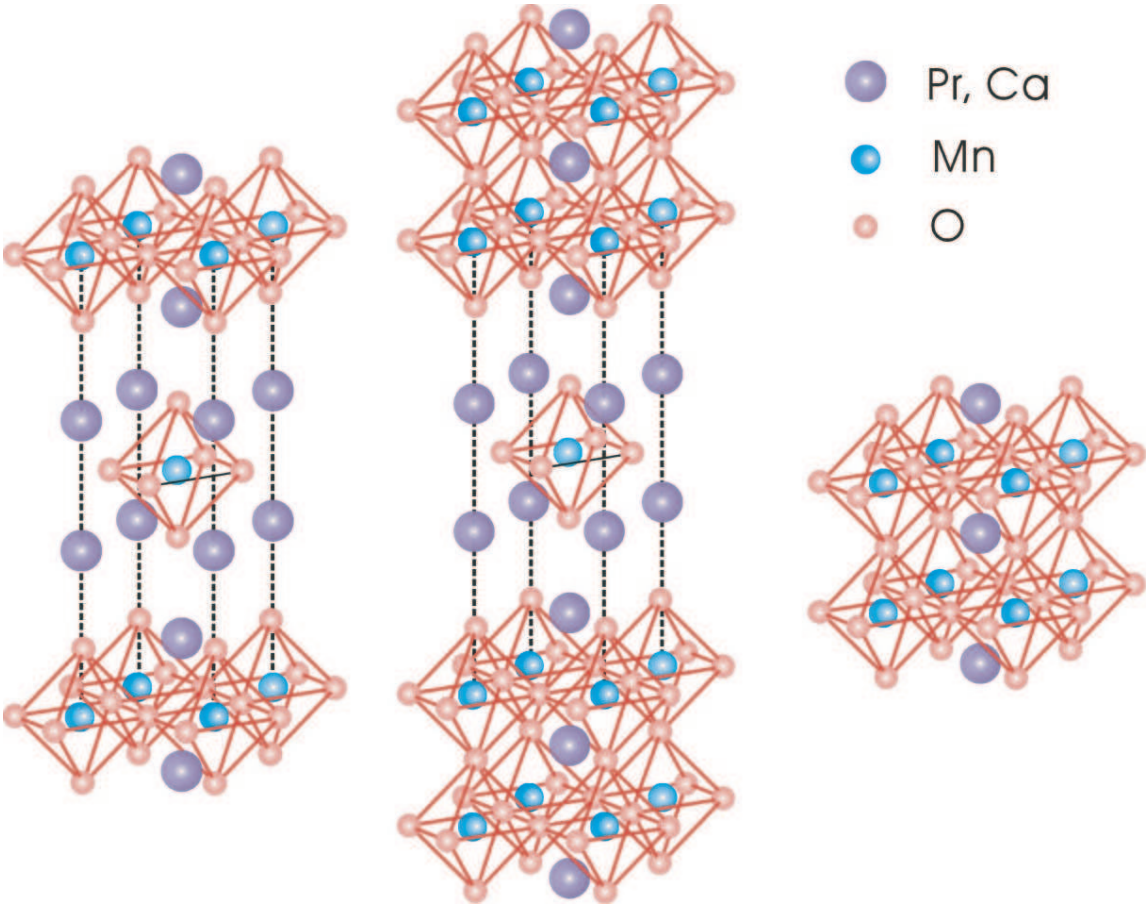

Figure 1.3: Schematic crystal structures of 3 typical Ruddlesden-Poper series.

perovskite start. The perovskite manganite is a member of Ruddlesden-Popper (RP) series of manganese oxides, $(R,A)_{n+1}MnO_{3n+1}$, where R and A represent trivalent rare earth and divalent alkaline earth ions respectively. The crystal structures of three typical members of this series are shown in figure 1.2. The perovskite ($n = \infty$) and the double layered ($n = 2$) manganites have attracted considerable attention over the last decade because of the CMR effect they exhibit.

These compounds exhibit a great variety of ground states and complex phase diagram as a function of pressure [5], temperature [1,2], magnetic field [1,6], and chemical pressure [7]. Among the theoretical works that tried to explain the origin of the ferromagnetic phase in the 1950s, Zener's model [9], later termed as "Double Exchange" (DE) model, properly explained ferromagnetism of manganites. The DE model was later continued and modified by Anderson and Hasegawa [10]. The DE theory predicts that electron

movement from one species to another will be facilitated more easily if the electrons do not have to change spin direction in order to conform with Hund's rules when on the accepting species. The ability to hop reduces the kinetic energy. Hence the overall energy saving can lead to ferromagnetic alignment of neighboring ions. This model is similar to superexchange. But in superexchange, a ferromagnetic alignment occurs between two atoms with the same valence; while in DE model the interaction occurs only when one atom has an extra electron compared to the other. The DE generates a ferromagnetic metallic state at low temperatures and a metal to insulator transition (MIT). A ferromagnetic (FM) to paramagnetic (PM)/antiferromagnetic (AFM) transition coincides the MIT, and is also coupled with a structural transition, which implies the disappearance of the static Jahn-Teller distortion in the FM state.

In 1995, Millis *et. al* [8] demonstrated using $La_{1-x}Sr_xMnO_3$ system that DE model alone is not sufficient to explain the CMR effect, and that in addition to DE physics a strong electron-phonon interaction arising from the Jahn-Teller (JT) splitting of the outer Mn d level plays a crucial role. This JT interaction lifts the double degeneracy of the energy orbitals, while preserving the total orbital energy. Meanwhile the mismatch of radii of cations causes the buckling of the oxygen octahedral network, which leads to altering the Mn-O-Mn bond angle and bond distance [11,12], thus affects the hopping probabilities of electrons and the DE interaction.

1.4 Introduction to the Pr-base filled skutterudites

Skutterud is a place in Norway where $CoAs_3$ based mineral was first mined as a source of cobalt and nickel. Compounds with the same cubic structure have been called skutterudites. The structure of skutterudite has two voids in each unit cell that are large enough to accommodate various atoms including lanthanides and Yb. This is how the name "filled skuterudite" (FS) came about. These compounds have the formula MT_4X_{12} where M=alkali metal, alkaline earth, lanthanide, or actinide: T=Fe, Fr, or Os; and X=P, As, or Sb. Figure 1.3 shows the structure of a FS compound, where the M ions are located at the center of a cage formed by 12 pnicogen atoms. The FS compounds have been the objects of a great deal of research due to the rich strongly correlated electron phenomena

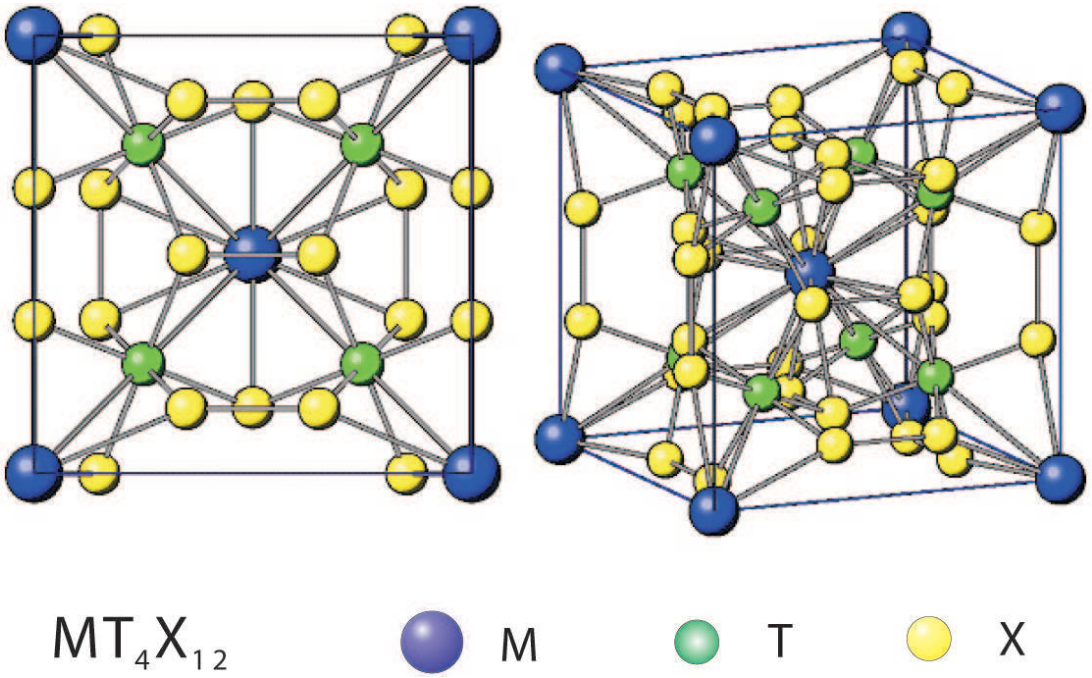

Figure 1.4: Schematic crystal structures of filled skutterudite MT_4X_{12}, where M=rare earth, T=Fe,Ru,Os, X=P, As, Sb.

they display. They show a great variety of thermal, magnetic and transport properties due to the interaction of conduction electron and f-electron orbital of magnetic ions and a "rattling" motion of R ion resulting from the unique crystal structure. The discovery of the heavy fermion phenomena in $PrOs_4Sb_{12}$ [13], $PrFe_4P_{12}$ [14], $PrRu_4Sb_{12}$ [15] and $PrRu_4Sb_{12}$ [16] changed the common belief that metallic Pr-based compounds are stable magnetic materials. Quadrupolar Kondo effect, which results from the interaction of conduction electrons with quadrupole moments of Pr^{3+} ions, is suggested to be responsible for their heavy-fermion behavior. Superconductivity has been observed in all the above-mentioned materials, of which $PrOs_4Sb_{12}$ is the first of this kind and exhibits many exotic features both above and below the superconducting transition temperature at T_c=1.85 K [13]. A significant mass enhancement of the conduction electrons induced by f-electron was observed in specific heat, upper critical field [13, 17], and de Haas-van Alphen measurements [19].

The strongly correlated electron phenomena and ground states found in the Pr-based FS compounds are summarized [18] in fig.3., which includes the type of property and

Pr		T		
		Fe	Ru	Os
X	P	AFQ order T_{AFQ}=6.5K HF-Metal	Insulator M-I transition T_{MI}=62 K	No order for T>70 mK
	As	FM T_{FM}=18 K	BCS SC T_c=2.4 K	AFM TN=2.3 K HF-Metal
	Sb	Magnetic? T_M~4.1 K	BCS SC Tc=1.1 K	Unconv. SC T_c=1.85 K HF-Metal

Figure 1.5: Properties of the Pr-based filled skutterudites PrT_4X_{12}. where T=Fe,Ru,Os, X=P, As, Sb.

temperature at which it occurs. The ground states show remarkable sensitivity of the Pr-base FS compounds to the substitution of the transition metal and pnictogen atoms. These materials enable us to study a broad range of exotic behaviors with very few adjustable variables.

Knowledge of the CEF ground state is essential to understanding the role of the $4f$-electrons in the superconductivity. In $PrOs_4Sb_{12}$, $4f$ electrons are well localized under the cubic CEF with T_h symmetry. In cubic symmetry the Pr^{3+} ion splits into a singlet Γ_1, a nonmagnetic doublet Γ_3, and two magnetic triplets (Γ_4 and Γ_5). The quadrupolar fluctuation is permitted by a nonmagnetic doublet. In recent literatures there is evidence both for singlet model [21–23] and for the Γ_3 doublet model [13]. As a reliable method of determining the crystal field potential, neutron scattering has been used to settle the controversy. Evidence from both elastic and inelastic has mounted to favor a Γ_1 singlet ground state although CEF level schemes are not totally agreed upon. This rules out any quadrupolar fluctuations within the ground state level, as required by the quadrupolar Kondo effect.

K. Kuwahara *et.al* [20] investigated the low energy magnetic excitations on single crystals of $PrOs_4Sb_{12}$ using high resolution inelastic neutron scattering experiments. They

observed new quadrupolar excitons, which are CF excitations modulated by quadrupolar interactions. It is the first example of the excitons due to quadrupolar interactions. A softening of this excitation at $Q = (1, 0, 0)$ was observed and a sudden narrowing of line-widths below T_c suggests that the quadrupolar excitons are related to the HF superconductivity.

Unlike the phosphate and antimonide Pr-based filled skutterudites, the arsenides have not been investigated in great detail. In view of the interesting correlated electron phenomena found in this class of materials, we have systematically studied the CEF levels and the magnetic properties of the arsenide Pr-based FS compound $PrOs_4As_{12}$.

1.5 High-T_c superconductivity in the iron pnictides

In the beginning of this year (2008), Hosono's group in Japan discovered a new superconductor $LaFeAsO_{1-x}F_x$ ($x = 0.05 \sim 0.12$) with transition temperature (T_c) of 26 K [25]. The iron oxypnictide contains layers of FeAs that are separated by layers of LaO. The Fe atoms order antiferromagnetically in the non-superconducting parent compound LaFeAsO [26], which becomes superconducting when doped with fluorine in the LaO layers. This has triggered a new round of superconductor race in the community of condensed matter physics. The T_c has been remarkably raised when La is replaced with Ce [28], Nd [29] and Sm [27]. Both hole- and electron-doped superconductors have been reported. The consensus so far seems to be that these compounds do not conform to conventional BCS-Eliashberg theory and that spin density wave type of antiferromagnetic order competes with superconductivity. The undoped material LaOFeAs has been reported to undergo a spin density wave (SDW) transition based on transport measurements. The elastic neutron scattering measurements [26] has confirmed that the parent compound is a long-range ordered antiferromagnet with a simple stripe-type AFM structure within the plane that is doubled along the c-axis. A structural phase transition has also been observed before the AFM phase transition that changes the structure from space group $p4/nmm$ to $P112/n$ at low temperatures. The materials are an antiferromagnet at low doping and increased doping destroys the antiferromagnetism, leading to superconductivity [30]. Photoemmission measurement [31] revealed another feature very similar to the cuprate superconductors: possible pseudogap existing above T_c. Given the tremendous

similarities the FeAs compounds bear with the cuprates, many researchers speculated that the mechanism of superconductivity in these two families are related.

However, further investigations revealed major differences between the FeAs materials and cuprates. Although both exhibit AFM order, the parent compound in the cuprates is a Mott insulator where the charge carriers are localized while the parent compounds of iron pnictides are AFM spin-density-wave metal, where the electrons are itinerant. Another main difference is that the cuprates are two dimensional with electrons reside in Cu-O sheets, resulting in the effective slightly smaller Coulomb repulsion than that expected for localized Cu d electrons. In contrast, all five Fe $3d$ orbitals contribute to the electronic structure in the vicinity of the Fermi level in the FeAs materials. This orbital mixing, coupled to the appreciable hybridization of the Fe d electrons with the As p-electrons, may strongly reduce the effective Coulomb repulsion as compared to the cuprates. Moreover, only moderate anisotropic upper critical fields have been reported for the FeAs compounds [32], as opposed to the highly anisotropic upper critical fields for the copper oxides.

Another conspicuous fact is that the transition temperature Tc is tremendously affected when La (26K) is replaced by magnetic rare-earth (R) ions, such as Ce (41 K), Pr(52 K), Nd(50 K), Sm(43 K) and Gd(10 K). This is in contrast to both the conventional superconductors and the perovskite-type copper-oxide compounds. These rare-earth (R) ions usually have a large detrimental effect on conventional superconductors; whilst T_c of copper-oxides is essentially unchanged upon replacing the Y and La ions by most magnetic R ions (except for Ce and Pr). So for a detailed investigation of the superconductivity and the competition between SC and AFM order in these newly found lanthanides iron oxypnictide compounds, the knowledge of the electronic ground state of the rare-earth ions, especially the CEF is indispensable. For instance, the temperature dependence of the line widths of the CEF excitations provides information on the SC energy gap. Also quantitative understanding of the CEF levels and will help monitor the local symmetry, especially charge distribution on the Fe-As plane which is an analogy to the Cu-O plane in copper oxide superconductors.

In addition to the LaFeASO series and its F-doped and La-substituted compounds, currently dubbed the "1111" systems, new classes of Fe-based materials, such as the "122" structure and the FeSe structure, have been synthesized and found superconducting. For

example, $(Ba_{1-x}K_x)Fe_2As_2$ has T_c ∼38 K for x=0.4 [33] and FeSe has $T_c = 27\ K$ [34]. Many experimental approaches under various conditions have been used to explore different facets of this newly found iron jewelry. The daily updates are so dazzling that one can easily get lost in the blink of an eye. Hopefully these new Fe-based superconductors will reveal something that has not been accessible for the cuperates so that the complement they have for each other will finally resolve the high-T_c superconductivity problem.

Chapter 2

Effect of antiferromagnetic spin correlations on lattice distortion and charge ordering in $Pr_{0.5}Ca_{1.5}MnO_4$

We use neutron scattering to study the lattice and magnetic structure of the layered half-doped manganite $Pr_{0.5}Ca_{1.5}MnO_4$. On cooling from high temperature, the system first becomes charge- and orbital- ordered (CO/OO) near $T_{CO} = 300$ K and then develops checkerboard-like antiferromagnetic (AF) order below $T_N = 130$ K. At temperatures above T_N but below T_{CO} ($T_N < T < T_{CO}$), the appearance of short-range AF spin correlations suppresses the CO/OO induced orthorhombic strain, contrasting with other half-doped manganites, where AF order has no observable effect on the lattice distortion. These results suggest that a strong spin-lattice coupling and the competition between AF exchange and CO/OO ordering ultimately determines the low-temperature properties of the system.

2.1 Single-layered manganites

$Pr_{1-x}Ca_{1+x}MnO_4$ is the $n = 1$ end member of Ruddlesden-Popper (RP) series of manganese oxides, as introduced in section 1.2. The CMR effect, partially explained by the

Zener DE mechanism, seems to arise from the competition between a ferromagnetic metallic phase and a paramagnetic phase with a cooperative (short-range) ordering of charges, orbital and spins. The paramagnetic phase is accompanied by short-range structural distortion as a result of charge and orbital ordering (CO-OO), which takes place in the MnO_2 planes. In single-layered systems the MnO_2 planes are separated by R(A)O layers. The reduced dimensionality results in confinement of the itinerant e_g carriers and anisotropic transport properties [35], therefore can provide a valuable insight in understanding the role the CO-OO plays in higher dimensional systems. It can also contribute to a deeper understanding of single-layer transition metal oxides in general.

The rich phase diagram and variety of ground states of perovskite manganites are related to tolerance factor, which is a measure of the O-octahedra distortions [70]. This distortion is caused by different size A site ions in single layered manganites. Moritomo *et. al* [35] reported that the CO transition in half doped $R_{0.5}Sr_{1.5}MnO_4$ is significantly suppressed by the decreasing average radius of R^{3+} and eventually vanishes.

The most intensively studied single-layer manganite is half doped $La_{1-x}Sr_{1+x}MnO_4$. A cooperative ordered phase of CO-OO and AF spin ordering is observed at low temperature [38,102] and the resultant superstructure is believed to be CE type [39–41] although there is evidence against it [45]. A full ordering of charges and orbitals is ruled out by quantitative structural analysis [39, 40].

Compared with $La_{0.5}Sr_{1.5}MnO_4$, the average radius of A site ions in $Pr_{0.5}Ca_{1.5}MnO_4$ is smaller. Less distortion leads to smaller bandwidth. By making a comparison study of PCMO with the results of LSMO, one hopes to understand the effect of tolerance factor on CO-OO, magnetic ordering and eventually CE-type cooperative ordering.

2.2 Motivations

Understanding the competition and coupling between charge, lattice, and spin degrees of freedom in doped transition metal oxides continues to be one of the most profound intellectual challenges in modern condensed matter physics since the discovery of high-transition temperature (high-T_c) superconductors and the colossal magnetoresistance (CMR) manganese oxides [42]. The complexity of transition metal oxides is directly responsible for their

tunability and the balance between different competing phases can produce large changes in the physical properties. For example, superconductivity in the high-T_c superconductors $La_{2-x}Ba_xCuO_4$ becomes drastically suppressed at the doping level of $x = 1/8$ due to the spin and charge phase separation (the so-called "striped" phase), where charge ordering (CO) establishes a template at a higher temperature to be followed by antiferromagnetic (AF) stripe order at a lower temperature [43, 44]. The low-temperature AF phase has little or no influence on the already established CO phase because of its low energy scales. Similarly, the long-range AF order in the parent compounds of high-T_c copper oxides is characterized by spin-only antiferromagnetism and has little or no effect on the underlying lattice [42]. These results suggest that spin-lattice coupling is weak in high-T_c copper oxides.

In the case of CMR manganites $A_{1-x}A'_xMnO_3$ (where A and A' are trivalent rare- and divalent alkaline-earth ions respectively), the competition between charge, lattice, and spin degrees of freedom can be delicately balanced to form a variety of ground states [42]. Before doping any holes into the system, the parent compound such as $LaMnO_3$ has an insulating ground state, where the Mn^{3+} spins order in the A-type AF structure [45, 46]. For hole-doping level around $x = 0.3$ by substituting trivalent La^{3+} with divalent Ca^{2+}, $La_{1-x}Ca_xMnO_3$ becomes a metallic ferromagnet with a CMR effect near the Curie temperature T_C. The formation of long-range ferromagnetic order at T_C also induces a large lattice distortion, suggesting a strong spin-lattice coupling [47]. Upon increasing the doping level to $x = 0.5$, $La_{0.5}Ca_{0.5}MnO_3$ changes again into an AF insulating phase but with a CE-type AF structure [45]. Here, equal amounts of Mn^{3+} and Mn^{4+} distribute alternately in the MnO_2 plane of $La_{0.5}Ca_{0.5}MnO_3$, forming a checkerboard CE-type pattern as schematically depicted in Figure 1(a) [45, 46]. Although the CE-type AF order disappears on warming above the Néel temperature T_N, the system is still charge and orbitally ordered (CO/OO). Such CO/OO order is strongly coupled to the lattice and induces an orthorhombic distortion that only disappears at temperatures well above CO/OO ordering temperature T_{CO}.

For example, in the three-dimensional nearly half-doped perovskites $La_{0.5}Ca_{0.5}MnO_3$ [48], $Pr_{0.5}Ca_{0.5}MnO_3$ [49, 50], and $Pr_{0.55}(Ca_{0.8}Sr_{0.2})_{0.45}MnO_3$ [51], the CO/OO ordered lattice first established slightly below room temperature is followed by a CE-type AF order

around 130 K [Fig. 1(a)]. X-ray and neutron diffraction experiments have shown that the materials exhibit a tetragonal to orthorhombic phase transition near T_{CO}. Furthermore, the orthorhombicity increases with decreasing temperature and shows no anomalies across the CE-type AF phase transition [48–51]. These results thus suggest that CO/OO order is strongly coupled to the lattice and there is a weak spin-lattice coupling. As a consequence, CO/OO ordering in half-doped perovskites may have a larger energy scale than the low temperature magnetic order. For the single layer half-doped manganites such as $La_{0.5}Sr_{1.5}MnO_4$ (LSMO), a similar behavior is also observed. Here, the material exhibits a tetragonal to orthorhombic phase transition at the CO/OO temperature of 230 K and then orders antiferromagnetically with a CE-structure below about 120 K [37, 52]. The lattice distortion and orthorhombicity of LSMO show no anomalies below the AF phase transition. Therefore, it appears that CO/OO order in doped transition metal oxides generally is strongly coupled to the lattice, while the low-temperature magnetic order has no influence on CO/OO ordering.

Although CO/OO order in doped manganites may have a stronger coupling to the lattice than that of the AF order, its microscopic origin is still unclear. Theoretically, CO/OO order established at higher temperatures may actually have a purely magnetic spin origin [53]; arise from a competition between the kinetic energy of the electrons and the magnetic exchange energy [54], due to a tendency of the Jahn-Teller distorted Mn^{3+} ions to maximize their relative distances to gain electron kinetic energy [55], or come from a purely Coulomb interaction without invoking magnetic interactions [56, 57]. In general, charge ordering in half-doped manganites is intimately related to the orbital ordering, where the orbitals of e_g electrons on Mn^{3+} sites form zigzag ferromagnetic chains that order antiferromagnetically [Fig. 2.1(a)] [58, 59]. One way to sort out the relationship between CO/OO and CE-type AF order is to carry out systematic measurements on $A_{0.5}A'_{0.5}MnO_3$ or layered $A_{0.5}A'_{1.5}MnO_4$ with different A and A' ionic sizes. Decreasing the ionic size at A and A' sites in half-doped manganites increases the buckling of the MnO_6 octahedra and therefore the lattice distortion of the perovskite. For three-dimensional $A_{0.5}A'_{0.5}MnO_3$, replacing Sr in $Pr_{0.5}Sr_{0.5}MnO_3$ ($T_{CO} = 150$ K) by the smaller Ca to form $Pr_{0.5}Ca_{0.5}MnO_3$ ($T_{CO} = 260$ K) moderately enhances the CO/OO ordering temperature, but dramatically increases the magnitude of the magnetic field (from 5 T for $Pr_{0.5}Sr_{0.5}MnO_3$ to 27 T for

$Pr_{0.5}Ca_{0.5}MnO_3$) needed to suppress CO/OO [60]. These results suggest that CO/OO ordering is more stable for manganites with smaller ionic size and larger lattice distortion; and has an energy scale larger than that of the magnetic exchange. Since single crystals of three-dimensional $A_{0.5}A'_{0.5}MnO_3$ with the CE-type AF structure are unavailable, we study $A_{0.5}A'_{1.5}MnO_4$ with different A and A' ionic sizes.

2.3 Materials and Methods

We grew single crystals of PCMO using the traveling solvent floating zone technique. High resolution neutron powder diffraction (HRNPD) experiments were carried out on BT-1 at the NIST Center for Neutron Research (NCNR) with powder of crushed single crystals. Elastic neutron scattering measurements were carried out on the thermal triple-axis instruments BT-7 and BT-9 at NCNR. Rietveld analysis on the powder data indicates that the crystals were single phase without detectable impurities. The crystals were mounted in a closed cycle He displex and aligned in successive orientations to allow the wavevectors in the form of (h, h, l), $(h, k, 0)$ and $(h, 0, l)$ accessible in the horizontal scattering plane. Neutron energies of 14.7 meV and 13.7 meV were used with pyrolytic graphite crystals as monochromator, analyzer and filters.

At room temperature, PCMO has the orthorhombic structure with lattice parameters $a_o = 5.380$ Å $b_o = 5.404$ Å and $c_o = 11.831$ Å (space group $bmab$). For simplicity, we use the tetragonal unit cell for the triple-axis measurements and label the momentum transfers $\mathbf{q} = (q_x, q_y, q_z)$ as $(h, k, l) = (q_x a/2\pi, q_y a/2\pi, q_z c/2\pi)$ in reciprocal lattice units (rlu), where $a = (a_o + b_o)/2\sqrt{2} = 3.814$ Å.

2.4 Results

Here we present neutron scattering results on $Pr_{0.5}Ca_{1.5}MnO_4$ (PCMO), a single layer manganite with smaller average A and A' site ionic radius and larger lattice distortion than that of LSMO [61]. We chose to study PCMO in order to determine the effect of the lattice distortion on the CO/OO and AF phase transitions. Since CO/OO is not affected by CE-type AF order in LSMO [37, 52], one would expect that CO/OO becomes

more robust when the larger (La,Sr) ions in LSMO are replaced by smaller (Pr,Ca) in PCMO. Surprisingly, we find that the development of short-range AF spin correlations in the MnO_2 plane of PCMO significantly affects the CO/OO-induced lattice distortion and reduces the orthorhombicity of the system below T_N. Our results thus indicate the presence of a strong spin-lattice interaction, suggesting that antiferromagnetism can reduce the CO/OO-induced orthorhombic strain and thus compete with the CO/OO ordering.

2.4.1 Structural and magnetic diffractions

Because one expects PCMO to behave similarly to LSMO, we first probe the low temperature magnetic and superlattice peaks associated with the CE-type AF structure and CO/OO state. Figs. 2.1(d) and (f) show the temperature dependence of the $\mathbf{q} = (3/2, 3/2, 0)$ and $\mathbf{q} = (3/4, 5/4, 0)$ structural superlattice peaks, respectively. Below $\sim$310 K, a structural phase transition associated with the CO/OO ordering occurs, consistent with the large increase in resistivity from transport measurements [62]. Figs 2.1(c) and (e) show the temperature dependence of the AF Bragg peaks at $\mathbf{q} = (1/4, 1/4, 3/2)$ and $\mathbf{q} = (1/2, 0, 1/2)$, corresponding to the Mn^{3+} and Mn^{4+} of the CE-type AF structure in Fig. 2.1(a), respectively. The system develops AF order below 130 K, consistent with the results of bulk transport measurements [63] and similar to other half-doped manganites [37, 45, 48–52].

To determine the low-temperature magnetic structure of PCMO, we made extensive surveys of reciprocal space and found that the allowed magnetic peaks are characterized by wavevectors $\mathbf{q} = (2n + 1/4, 2n + 1/4, l)$ and $(2n + 1/2, 0, l)$ with n and l being integers and half-integers, respectively [Fig. 2.1(b)]. Figure 2.3 summarizes scans along the l direction for the $(2n + 1/4, 2n + 1/4, l)$ (corresponding to the Mn^{3+} sites) and $(2n + 1/2, 0, l)$ (the Mn^{4+} sites) Bragg positions. The $l = m + 1/2$ ($m = 0, 1, 2, \cdots$) peaks are clearly magnetic because they disappear above the Néel temperature [Fig. 2.3(a)]. We note that the c-axis correlation length in PCMO is resolution-limited and long-ranged, in contrast to the short-range c-axis correlations in LSMO [102]. Magnetic structure factor calculations indicate two possible spin stackings of successive MnO_2 layers along the c-axis direction. As depicted in Fig. 2.2(a), spins in the $c/2$ MnO_2 layer simply shift from those in the $c = 0$ layer by $(a/2, a/2, c/2)$ or $(-a/2, -a/2, c/2)$. The stacking arrangements of Mn^{3+} sublattice are also

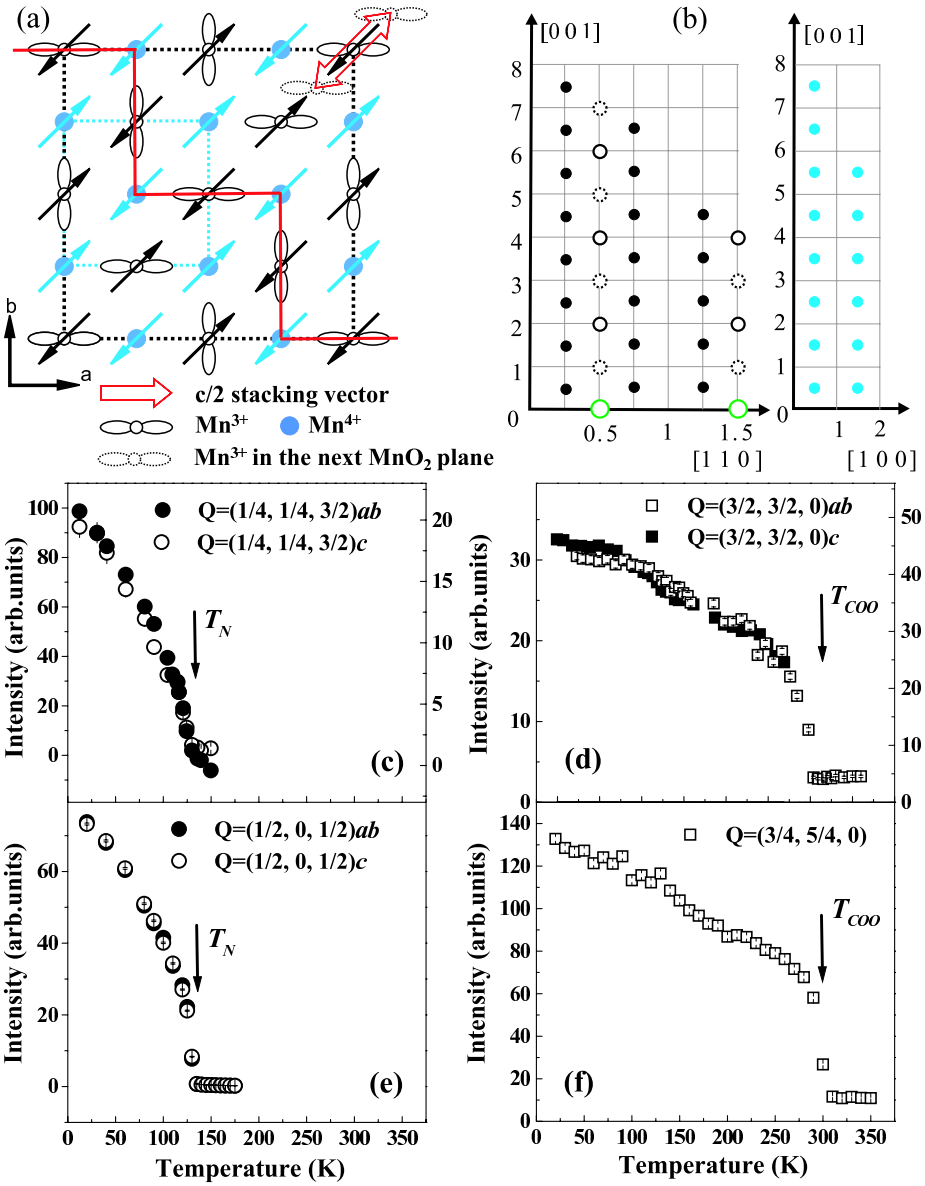

Figure 2.1: (a) Schematic view of the CE-type AF ordering in the MnO_2-plane. The black dashed line represents the periodicity of the unit cell for the Mn^{3+} sublattice, and the blue dashed line shows that of the Mn^{4+} sublattice. Possible spin arrangements in the $c/2$ stacking layers are marked by red arrows. The directions of Mn^{3+} orbitals form zigzag ferromagnetic chains (red line) that order antiferromagnetically. (b) The observed nuclear peaks (black open circles), CO-OO-induced superlattice peaks (green open circles) and magnetic ordering (solid circles) in reciprocal space. The dotted open circles represent the observed weak nuclear peaks that are disallowed by orthorhombic symmetry, indicating that the symmetry is lower than orthorhombic. Temperature dependence of the AF peak intensity from (c) (1/4,1/4,3/2); (e) (1/2,0,1/2) and temperature dependence of CO-OO peak intensity from (d) (3/2,3/2,0) and from (f) (3/4,5/4,0).

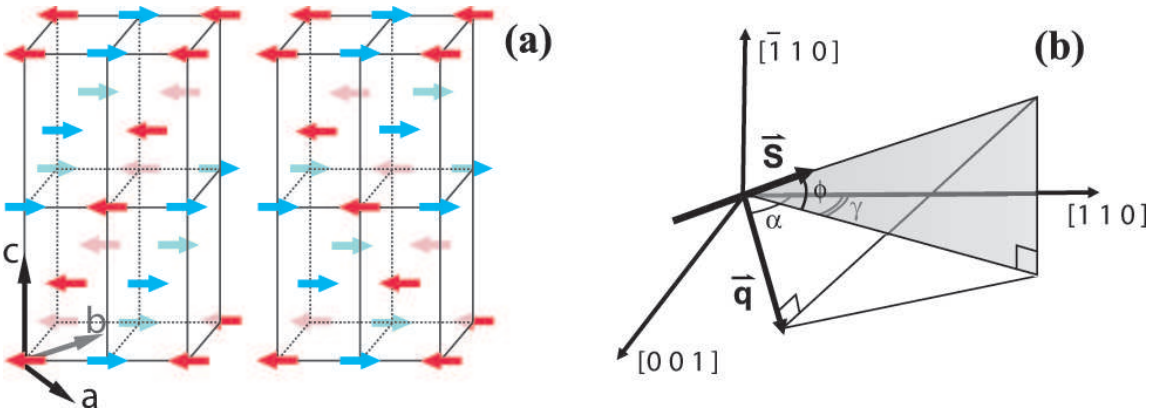

Figure 2.2: (a) Two possible spin arrangements for the Mn^{3+} sublattice as obtained from Rietveld analysis of the HRNPD data and fits to single crystal integrated intensities at different positions. (b) The geometrical relationship between the Mn^{3+} spin and the MnO_2 plane.

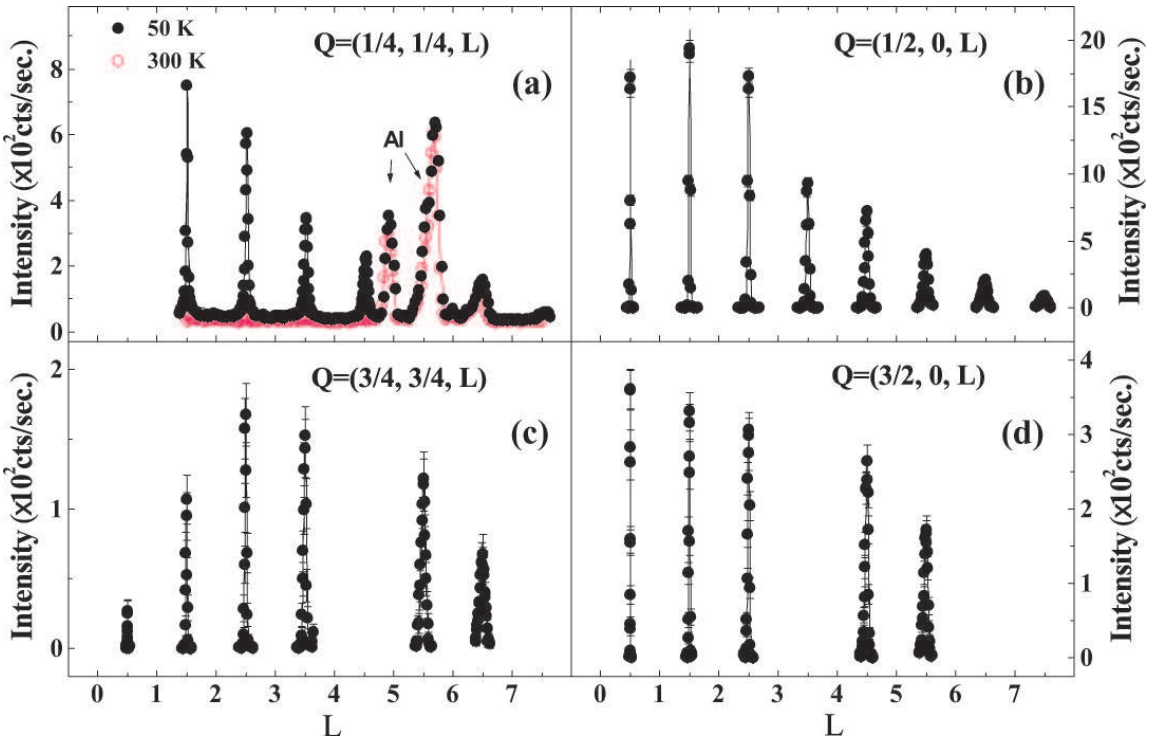

Figure 2.3: (a) Scattering data along **q**=(1/4,1/4,L) at T = 50 and 300 K, respectively. Panels (b), (c) and (d) show the $\theta - 2\theta$ scans for **q**=(3/4,3/4,L), (1/2,0,L) and (3/2,0,L) that are projected to the [0,0,L] direction.

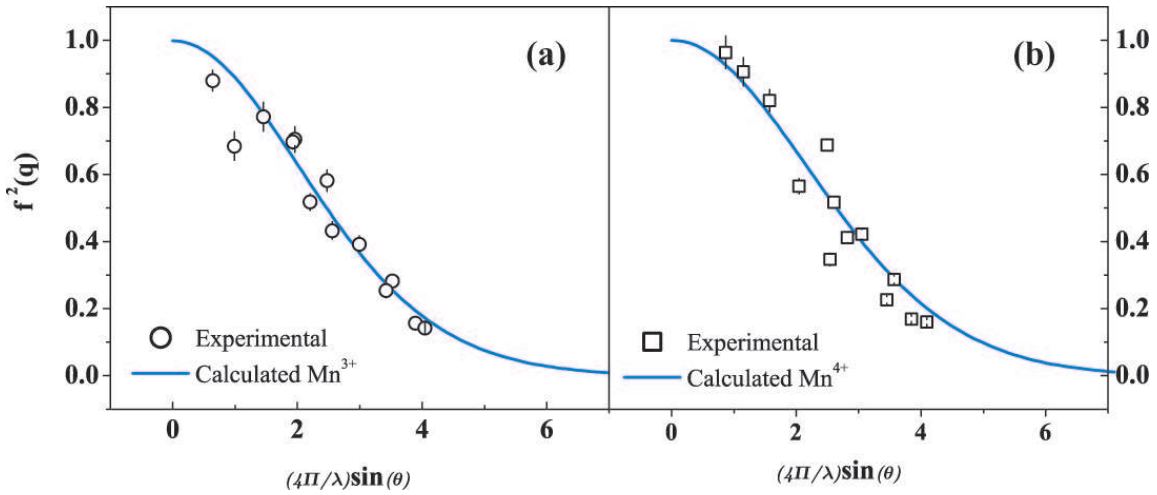

Figure 2.4: The intensities of observed magnetic peaks are fit to the generic magnetic form factor for (a) Mn^{3+} and (b) Mn^{4+} ions.

shown in Fig. 2.2(a). The resulting magnetic structure allows both $(2n+1/4, 2n+1/4, l)$ and $(2n+1/2, 0, l)$ peaks. There is no evidence of magnetic peaks at l-even $(2n+1/4, 2n+1/4, l)$ positions [Fig. 2.3(a)] as observed in LSMO [37]. The temperature dependence of the order parameters for the $(1/4, 1/4, 3/2)$ [Fig. 2.1(c)] and $(1/2, 0, 1/2)$ [Fig. 2.1(e)] peaks show that the Mn^{3+} and Mn^{4+} networks enter the AF long-range ordered states simultaneously at T_N ~130 K.

We measured the radial and transverse scans of all observed magnetic peaks. The product of the longitudinal peak width in full-width-half-maximum (FWHM) and the integrated intensity of the rocking curve was used as the total intensity of a Bragg peak. The observed intensity of a magnetic Bragg peak is expressed in equation (1.16) and (1.15). For convenience of reading, the two equations are repeated here:

$$I \propto \frac{|F_M(\mathbf{q})|^2}{\sin(2\theta)} \tag{2.1}$$

where θ is the scattering angle and $\sin(2\theta)$ is the Lorenz factor. The magnetic structure factor F_M is

$$F_M(\mathbf{q}) = \sum_j f(\mathbf{q})_j \mathbf{q} \times (\mathbf{M}_j \times \mathbf{q}) e^{i\mathbf{q}\cdot\mathbf{r}} e^{-W_j}, \tag{2.2}$$

where $f(\mathbf{q})_\mathbf{j}$, $\mathbf{M_j}$ and e^{-W_j} are the magnetic form factor, the spin moment of the j-th ion

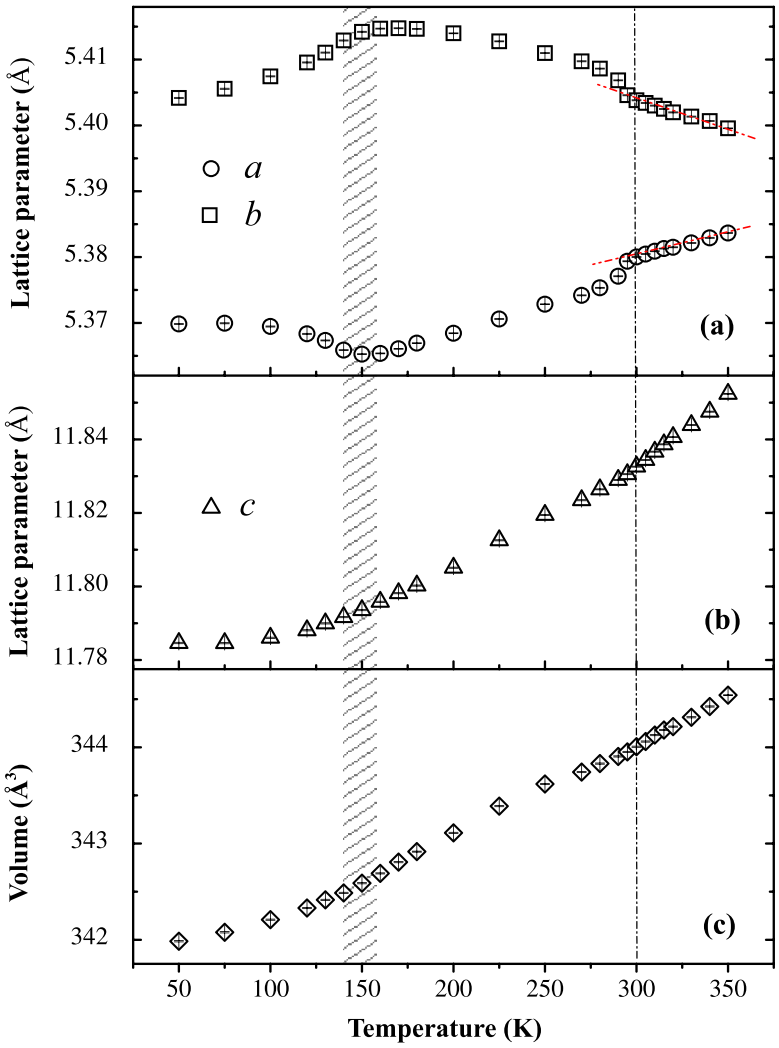

Figure 2.5: Temperature dependence of lattice parameters and unit cell volume. The dashed line near 300 K marks the CO-OO transition temperature T_{CO}. While the in-plane a and b lattice parameters show clear anomalies around T_{CO} and T_N, the c-axis lattice parameter changes smoothly across both transitions. The dash-dotted lines in panel (a) are guides to the eye.

and Debye-Waller factor respectively.

In the case of the Mn^{3+} spin network, the integrated intensities of $(2n+1/4, 2n+1/4, l)$ peaks depend on α, ϕ and γ, where α is the the angle between wave vector $\mathbf{q}$ and the MnO_2 plane, ϕ is the angle between the moment direction and the $[1,1,0]/[0,0,1]$ plane, and γ is the angle between the projection of the spins in the $[1,1,0]/[0,0,1]$ plane and the MnO_2 plane, as depicted in figure 2.2(b). By fitting the integrated intensities of $(2n+1/4, 2n+1/4, l)$ peaks as a function of α, ϕ and γ, we find that the best fit for the Mn^{3+} form factor in Fig. 2.4(a) requires both ϕ and γ to be zero, indicating that the Mn^{3+} spins are in the MnO_2 basal plane and along the $[1,1,0]$ direction [Figs. 2.1(a) and Fig. 2.2(a)]. Similarly, the moment direction for Mn^{4+} spins along the $[1,1,0]$ direction also gives the best fit [Fig. 2.4(b)]. Independent Rietveld analysis of the magnetic structural data on powder samples confirms that the magnetic structure has dimensions of $a_o \times 2b_o \times 2c_o$ (where a_o = 5.37 Å, b_o = 5.40 Å, and c_o = 11.78 Å at low temperature) for the Mn^{3+} magnetic sublattice and $2a_o \times 2b_o \times 2c_o$ for Mn^{4+} sublattice. Although the proposed spin directions of PCMO is different from that of LSMO, where spins are aligned along the $[1,2,0]$ direction in the MnO_2 basal plane, the presence of impurity and minority phase in LSMO makes the conclusive magnetic structural determination difficult [102].

2.4.2 Abnormal suppression of the CO/OO-induced orthorhombic strain

As PCMO is cooled from 350 K, the orthorhombicity of its structure increases with decreasing temperature and shows a clear enhancement of the orthorhombic strain around the charge ordering temperature T_{CO} to accommodate the establishment of orbital ordering. Figure 3 shows the temperature dependence of the lattice parameters and unit cell volume obtained from Rietveld analysis of the neutron powder diffraction data. While an enhancement of the orthorhombic structure near T_{CO} is expected, similar to that of other half-doped manganites [48–52, 102], the orthorhombicity of PCMO mysteriously becomes smaller below ∼150 K, at temperature 20 K above the T_N of the system (Fig. 2.5). To demonstrate this more clearly, we carried out detailed studies of the $(1,1,2)$ Bragg peak at temperatures 30 K$< T_N$, $T_N <$160 K$< T_{CO}$, and $T_{CO} <$320 K [Fig. 2.6(g)]. Below T_{CO}, the $(1,1,2)$ peak at 2θ=36.61° starts to broaden with reduced peak intensity, and

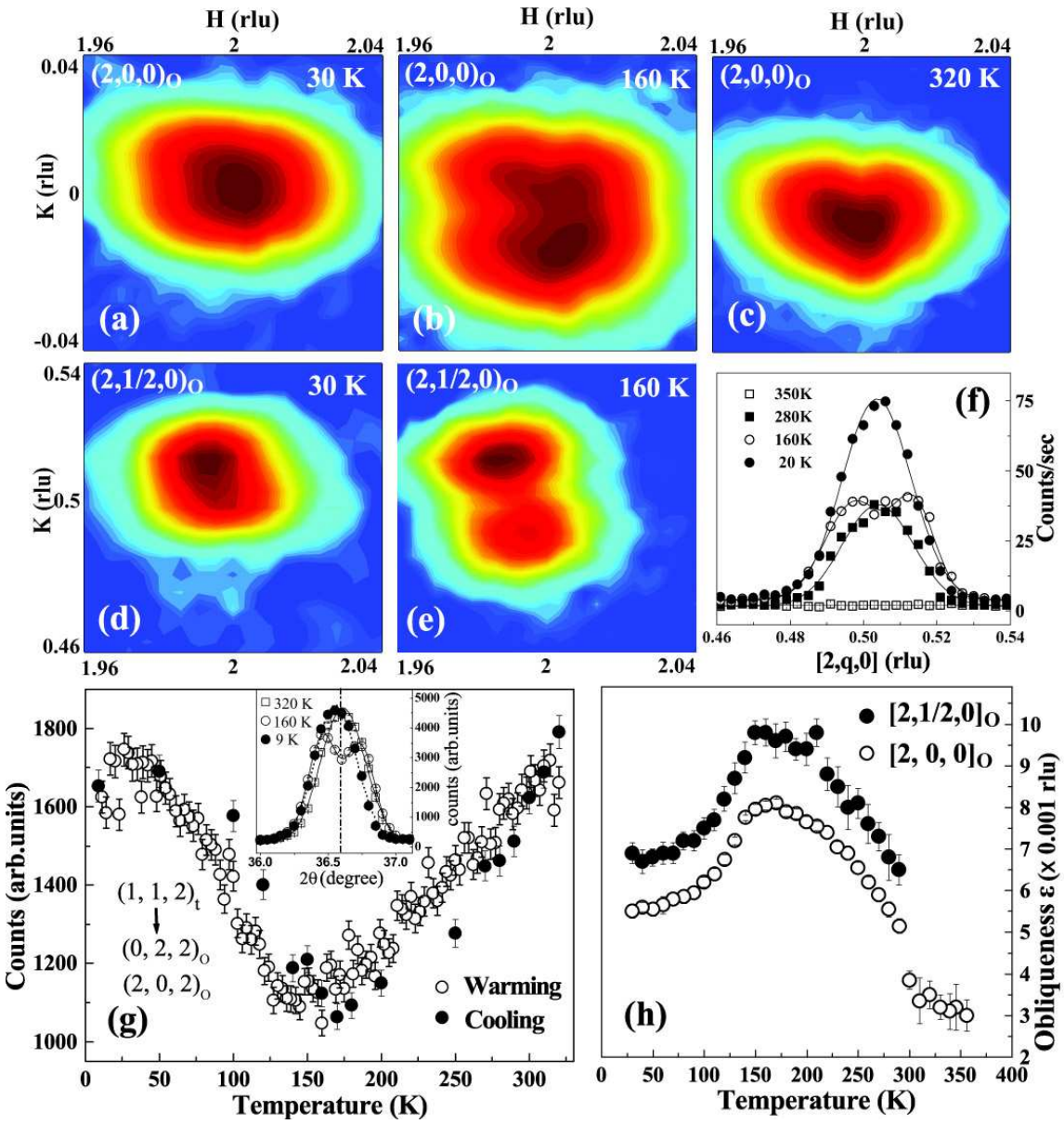

Figure 2.6: Strong spin-lattice coupling near the magnetic transition temperature. (a-c) Mesh-scans around the nuclear Bragg peak $(2,0,0)_O$ [in orthorhombic notation] at $T = 30$, 160 and 320 K. (d and e) The corresponding mesh-scans around CO-OO induced superlattice peak $(2,1/2,0)_O$ at 30 and 160 K. (f) wavevector scans of the same CO-OO peak at selected temperatures. (g) Temperature dependence of the peak intensity from powder monitored at 2θ=36.61°, which corresponds to $(1,1,2)_t$ structural peak in tetragonal notation. The inset shows the splitting of the $(1,1,2)_t$ peak [the actual $(0,2,2)_O$ and $(2,0,2)_O$ in orthorhombic symmetry] becomes much more prominent at 160 K and recovers back to one peak at low temperature. (h) Temperature dependence of the obliqueness, the separation between the center of the split peaks in reciprocal space, for $(2,0,0)_O$ and $(2,1/2,0)_O$.

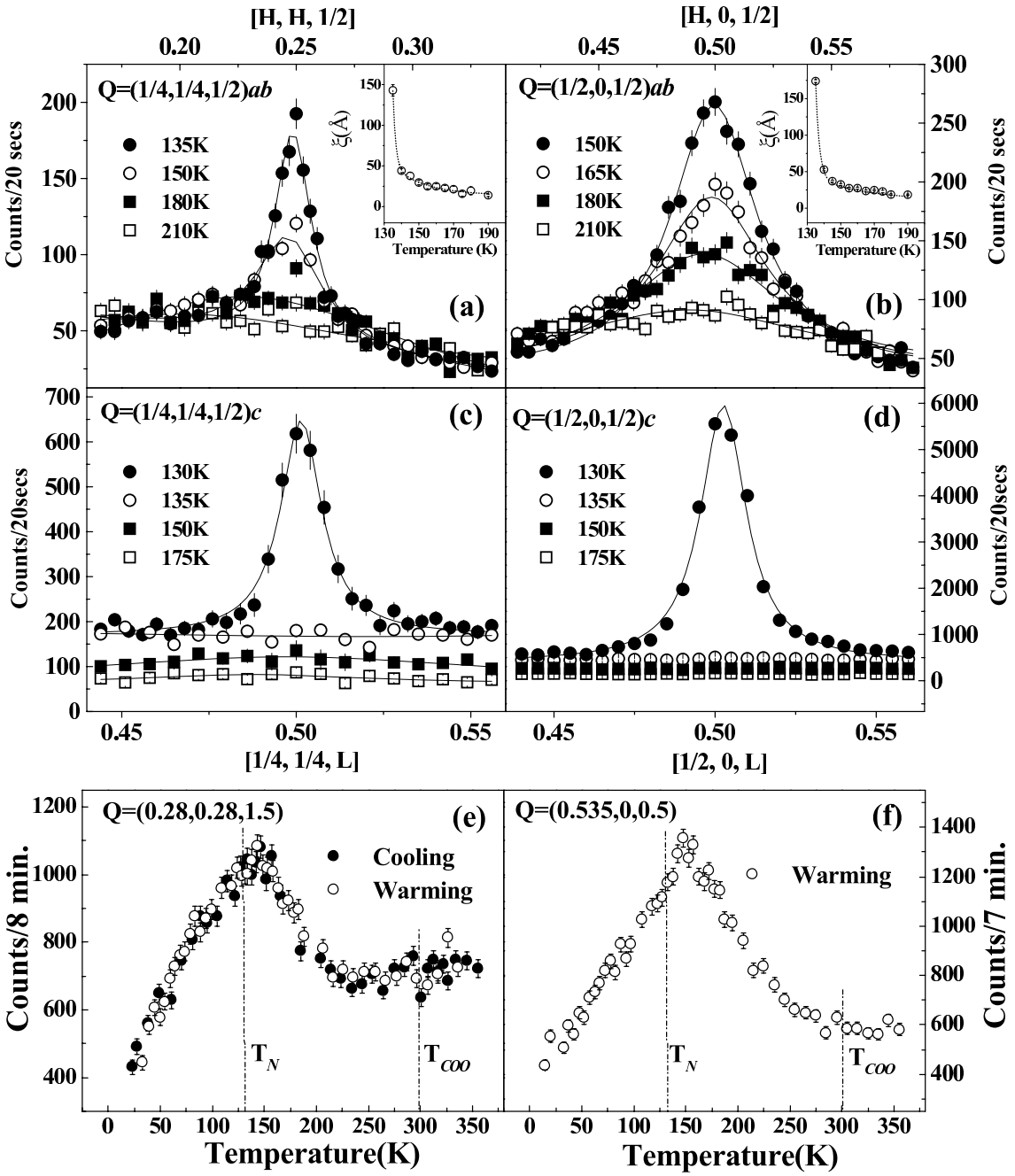

Figure 2.7: Crossover from two-dimensional AF fluctuations to three-dimensional AF order. Wavevector scans of AF scattering from the Mn^{3+} sublattice near $\mathbf{q} = (1/4, 1/4, 1/2)$ (a) within Mn-O plane and (c) along the inter-plane direction. Similar scans from the Mn^{4+} sublattice near (1/2,0,1/2) are presented in panels (b) and (d). Insets shows the evolution of magnetic correlation lengths above the long range AF order temperature $T_N =$ 130 K. (e) Temperature profiles of short-range magnetic scattering measured at (e) $\mathbf{q} = (0.28, 0.28, 3/2)$ and at (f) $\mathbf{q} = (0.535, 0, 1/2)$. Those wavevectors have been chosen to avoid the contamination from the magnetic Bragg peaks.

then splits into two peaks [indexed as $(0,2,2)_O$ and $(2,0,2)_O$ in orthorhombic notation] at $T \sim$150 K as shown in the inset of Fig. 2.6(g). As the temperature continues to drop, the split peaks merge back into one at low temperature. The temperature dependence of the $(1,1,2)$ peak intensity shows a continuous drop for $T < 300$ K and then the recovery below $T \sim$150 K [Fig. 2.6(g)].

Figs. 2.6(a-f) summarize mesh scans in reciprocal space near the fundamental Bragg $(2,0,0)_O$ and charge ordering $(2,1/2,0)_O$ positions in the orthorhombic symmetry at low, intermediate, and high temperatures obtained on single crystals of PCMO. The $(2,0,0)_O$ peak first broadens and then splits along the transverse direction at 160 K. On further cooling to 30 K, the split peaks become one again [Fig. 2.6(a)]. Figs. 2.4(d-f) show that the $(2,1/2,0)_O$ CO-OO peak, which is equivalent to the $(3/4,5/4,0)$ peak in tetragonal notation, exhibits similar behavior: broadens and splits between T_N and T_{CO}, and emerges back to one below T_N. To quantitatively determine the degree of orthorhombicity, we plot in Fig. 2.6(h) the temperature dependence of the separation between the centers of split peaks ϵ in reciprocal space. Below T_{CO} of 310 K, the distortion increases dramatically. It continues to increase and reaches its maximum around 150 K. Upon further cooling below $\sim$150 K (a temperature 20 K above T_N), the lattice distortion is continuously suppressed, but still remains at the lowest probed temperature of 20 K. This anomalous lattice response near T_N has not been observed in LSMO or other half-doped manganite systems. In these materials, the CO/OO induced lattice distortions do not exhibit noticeable anomaly across T_N at lower temperatures [48,49,52]. We also note that the suppression of orthorhombicity below $\sim$150 K in PCMO is not associated with the melting of charge ordering as the integrated intensity of CO peaks shown in Figs. 2.1(d) and (f) display no anomalies across T_N. This is different from bilayer perovskite manganites [64,65].

The temperature dependence of AF peaks such as $(1/4,1/4,3/2)$ and $(1/2,0,1/2)$ shows a T_N of 130 K for PCMO. Wavevector scans within the MnO_2 plane and along the c-axis [Figs. 2.7(a)-(d)] show quite anisotropic correlations above T_N. Scans along the $[h,h,1/2]$ and $[h,0,1/2]$ directions in the MnO_2 plane display the clear presence of two-dimensional short-range spin correlations above T_N. Figure 2.7(a) suggests that the in-plane Mn^{3+}-Mn^{3+} spin correlations are established at temperatures as high as 210 K, while the inter-plane Mn^{3+}-Mn^{3+} spin correlations are turned on only below T_N [Fig. 2.7(c)]. The spin

correlations between Mn^{4+} ions behave similarly as shown in Figs. 2.7(b) and 2.6(d). The short-range AF spin correlations have been fit to a Lorentzian line shape as shown in the solid curves in Figs. 2.7(a) and 2.7(b). Their linewidths decrease with decreasing temperature. Below T_N, the Lorentzian line shape is gradually taken over by a Gaussian component indicating the development of long-range AF order. The insets of Figs. 2.7(a) and 2.7(b) show the temperature dependence of the in-plane spin-spin correlation lengths. While the correlation lengths clearly diverge near T_N as expected with the establishment of the long-range AF order, there is no anomaly around $\sim$150 K.

One way to determine the temperature dependence of the staggered magnetic susceptibility is to track the scattering intensity at a wavevector position slightly away from the magnetic Bragg peak (to avoid the Gaussian component) but close enough to probe short-range spin-spin correlations. In a standard second order AF phase transition, one would expect the staggered susceptibility to increase with decreasing temperature, peak at the transition temperature and then decrease below T_N. Figs. 2.7(e) and 2.7(f) show the temperature dependence of the scattering intensity at $(0.28, 0.28, 3/2)$ and $(0.535, 0, 1/2)$, which probe the Mn^{3+} and Mn^{4+} spin-spin correlations, respectively. The susceptibilities corresponding to Mn^{3+} and Mn^{4+} spin correlations start to increase around 240 K. They reach their maxima at $\sim$150 K on cooling and are continuously suppressed below $T \sim$150 K, showing no anomaly across T_N. Currently, we do not understand why there is no anomaly in the spin correlation lengths at 150 K [see Figs. 2.6(a) and 2.6(b) Insets].

2.5 Discussion and conclusion

In general, CO/OO ordering is strongly coupled to the lattice, has a large energy scale, and occurs at higher temperatures than magnetic ordering. As a consequence, the development of magnetic order at low temperature usually has no effect on the lattice distortions induced by the CO/OO order. For previously studied half-doped manganites [37, 48–52], orbital ordering is always established simultaneously with charge ordering [58, 59]. In addition, the CE-type AF order occurring at low temperatures stabilizes the CO/OO ordered phase and the orthorhombicity of the system saturates below T_N [48]. Since PCMO has a smaller $A_{0.5}A'_{1.5}$ ionic radius and larger lattice distortion than that of LSMO, one would expect

CO/OO order in PCMO to be more robust than the magnetic order. Instead, the dramatic reduction of the orthorhombicity near T_N indicates a strong spin-lattice coupling that can influence the distortion already established by CO/OO ordering. At present, it is unclear why PCMO should behave differently from other half-doped manganites. Perhaps the small Pr/Ca ionic sizes and large lattice distortion in this material can enhance the CE-type AF superexchange interaction and make it comparable to the energy of CO/OO ordering. For LSMO, inelastic neutron scattering experiments [66] have shown that the ferromagnetic exchange coupling along the zigzag chain direction [see Fig. 1(a)] is about 5.5 times larger than that of AF exchange in between the chains ($J_{FM}/J_{AF} = 9.98$ meV/1.83 meV ≈ 5.5).

In the case of PCMO, our preliminary spin wave measurements based on the Hamiltonian similar to that reported in ref. [66] suggest that this ratio becomes $J_{FM}/J_{AF} =$ 8.7 meV/6.5 meV ≈ 1.34 [67]. Therefore, the AF exchange interaction is much stronger in PCMO than in LSMO, making a more robust AF CE structure with little anisotropy between a and b axis directions. This means that the AF order in PCMO prefers a tetragonal structure rather than orthorhombic [46], and provides a competing energy scale to the already established CO/OO ordering. In any case, our data clearly indicate that the magnetic exchange energy in PCMO is an important competing force and must be taken into account to understand its low temperature electronic properties. Furthermore, the spin-lattice coupling in PCMO is much stronger than that for other half-doped manganites.

In summary, we have carried out neutron scattering studies of the lattice and magnetic structure of the layered half-doped manganite PCMO. The system first displays CO/OO order and then develops CE-type AF order at low temperatures. We have discovered that AF order can have a large effect on the already established lattice distortions induced by the CO/OO. This result indicates a strong spin-lattice coupling in PCMO. It also contrasts with all other known half-doped manganites, where AF order has little or no influence on orthorhombic strains in the system. We argue that the reason for this difference is because magnetic exchange coupling in PCMO is much more isotropic, favoring a tetragonal AF crystal structure.

Chapter 3

Coexistence of commensurate and incommensurate magnetic scatterings in underdoped $Pr_{1-x}Ca_xMnO_4$

3.1 Introduction and motivations

Recent study of the hole-doped manganites ($R_{1-x}A_xMnO_3$) has been centered on the coexistence and interplay of various magnetic and electronic phases, which is believed to be responsible for the colossal magnetoresistance (CMR). Of particular importance is the insulating CE-phase, the collaborated charge/orbital/spins-ordered state that neighbors almost all other ordered phases in the doping-bandwidth phase diagram [68]. It has been discussed in Chapter 2 how the correlated orderings of spins lattice and orbital form the CE-type structure in the half-doped single layered $Pr_{0.5}Ca_{1.5}MnO_4$. The CE phase stabilizes at half doping ($x = 0.5$) of perovskite manganites of relatively small band width, where equal amount of Mn^{3+} and Mn^{4+} , together with orbitals of Mn-e_g electron, form antiferromagnetically coupled ferromagnetic chains. Although a few groups have reported that the disproportion of the two sites is less than one [69–72], the model originally proposed by Goodengouth [46] works perfectly for neutron scattering approach, so they will

continue to be dubbed as Mn^{3+} and Mn^{4+} in this work.

As hole density deviates from the half-doping, there is an asymmetry between the under- ($x < 0.5$) and over-doped ($x > 0.5$) systems in charge/orbital order (CO/OO) as well as in magnetic orders. For $x > 0.5$, the CO/OO survives longer doping range but the charge modulations become incommensurate [73, 74], and the magnetic ground state is usually anisotropic AFM; while for $x < 0.5$ the CO/OO remain commensurate [73, 75, 76], and most systems have FM magnetic ground state [77]. Various theoretical models involving topological invariance [100], Ginzburg-Landau theory [98], orbital solitons [99] and strong JT interaction [96, 97] have been proposed to explain this asymmetry. Despite remarkable theoretical efforts [78],

This chapter represents a systematic study of the magnetic correlations in the layered manganite $Pr_{1-x}Ca_{1+x}MnO_4$ (PCMO) using elastic neutron scattering technique. The long range, commensurate (CM) AF order observed at x=0.5 [63, 79] is suppressed with decreasing carrier (hole) concentration. The characteristic wave vectors associated with the CE-phase retain as hole concentration decreases from x=0.5. Remarkably, additional magnetic scatterings appear at incommensurate (ICM) positions near the CM peaks. It is no surprise that the robust CE-phase survives doping levels well below x=0.5, as happens in several perovskite manganites. The appearance of ICM magnetic scattering and the coexistence with their CM partners is unique to the single-layered PCMO systems. The electronic phase separation seems to be a good explanation for the coexistence of CM and ICM magnetic reflections, and a ubiquitous character of the doped manganites [80–82].

3.2 Experimental details

Single crystals of PCMO (mass $\approx$ 4 to 6 grams) were grown using the floating zone method. Each crystal has been checked by transport and magnetic susceptibility measurements to ensure the nominal carrier concentration. At room temperature, PCMO has orthorhombic structure slightly distorted from the tetragonal symmetry, with lattice parameters $a \approx 5.38\mathring{A}$, $b \approx 5.40\mathring{A}$ and $c \approx 11.85\mathring{A}$. To be consistent with the result of PCMO (x=0.5) systems, we use the tetragonal unit cell ($a = b \approx 3.84\mathring{A}$) for the neutron diffraction measurements. The experiments were carried out using triple-axis spectrome-

ters BT7 and BT9 at the NIST Center for Neutron Research. The neutron energy was fixed at E=14.7 or 13.5 meV using pyrolytic graphite crystals as monochromator, analyzer and filter. The momentum transfers $q = (q_x, q_y, q_z)$ in units of $\AA$ are at positions $(h, k, l) = (q_x a/2\pi, q_y b/2\pi, q_z c/2\pi)$ in reciprocal lattice unit (rlu). Scattering planes of $(h, k, 0)$, $(h, 0, l)$ and (h, h, l) are used in order to reach different magnetic reflections.

3.3 The CM and ICM magnetic peaks in underdoped PCMOs ($x < 0.5$)

Figure 3.1 shows the magnetic scattering from the Mn^{3+} sublattice for under-doped samples at 0.40. The measurements are carried out near the Bragg point (1/4,1/4,0) and equivalent positions at higher Brillioun zone at (1/4,3/4,0) and (3/4,3/4,0). A wide range of reciprocal space is surveyed in order to capture the short range ICM magnetic scattering. The scattering contains two parts, the first of which locates at the CM position, same as those observed at $x = 0.50$ [79]. The second feature is the ICM fluctuations at smaller wavevector $(1/4 - \delta/\sqrt{2}, 1/4 - \delta/\sqrt{2}, 0)$. This scattering reaches strongest near (3/4,1/4,0) and decreases in intensity near (3/4,3/4,0). These results confirm their magnetic origin and the fluctuating spins presumably lie in the MnO_2 plane with moments pointing along [1,1,0] direction [79], as discussed in the previous chapter. It should be noted that the ICM fluctuation extends in a much large momentum space and has a highly anisotropic scattering profile. The rode-like scattering elongates along the [1,1,0] (longitudinal) direction indicating a much shorter correlation length. As the hole doping increases, the diffusive ICM scattering sharpens and the peak gradually moves toward the CM position. At $x = 0.45$, the scattering remains anisotropic but the difference between two orthogonal directions becomes smaller. As displayed in wavevector scans in Figure 1, the longitudinal scan shows broad width comparing to the transverse scan along the [1,-1,0] direction. The correlation lengths, after deconvoluting the instrumental resolution, are estimated to be $\xi_L = 12.2 \pm 0.3\AA$ and $\xi_T = 20.2 \pm 0.4\AA$ at $x = 0.35$. These numbers become $\xi_L = 52.5 \pm 1.5\AA$ and $\xi_T = 66.5 \pm 1.8\AA$ at $x = 0.45$.

The investigation of the magnetic correlations from the Mn^{4+} spins is obtained by probing the scattering near the expected superlattice peak $(1/2, 0, 0)$. Figure 3.2 shows

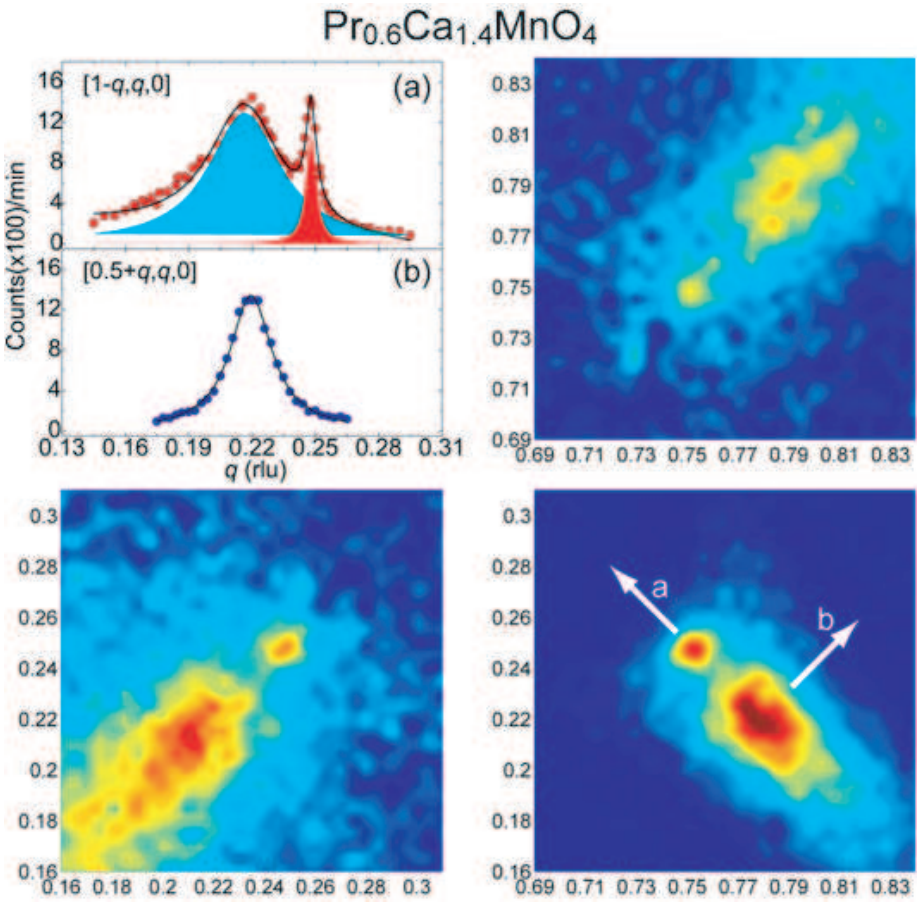

Figure 3.1: Contour plot of magnetic diffuse scattering from the Mn^{3+} sub-lattice at x=0.40. Panel (a) and (b) present the longitudinal and transverse wavevector scans across CM and ICM peaks. Arrows show the scan directions.

the contour plots and the wavevector scans for the PCMO (x=0.45). The prominent feature is the intense peaks at the CM positions surrounded by broad diffuse components. Although the CM scatterings appear to be much sharp than the ICM fluctuations, they have Lorentzian profiles and are broader than the instrument resolution, indicating that the system never achieves true long range order. Similar to the Mn^{3+} sublattice, the incommensurability of the diffuse scattering can be tuned by sample composition. As the ICM peaks moves closer to the CM position with increasing x, the width of diffuse peak narrows and the intensities become enhanced. Unlike the Mn^{3+} sublattice, the short range correlations is less anisotropic. The distance between the CM and ICM peaks remain the same at (0.5,0,0), (1.5,0,0) and (0,0.5,0), therefore we can rule out magnetic domains as the origin the the ICM peaks. Both CM and ICM peaks diminish at raised temperatures. We will discuss their temperature dependence in a later section.

3.4 Doping dependence of the incommensurability

As the doping goes from half-doped to lower (decreasing x) levels, the ICM peaks show up, broaden and deviate further from the corresponding CM positions. As shown in fig. 3.3(a), at $x = 0.5$, there is no ICM peaks around (0.25,0.25,0). The ICM peak shows up at about (0.23,0.23,0) at $x = 0.45$, and shifts to (0.22,0.22,0) at $x = 0.40$, then to (0.21,0.21,0) at $x = 0.35$. The linewidth of the ICM peak remarkably broadens at lower doping levels. Similar behavior has been observed for Mn4+ sublattice (data not shown). If we define the incommensurability as the distance δ between the CM and ICM peak positions, Mn^{3+} and Mn^{4+} sub-lattices have the same δ value and it shows strong doping dependence. Fig. 3(b) shows that the δ value increases as doping x decreases. It is 0, $\sim$0.025,0.042, and 0.063 at x=0.5, 0.45, 0.40, and 0.35 respectively.

3.5 Temperature dependence of the CM and ICM peaks

To further characterize the magnetic correlations, we plot the temperature dependence of the wavevector scans at $x = 0.45$ in Figs. 3.4(a) and 3.4(b). At T =10 K, the coexistence of the CM and ICM peaks are distinctly resolved. Upon warming, the scattering from both

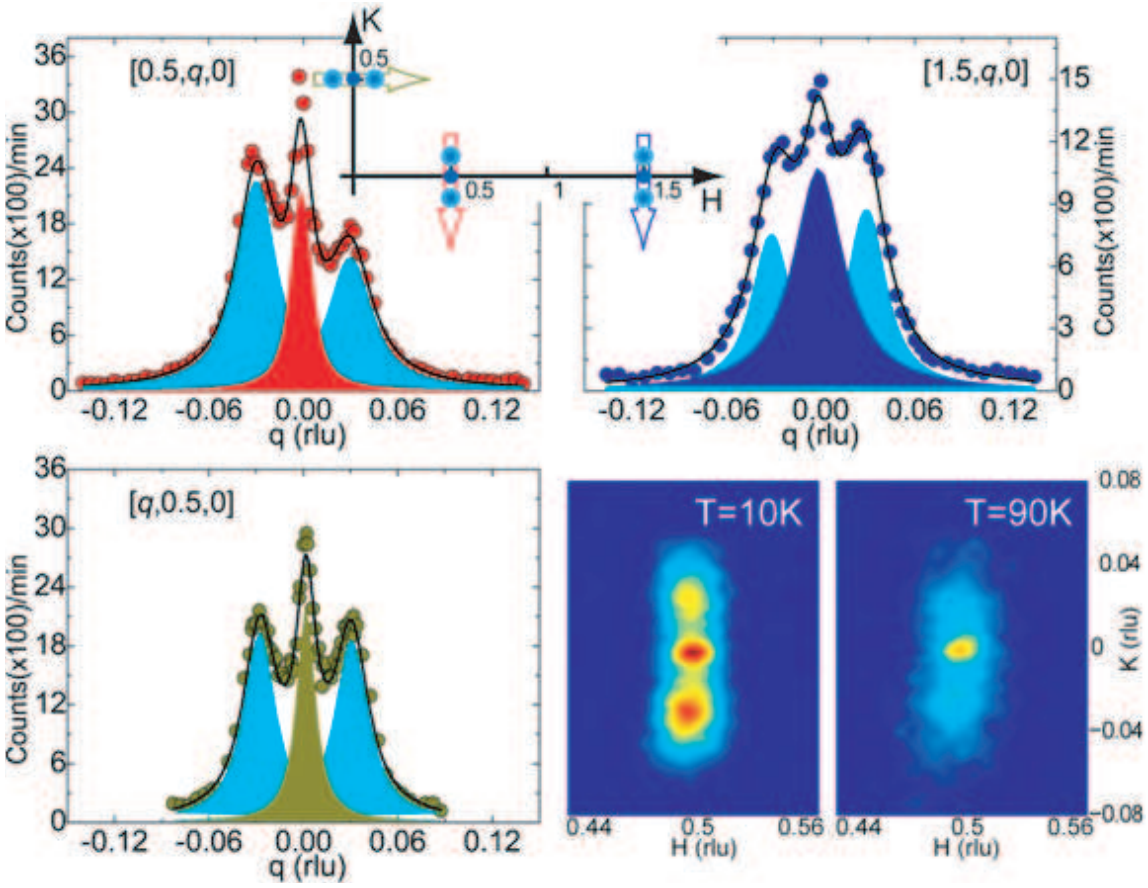

Figure 3.2: Transverse scans and the contour plots of the Mn^{4+} network. The distance between the CM and ICM peaks remain the same at (0.5,0,0), (1.5,0,0) and (0,0.5,0), therefore we can rule out magnetic domains as the origin the the ICM peaks. Both CM and ICM peaks diminish at raised temperatures.

Table 3.1: Doping dependence of the magnetic scattering correlation length ξ from the Mn^{3+} and Mn^{4+} sublattices. "L" and "T" denote the longitudinal and transverse directions.

$Pr_{1-x}Ca_{1+x}MnO_4$	$x = 0.35$	$x = 0.40$	$x = 0.45$
$\xi_L(Mn^{3+})$(Å)	12.2 ± 0.3	21.1 ± 0.4	52.5 ± 1.5
$\xi_T(Mn^{3+})$(Å)	20.2 ± 0.4	37.6 ± 0.9	66.5 ± 1.8
$\xi_{CM}(Mn^{3+})$(Å)	116.8 ± 4.5	139.4 ± 6.4	127.1 ± 6.6
$\xi_{ICM}(Mn^{4+})$(Å)	9.8 ± 1.1	15.9 ± 1.3	44.6 ± 1.4
$\xi_{CM}(Mn^{4+})$(Å)	131.4 ± 2.8	127.3 ± 5.3	121.0 ± 7.2

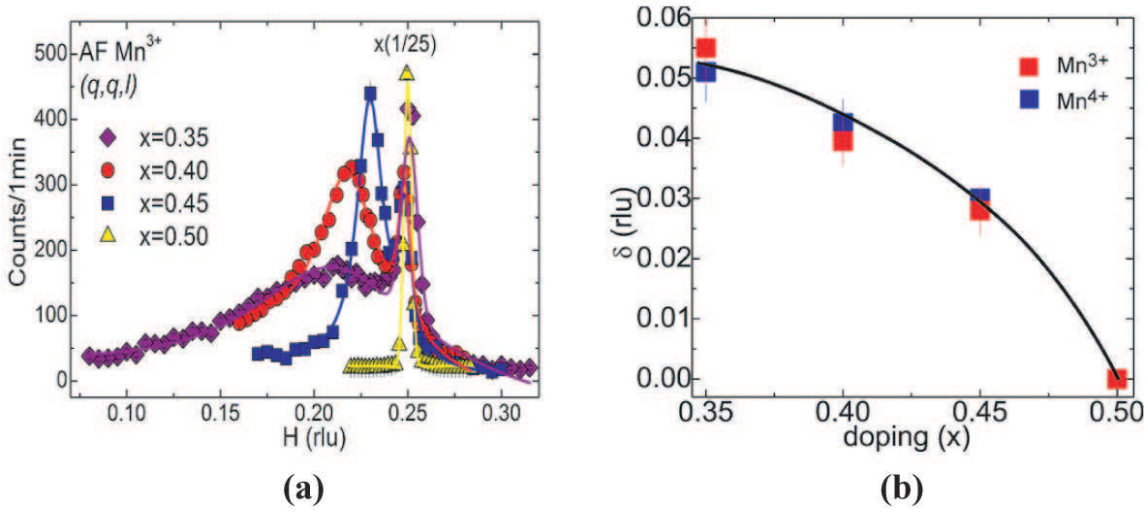

Figure 3.3: (a) The radial scans of the Mn^{3+} magnetic site (0.25,0.25,0) for PCMO x=0.35,0.4 and 0.45. (b) Doping dependence of incommensurability from both Mn^{3+} and Mn^{4+} sublattices.

magnetic sublattices show very similar behavior. The amplitude of the ICM peak is rapidly suppressed with little variation in peak position. In addition, the ICM scattering evolves into broad feature as temperature is raised. The scattering profile of the CM component, on the other hand, remains well resolved at a much higher temperature. Figs. 3.5(a) and (b) compares the thermal evolution of the peak intensities of the doped samples. The concave shape of the peak intensity as a function of temperature from the ICM scattering indicates the expected diffusive nature for the short-range fluctuation, in contrast to the convex functional form for the CM magnetic order, which behaviors like a typical order parameter. It should be noted that the ICM fluctuations become much weaker in intensity at lower doping.

Fig. 3.6 shows L-scan on the (a) Mn^{4+} CM site [0.5,0,L] and (b) Mn^{3+} ICM site [0.78,0.22,L] for the PCMO (x=0.4) sample. The CM sites show the survival of c-direction correlation through peaks $(0.5,0,L/2)$ at low temperature. The linewidths of these peaks, though, are broader than those in the half-doped system and are not resolution limited (data not shown), indicating short-range correlations between the MnO_2 planes. No peak is observed for the L-scans on the ICM sites.

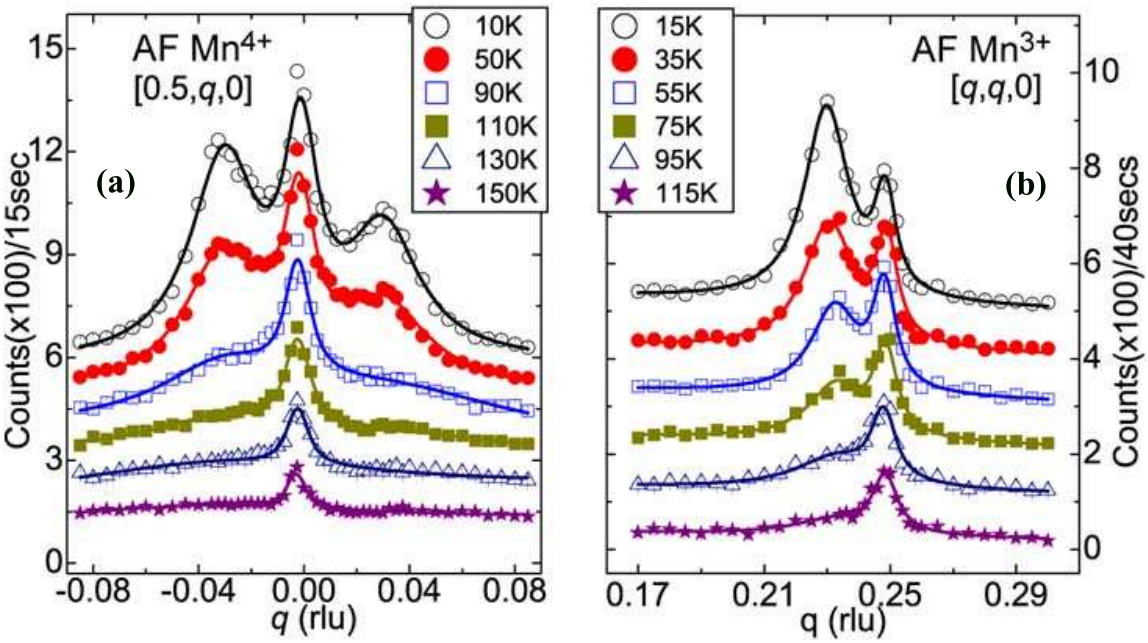

Figure 3.4: Temperature dependence of (a) transverse scans of the Mn^{4+} site (0.5,0,0) and (b) radial scans of the Mn^{3+} site (0.25,0.25,0).

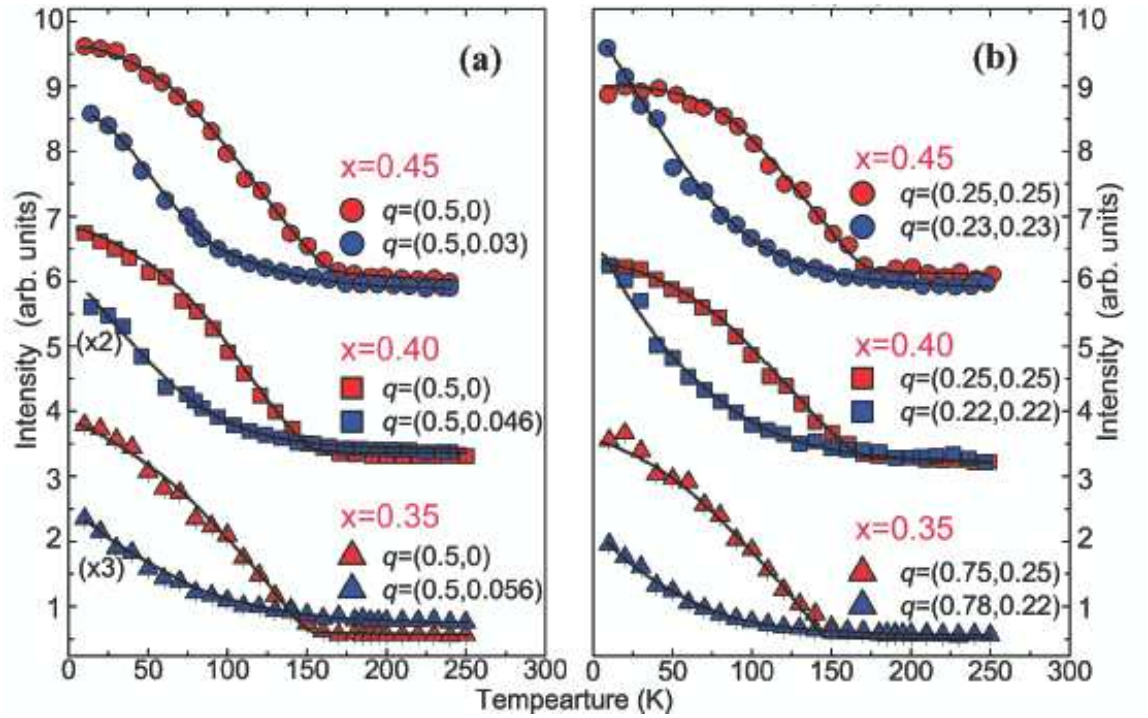

Figure 3.5: Temperature dependence of peak intensities at the CM positions (red) and ICM positions (blue) from (a)Mn^{4+} and (b)Mn^{3+} sublattices for $x < 0.5$.

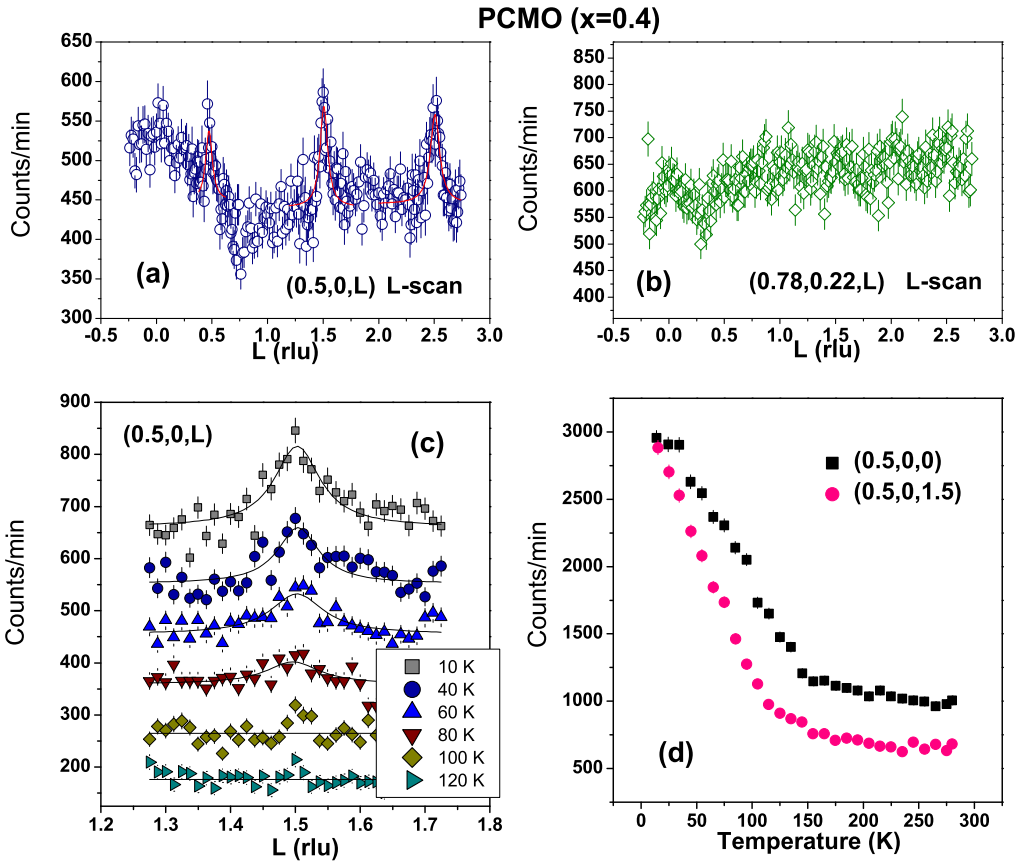

Figure 3.6: L-scan on the (a) Mn^{4+} CM site [0.5,0,L] and (b) Mn^{3+} ICM site [0.78,0.22,L]. (c) Temperature dependence of the profile and (d) the intensity of the (0.5,0,0) and the (0.5,0,1.5) peak.

3.6 The possible explanations for the ICM reflections

The suppression of the long range CM magnetic order and the surprising emergence of the ICM short range fluctuations in PCMO are markedly different from the perovskite $Pr_{1-x}Ca_xMnO_3$ and other insulating manganites, where the CE-type spin order extends to broad carrier doping [83, 84]. Our results clearly demonstrate the electronic phase separation in this layered compound, regardless of controversial existence of distinct Mn^{3+} and Mn^{4+} site [85–88]. There are several possible scenarios that could explain the appearance of ICM scattering. One is the formation of the CDW and associated spin density wave (SDW) due to the charge incommensurability [89]. In this picture, the overall magnetic structure resembles the checkerboard spin configuration, but the amplitudes of the spins have a smooth spatial modulation in order to accommodate the extra electrons. This configuration naturally brings about the ICM magnetic peaks. However, it will also produce symmetric satellite peak at equivalent wavevector $q = (1/4 + \delta/\sqrt{2}, 1/4 + \delta/\sqrt{2}, 0)$ with same spectral weight [90], which contradicts the experimental observation.

Another possible origin of the ICM peak is the stripe phase similar to those observed in the high-T_C superconductor cuprates [91] and proposed in manganese oxides [92, 93]. At doping below $x = 0.5$, the system tends to form magnetic clusters/domains which preserve the CE-type spin configuration. Different from the CDW/SDW case, the neighboring Mn sites could have distinct moments (S=2 and 3/2 for Mn^{3+} and Mn^{4+}, respectively). The excess electrons congregate at the domain boundary with random spin and orbital orientations. A variety of real-space spin arrangements have been explored in order to reproduce the experimental results. Two of them best characterize the observations. The first one [Fig. 1(c)] describes a diagonal domain boundary separating two anti-phase magnetic clusters. The individual magnetic domain contributes to the CM scattering, while ICM peak arises from the correlation between domains. This configuration reproduces the magnetic scattering originating from the Mn^{3+} sites, but leaves the scattering near (1/2,0,0) undisturbed. The second one [Fig. 1(d)] describes spin arrangements with a horizontal domain boundary. There is extra phase shift (1/4 or 3/4 of the $4a_c$, the periodicity of CE-phase) between adjacent magnetic domains. It introduces two symmetric ICM peaks at $q = (1/2, \pm\delta, 0)$ but not at $q = (0, 1/2 \pm \delta, 0)$. As demonstrated in Fig. 1(e), the Fourier

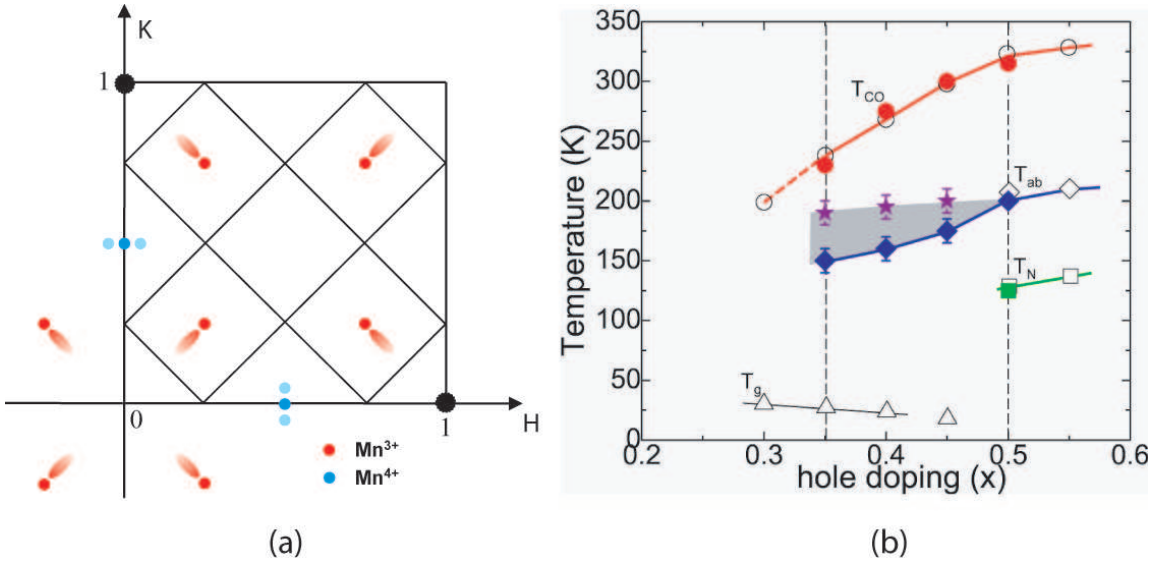

Figure 3.7: (a) Schematics of the experimental observation in reciprocal space. (b) Phase diagram of the single layer manganite $Pr_{1-x}Ca_{1+x}MnO_4$.

transformation of those configurations successfully create the pattern similar to the experimental results with some minor discrepancy. For example, the anisotropic character of the ICM scattering from the Mn^{3+} sublattice is not reflected. The experimental data might suggest the actual CE-type domains have longer FM chains, a result observed in CO-OO perovskite manganite [51]. Another noticeable feature is the remarkable doping dependence of the incommensurability and the correlation lengths of the ICM scattering. Although the origin of ICM scatterings in our model could be completely independent, the good agreement of the incommensurability from the both magnetic sublattices clearly suggest their common origin.

It was recently pointed out that the quenched disorder is important in determining the stability of the CE-type magnetic phase [94]. Monte Carlo simulations by Alvarez *et al.* suggest that a small amount disorder/randomness in 2D or 3D system may destroy that phase. The inherent quenched disorder in PCMO caused by A-site solution is considerably small ($1 \sim 2 \times 10^{-7}$ for the doping range we studied) because of their comparable Pr^{3+}/Ca^{2+} ionic size. Therefore, the preservation of CE-type fluctuations at lower doing in PCMO confirm that the CE-phase could be a robust feature, in contrast to the quick disappearance of much distorted LSMO [95]. On the other hand, the striking difference

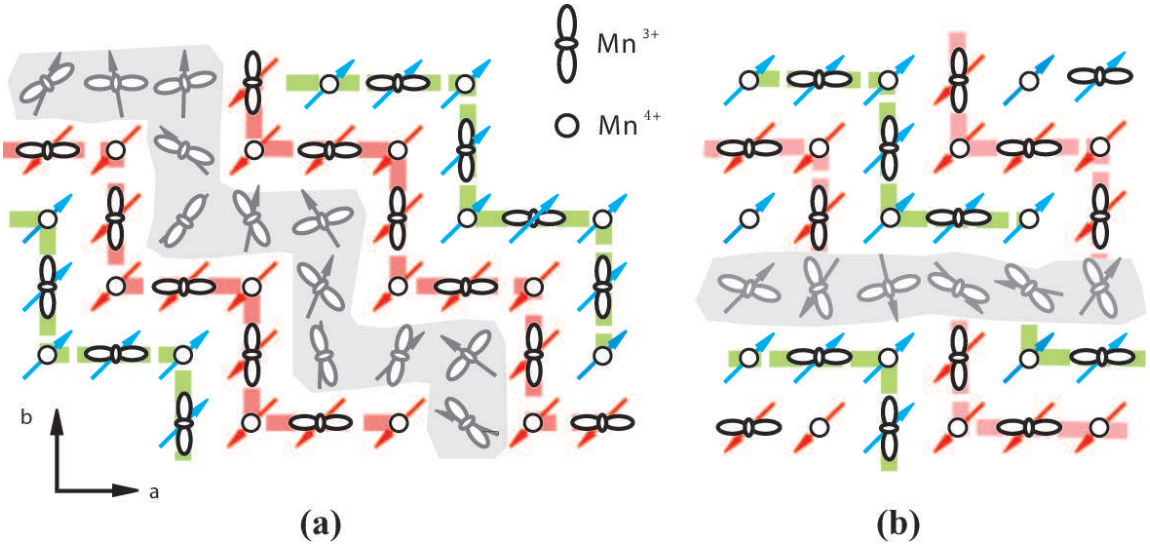

Figure 3.8: Coexistence of the commensurate and incommensurate magnetic scatterings on the Mn^{3+} sites.

between PCMO and the perovskite manganites highlight the crucial role of the magnetic interactions between planes, which is believed to stabilize the CE-type order [**?**].

3.7 Conclusions

Figure 1(b) summarizes the main finding of our neutron scattering results. In doped manganites with long range CO-OO and magnetic order, the Mn spins form two magnetic sublattices. The characteristic wavevector associated with the Mn^{3+} spins appears at the $q_1 = (1/4, /1, 4, 0)$ and the corresponding wavevector for the Mn^{4+} spins is at $q_2 = (1/2, 0, 0)$. For under-doped PCMO, in additional to the CM magnetic Bragg peaks at q_1 and q_2, there are incommensurate (ICM) magnetic fluctuations appearing at $(1/4 - \delta/\sqrt{2}, 1/4 - \delta/\sqrt{2}, 0)$ and $(1/2, \pm\delta, 0)$, respectively. The incommensurability (defined as the distance δ between the CM and the ICM peak) from both sublattices show strong doping dependence [Figure 1(f)].

To summarize, we have presented the neutron scattering studies of the single layer manganites PCMO. Although the same CM magnetic scattering is observed with much reported charge/orbital ordered perovskite manganites, we show the presence of highly anisotropic ICM magnetic fluctuations with carrier concentration below the commensurate

doping $x = 0.5$. The propagation wavevector and spin correlation of the ICM scattering are composition tunable. We demonstrate that the electronic phase separation with textured spin configuration is a robust feature in this layer transition metal oxides.

Chapter 4

Magnetic excitations in the nearly half-doped single layered $\mathbf{Pr_{0.55}Ca_{1.45}MnO_4}$

4.1 Introduction and motivation

How the electrons are distributed in the doped manganese oxides (manganites) remains as one of the most intriguing phenomena in condensed matter physics. In perovskite manganites, electrons and their corresponding magnetic spins often self organize into a textural pattern in certain narrow-band, insulating manganites. For example, checkerboard-like CE magnetic configuration is observed in $Pr_{1-x}Ca_xMnO_3$ and $La_{1-x}Ca_xMnO_3$ around $x = 0.50$. It has been reported that such co-operative ordered phase forms even when the system has unequal mount of electrons and holes. Despite numerous theoretical and experimental investigations, it is unclear whether such order is universal in insulating manganese oxides.

What seems to add to the the complication is the newly discovered incommensurate (ICM) magnetic fluctuations in addition to the suppressed typical CE commensurate ones in the under-doped $Pr_{1-x}Ca_{1+x}MnO_4$, as presented in the previous chapter. This co-existence has never been observed in any other manganites including the single-layered $La_{1-x}Sr_{1+x}MnO_4$.

The single-layered $Pr_{1-x}Ca_{1+x}MnO_4$ (PCMO) has weak quenched disorder due to the similar size of ion Pr^{3+} and Ca^{2+}. The cooperative ordering of charge, orbital and spin in half-doped PCMO [101] is very similar to that of the $La_{0.5}Sr_{1.5}MnO_4$ (LSMO) [102]: the system first becomes charge- and orbital-ordered (CO/OO) on cooling from high temperature, then enters the CE-type antiferromagnetic order. The main difference is the orthorhombic strain in PCMO, as distinct from the tetragonal structure of LSMO, promotes more ordering along c-direction. As reported in Chapter 2, the CO/OO induced orthorhombic distortion was suppressed by the appearance of short-range AF spin correlations, indicating a strong spin-lattice coupling. In the systems of deficient holes with respect to the half-doped (x=0.5) case, namely, when extra electrons are introduced into the CE-type cooperative ordering state, an incommensurate (IC) set of magnetic scatterings was observed in addition to the persistent CE AF peaks. These IC scatterings exhibit different features for Mn^{3+} and Mn^{4+} sites, as shown in fig. 4.3(b). The IC peaks for Mn^{3+} are along the diagonal directions and those for Mn^{4+} along [h,0,0] or [0,k,0]. In order to understand the mechanism producing such magnetic coexistence, the measurements on dynamic magnetisms are needed. Any change in the magnetic excitations from slightly under-doped to half-doped system would provide the insight on what extra electrons do to the CE phase.

In this chapter I will report the observation of two sets of magnetic excitations in the slightly under-doped PCMO systems: a magnon that is traceable to the standard CE-type spin arrangement of the x=0.5 system; and a dispersionless mode arising from the incommensurate spin positions. This strongly suggests two types of spin dynamics originated from separated phases: the mainly intact CE-type magnetic phase and an additional electronic phase caused by extra electrons introduced into the CE template.

4.2 Experimental details

The single crystals of PCMO were grown using the traveling solvent floating zone technique as described in Chapter 2. Three high quality single crystals of PCMO (x=0.45) were mounted on separate goniometers and coaligned, as shown in figure 4.1. Elastic and inelastic neutron scattering measurements were carried out on the triple-axis spectrome-

ter BT-7, BT-9, and SPINS at the NIST Center for Neutron Research and on HB-1 at High Flux Isotope Reactor at the Oak Ridge National Laboratory. At room temperature, PCMO has orhtorhombic structure (space group *bmab*). For simplicity, we use tetragonal unit cell with lattice parameters $a = b = 3.813\mathring{A}$, and $c = 11.831\mathring{A}$. The wave vector $\mathbf{q} = (q_x, q_y, q_z)$ is in the unit of $\mathring{A}^{-1}$ and $(h, k, l) = (q_x a/2\pi, q_y a/2\pi, q_z c/2\pi)$ is in reciprocal lattice units (rlu).

4.3 Glassy nature of the surviving CE-phase in underdoped PCMO

As discussed in the previous chapter, although depicted as tetragonal for convenience, the nuclear lattice of the PCMO systems is actually orthorhombic with lattice constance $\sqrt{2}$a along [1,$\bar{1}$,0] direction and $2\sqrt{2}$a along [1,1,0] direction, as shown in figure 3. The zig-zag chains are along [1,$\bar{1}$,0] direction. The Mn^{3+} spins contribute to magnetic superstructure reflections with $\mathbf{q} = \pm(0.25, -0.25, 0)$ or $\mathbf{q} = \pm(0.25, 0.25, 0)$ depending on the probed twinning domain; while the Mn^{4+} spins contribute to positions with $\mathbf{q} = \pm$(0,0.5,0) or $\mathbf{q} = \pm$(0.5,0,0).

Figure 4.2(a) and (b) display the temperature dependence of the magnetic of the peaks on the Mn^{3+} and Mn^{4+} sites respectively. On cooling the CM magnetic order starts to grow first, followed by the ICM intensities. The integrated intensities of both CM and ICM peaks from Lorentzian fits exhibit smooth growth without an abrupt transition, a typical spin glass (SG) feature. Spectrometers of different resolutions have different sensitivities to the time scale. Thus the magnetic peaks of SG state should have different temperature dependence for different spectrometers, or the same spectrometer with different configurations. The measurements with $E_f = 14.7meV$ on BT7 and BT9 are compared to those with $E_f = 3.7meV$ on SPINS at NCNR, as shown in figs. 2(c-d). The great contrast indicates the glassy nature of both CM and ICM states. This is in agreement with ac-susceptibility measurement [105] where the frequency-dependent cusp suggests a spin glass state.

Figure 4.1: Assembly of $Pr_{0.55}Ca_{1.45}MnO_4$ single crystals coaligned for inelastic neutron scattering measurements on SPINS, BT7 and HB1.

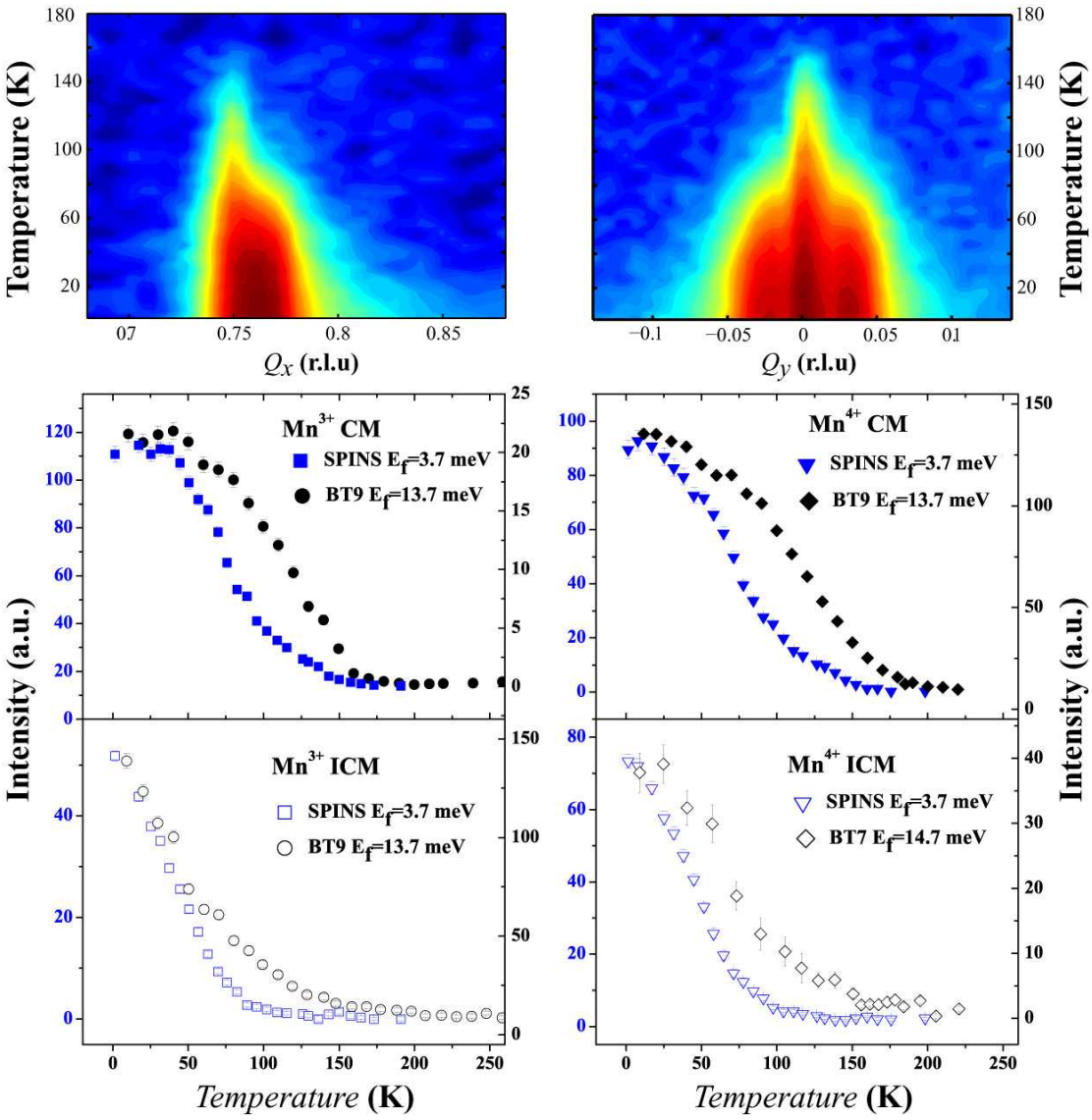

Figure 4.2: Temperature dependence of the CM and ICM peaks on the Mn^{3+} and Mn^{4+} sites with different spectrometer.

4.4 Coexistence of two types of magnetic excitations

The (0.75,0.75,0) magnetic Brillouin zone, equivalent to the $(-0.25, -0.25)$ was chosen for the magnetic excitation measurement to be able to close triangle and to avoid the focusing issue. Proceeding from the zone center (0.75,0.75,0), as shown in figure 4.3(b), the direction [0.75+q,0.75+q,0] ($\Gamma - A$) leads to the zone boundary (0.875,0.875,0) and [0.75-q,0.75-q,0] ($\Gamma - A'$) leads to boundary $(0.625, 0.625, 0)$. Both directions probe the coupling between the zig-zag chains. The two directions are equivalent in the half-doped system. However, in underdoped compounds, the two directions are no longer symmetric about the zone center because of the ICM peaks that are present only in the [0.75+q,0.75+q,0] direction. We observed two sets of magnetic excitations in this direction: one dispersionless excitation at 1 meV that decreases in intensity as the propagation wave vector deviates from the incommensurate (ICM) magnetic peak position (0.77,0.77,0); another magnon-like excitation that disperses toward higher energies as the wave vector propagates from center to boundary. In the $\Gamma - A'$ direction the localized mode is not present , but the dispersion mode still is (Fig. 4.4(a)).

The localized mode is obviously from the ICM sites because it appears only in the $\Gamma - A$ direction, and its intensity decreases as **Q** deviates from the ICM peak position (0.77,0.77,0) as shown in Fig. 4.3(b). While the dispersive mode appears in both $\Gamma - A$ and $\Gamma - A'$ directions and is symmetric about the zone center, therefore originates from the commensurate (CM) magnetic sites. It is not possible to probe the nature of the localized mode using temperature variation because the it is soon overwhelmed by the onset of diffuse scattering, as shown in Fig. 4.4(c). We also measured the temperature dependence of the dispersive mode on the side of the zone where there is no ICM reflection at $(0.7, 0.7, 0)$. Fig. 4.5(b) shows that the magnetic excitation at 4.5 meV broadens and shifts to lower energy, the typical softening of a magnon.

In the transverse direction [0.75+q,0.75-q,0] ($\Gamma - B$) in which the intra-chain coupling is probed, it makes no difference propagating to the two boundaries. Although there are no ICM peaks in this direction, the vicinity to ICM positions yields strong presence of the localized mode at small propagation wave vectors, which decreases in intensity as the wave vector becomes further away from the ICM position. Another dispersive mode is also

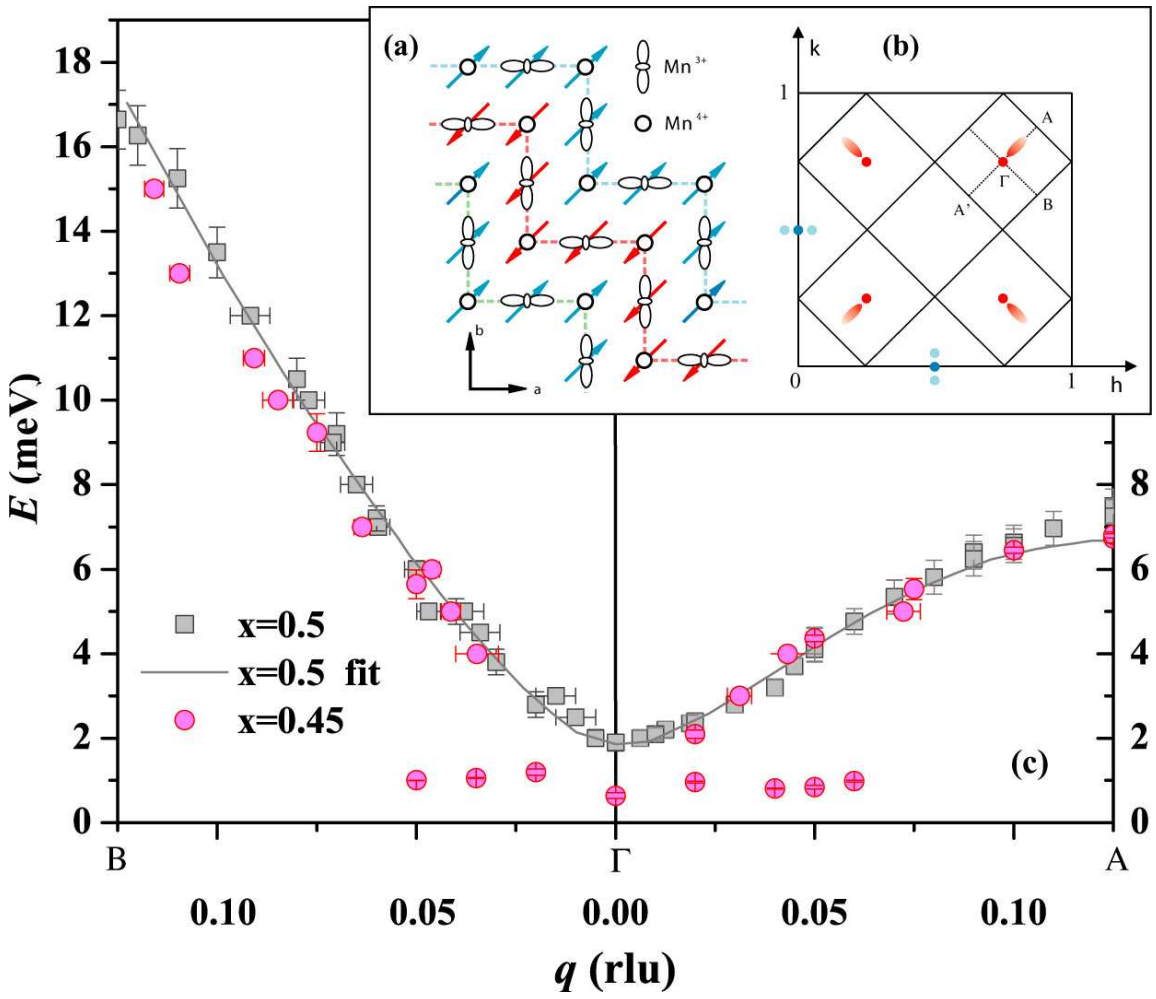

Figure 4.3: Spin wave dispersions of $Pr_{1-x}Ca_{1+x}MnO_4$ with x=0.5 (gray) and x=0.45 (red). The inset (a) shows schematic view of the CE-type correlated ordering phase in the ab plane of half-doped manganites in real space and (b) shows the magnetic Brillouin zone of the nearly half-doped PCMO.

obvious to see, different from the one in the inter-chain direction.

Although the geometry of incommensurability on the Mn^{4+} sites are different, the magnetic excitations are similar. Since the ICM peaks appear on both side of the CM peak in the transverse direction, the only way to contrast the excitation with ICM and the one without is to compare the measurements in transverse and longitudinal directions. In case of the (0,0.5,0) zone, it is to compare the magnetic excitations in the [0,0.5+q,0] and [0+q,0.5,0] directions respectively, which are the mixed directions in terms of zig-zag chains. Due to the closeness of the longitudinal [0,0.5+q,0] **Q** positions to the ICM peaks and the relatively large chosen q, the contrast is not as prominent as on the Mn^{3+} sites. But the existence of two types of excitations, a dispersionless mode at 1 meV and a dispersive magnon, is clear enough.

With the observed co-existence of two modes, one naturally asks if this is a result of two separated phases. Neutron scattering is a bulk probe, it is difficult to determine if the observed IC peaks arise from parts of the sample that are phase separated from the CE-structure parts of the samples. One way to test this hypothesis is to follow the dispersive magnon and see if it is the same or similar to that of the standard CE-type magnetic structure. If the answer is yes, we can safely conclude that extra electrons in the CE-phase form a new phase that coexists with the surviving CE-phase.

4.5 The dispersive magnetic excitation

At the zone center (0.75,0.75,0), as shown in fig. 4.4(a), there is a magnetic excitation at about 2 meV that appears as a shoulder on the localized excitation at about 1 meV. This suggests that the gap in the x=0.45 system is the same as that in the half-doped system. The magnon dispersions at high energies have been measured on BT7 at NCNR and HB3 at HFIR. The red circles in fig. 4.7 show the raw data scans, including constant-energy scans (fig.4.7(a)) and constant-**Q** scans (fig.4.7(b)). The dispersion along the zigzag chains ([1,1,0] direction) is much steeper than that along the inter-chain ([1,$\bar{1}$,0]) direction. This is very similar to the LSMO (x=0.5) [66] and PCMO (x=0.5) systems. At the magnetic zone boundaries **A** and **B**, the magnon energies are at 7 meV and 16 meV respectively.

In order to directly compare the spin wave in the slightly under-doped PCMO com-

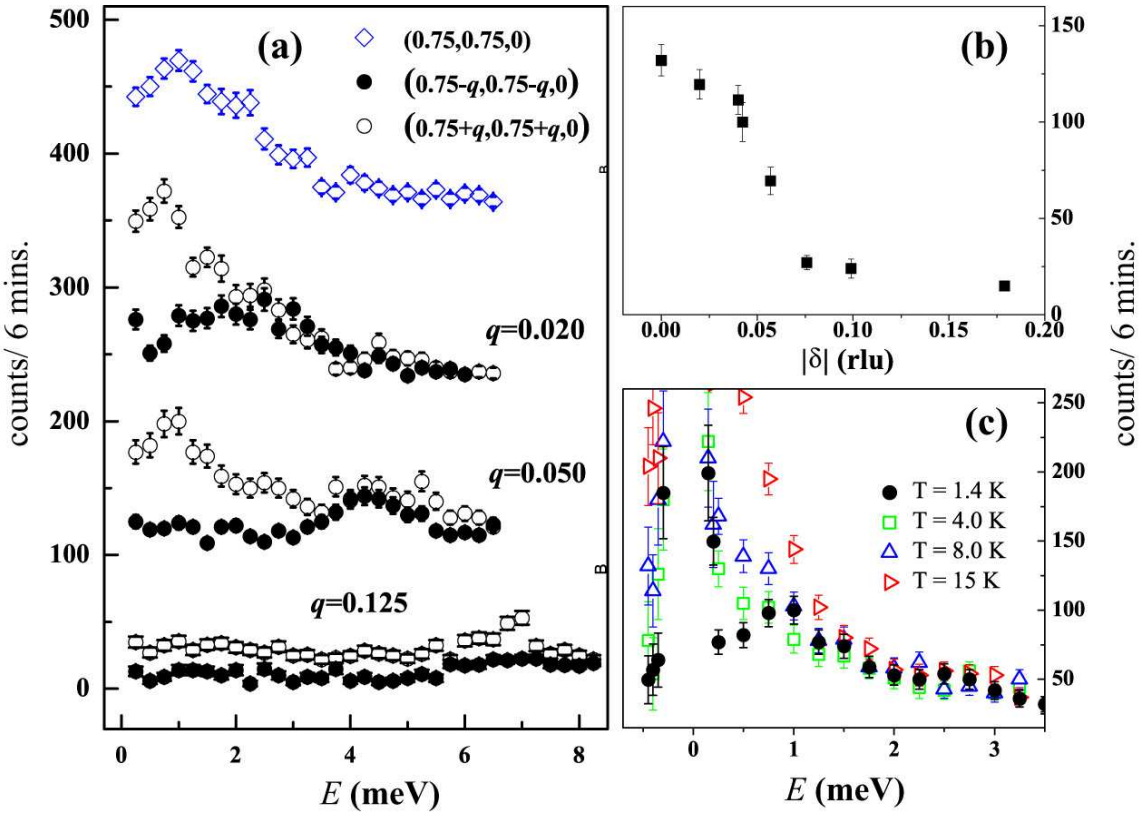

Figure 4.4: (a) The observation of two types of magnetic excitations with wave vectors of the same magnitude but different directions: the open symbols represent the scattering approaching the zone boundary where there is the CM magnetic fluctuation; and the solid symbols denotes the scattering in the opposite direction. (b)The intensity of the localized mode at ∼1 meV has the maximum at the ICM peak position (0.77,0.77,0) and decreases quickly as the wave vector deviates from it. The value $|\delta|$ denotes the absolute value of the deviation from the ICM peak. (c) The mode at ∼1 meV is overwhelmed by diffuse scatterings at low temperatures.

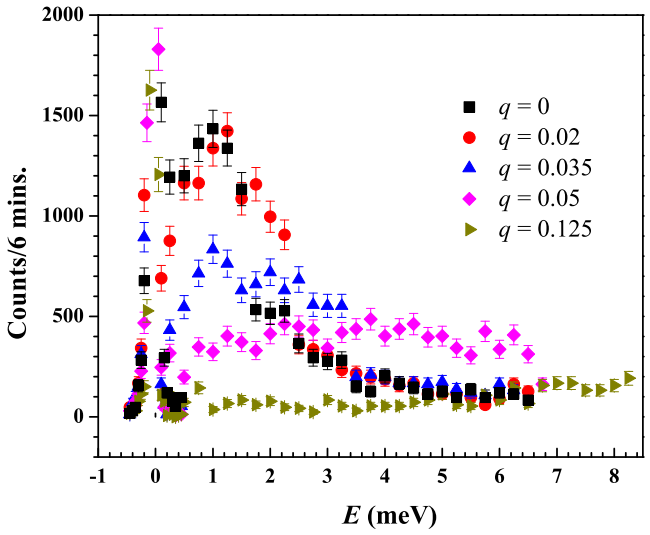

(a)

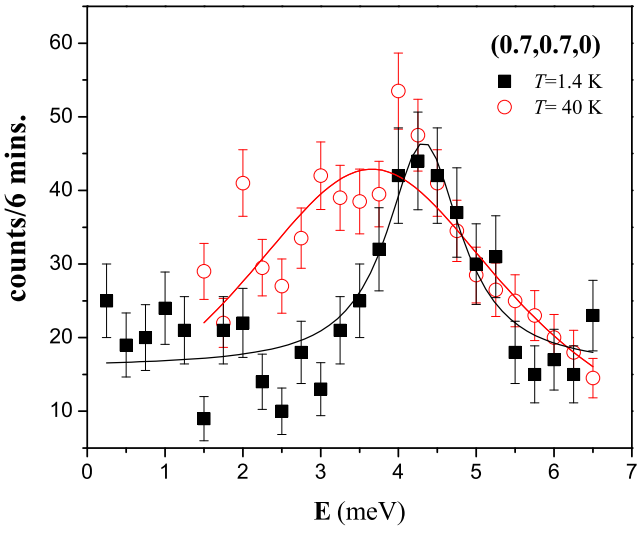

(b)

Figure 4.5: (a) Magnetic excitations in the $\Gamma - B$ direction. (b) The temperature dependence of magnetic excitation at $\mathbf{Q}$ =(0.7,0.7,0).

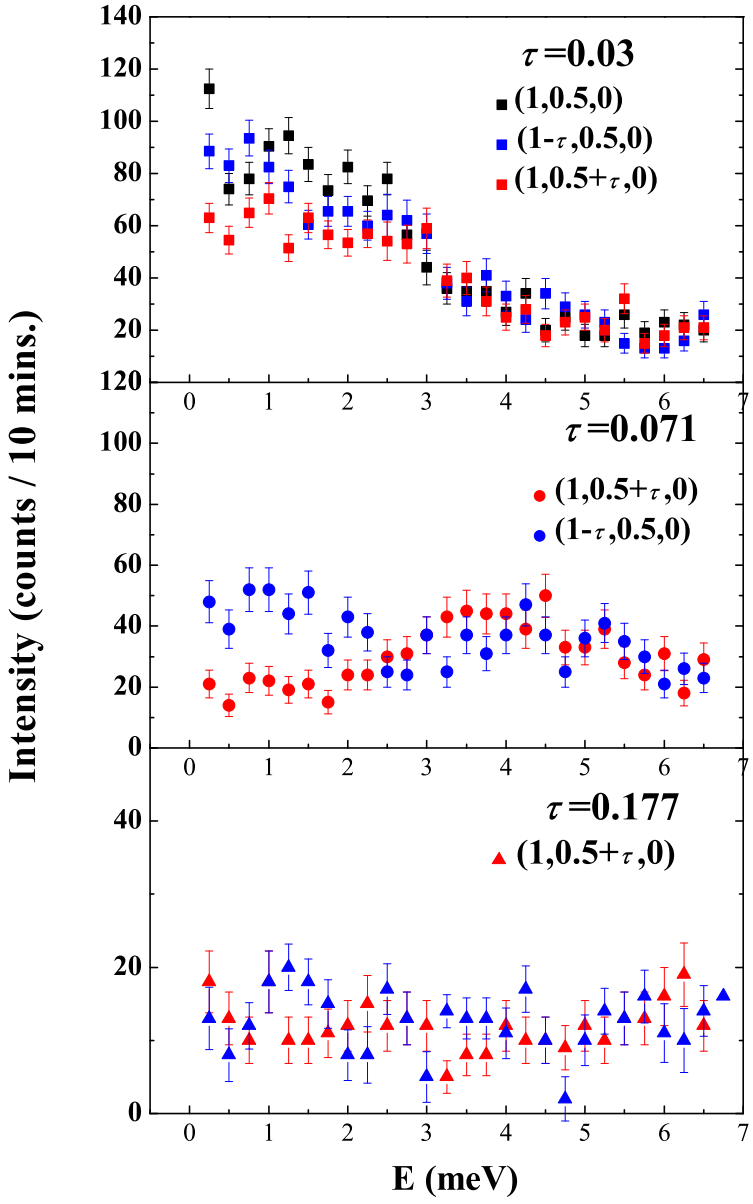

Figure 4.6: Coexistence of the commensurate and incommensurate magnetic scatterings on the Mn^{4+} sites.

pound to that in the half-doped system, we carried out identical constant-**Q** scans in the $\Gamma - A$ direction on HB1 with identical configuration. Phonons of these two systems were measured, as shown in fig.4.8, and used to normalized the intensities of the magnetic scatterings. Figure 4.7(b) compares the magnons of these two systems in the $\Gamma - A$ branch. Obviously the overall magnetic scattering is remarkably suppressed in the x=0.45 system. The E-scan peaks are broadened and much weaker in the underdoped compound. There is also a slight softening at the boundary. However, the magnon dispersions of these two systems are almost identical, intra-chain and inter-chain directions alike, as summarized in figure 4.3. This suggests that the CE phase, unable to compromise its generic format to accommodate extra electrons, is broken into patches with its initial CE structure intact within the patches.

4.6 Magnetic excitations in PCMO(x=0.35)

As discussed in the previous section, the attempt to probe the temperature dependence of the localized magnetic excitation at $\sim$1 meV was not successful because of the diffuse scattering that surmounts this mode at low temperatures. Another way to investigate this nature of this excitation is study its doping dependence.

Single crystal of PCMO (x=0.35) of about 3 grams has been used on cold neutron triple-axis spectrometer (TAS) SPINS and direct geometry NG4 Disc-chopper time-of-flight spectrometer (DCS) at NCNR. The sample was aligned in the $(H, K, 0)$ scattering plane for both spectrometers. For the DCS measurement, the orange cryostat was used as the sample environment and incident beam of wavelength 3.5 $\mathring{A}$ was chosen. The contour plot of the elastic channel (figure 4.9(a)) confirms the TAS observation of CM magnetic peaks at (0.25,0.25,0), (0.75,0.75,0) and (0,0.5,0), as well as their corresponding ICM peaks. The DCS measurement shows no clearly defined excitations around 1 meV that was observed for PCMO (x=0.45). Figure 4.10 shows inelastic cold neutron scattering measurements on SPINS using the same idea as plotted in figure 2.4. The (0.75,0.75) magnetic Brillouin zone was chosen to avoid the focusing complexion. The wave vector propagates from the zone center to two opposite directions, $[1, 1, 0]$ and $[\bar{1}, \bar{1}, 0]$. Again, two different behaviors were observed for the two supposedly identical scans. An obvious diffuse intensity appear

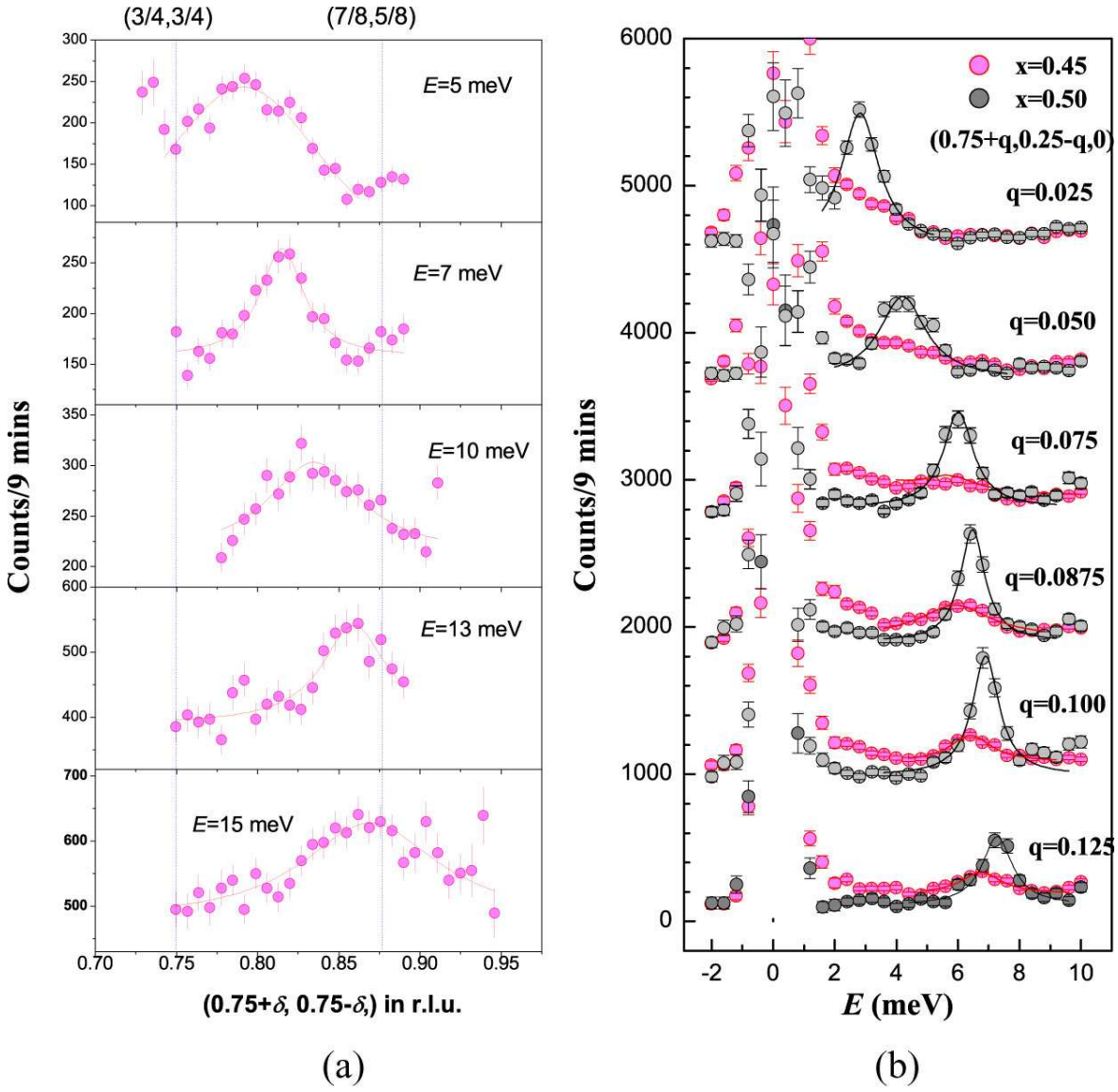

Figure 4.7: (a) Raw data Q-scans to determine the magnon dispersion in PCMO (x=0.45) (b) Magnetic excitations raw data of the E-scans in the $\Gamma - B$ direction for PCMO (x=0.5 black circle) and (x=0.45 pink circle).

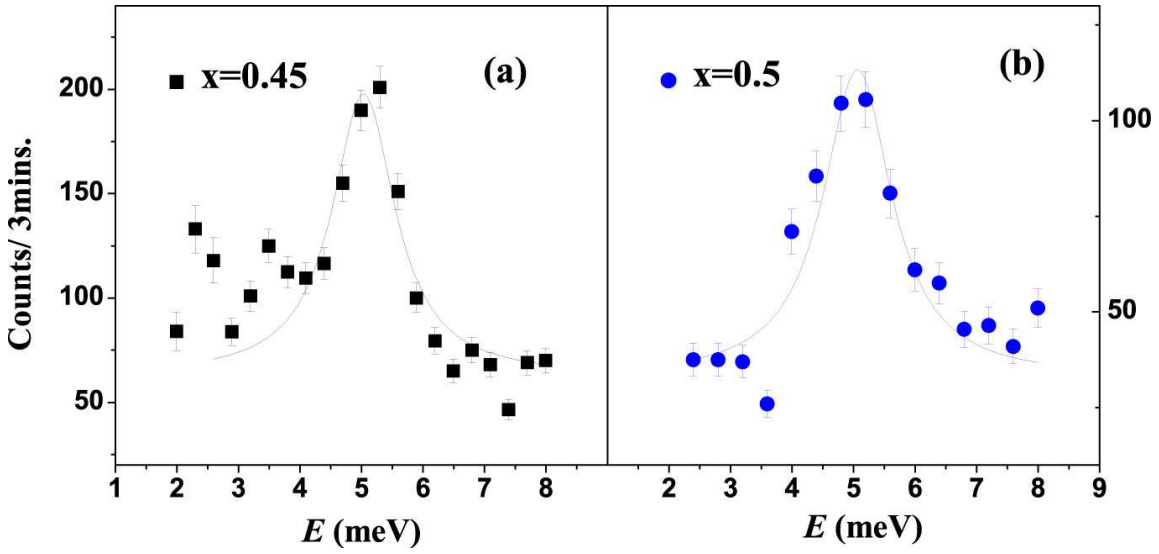

Figure 4.8: Phonons are measured for PCMO x=0.45 (a) and PCMO x=0.5 (b), and used to normalized the intensities of the constant **Q** scans of these two compounds.

in the $[1, 1, 0]$ direction where there is ICM peak, but is not present in the $[\bar{1}, \bar{1}, 0]$. In figure 4.10, energy scans of wave vectors of same quantity but opposite direction are plotted. The localized magnetic excitation observed in x=0.45 system is not present in the PCMO (x=0.35). The diffuse scattering that is unique to the ICM side does not change its intensity as in the PCMO (x=0.45). There is neither a sign of a magnon for $E < 7\ meV$. Figure 4.11 shows a **Q**-scan with $E = 1\ meV$. It is clear that the diffuse scattering occurs only on the side of the zone where ICM magnetic fluctuation appears.

The presence of the localized magnetic excitation in the PCMO (x=0.45) system and its absence in PCMO (x=0.35) suggests that local mode is not a result of the ordering of the extra-electron-induced new phase. This is because in the x=0.35 system where there are more electrons, the diffuse scattering that is related to the ICM magnetic fluctuation is more predominant. It is more reasonable to think this mode as a result of domain wall motion, which diminishes as domain walls increase in size and eventually turn into a paramagnetic phase that is separated from the CE-type ordered phase.

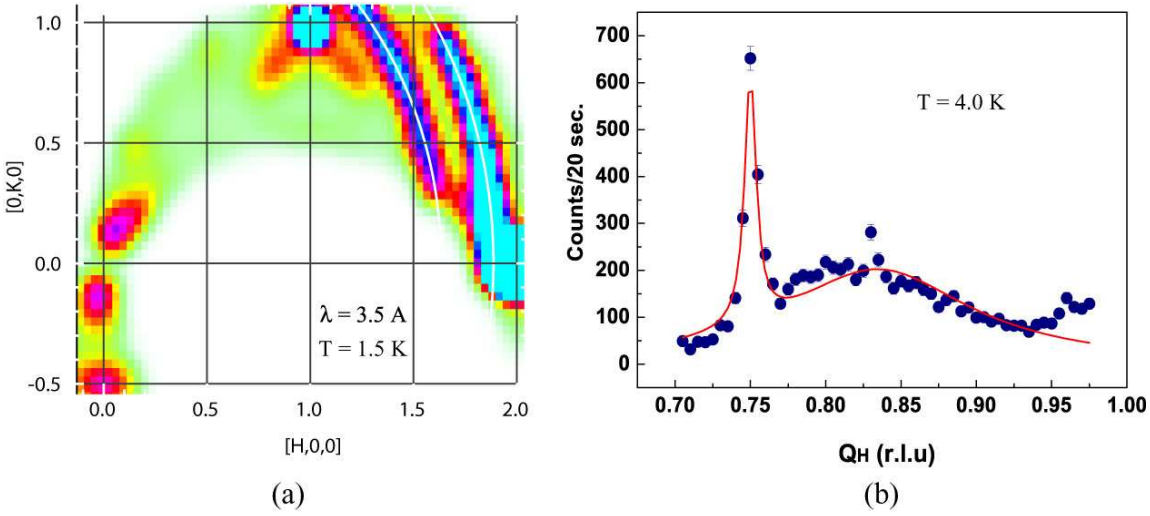

Figure 4.9: Confirmation of commensurate and incommensurate magnetic scatterings in the PCMO (x=0.35) system. (a) Contour plot of the (H,K,0) plane of the PCMO (x=0.35) measured with DCS, which shows the nuclear peak, CM and ICM magnetic peaks. The white arcs represent the Brag scattering of Al. (b) Radial scan in the (0.75,0.75,0) magnetic Brillouin zone that shows CM and ICM magnetic peaks.

4.7 Conclusions

Neutron scattering has been used to study the nature of the coexistence of the commensurate and incommensurate magnetic peaks in the under-doped $Pr_{1-x}Ca_{1+x}MnO_4$ (x=0.45, 0.35). Temperature dependence measurements of the magnetic intensities with different energy resolutions indicate a glassy nature of the magnetic moments. Inelastic neutron scattering on the x=0.45 system reveal both symmetric and asymmetric magnetic excitations about the CM peak positions: one dispersive spin wave that imitates the x=0.5 system; and another localized mode at about 1 meV. This strongly suggests two types of spin dynamics originated from separated phases: the CE-type magnetic phase and an additional electronic phase caused by extra electrons introduced into the CE template.

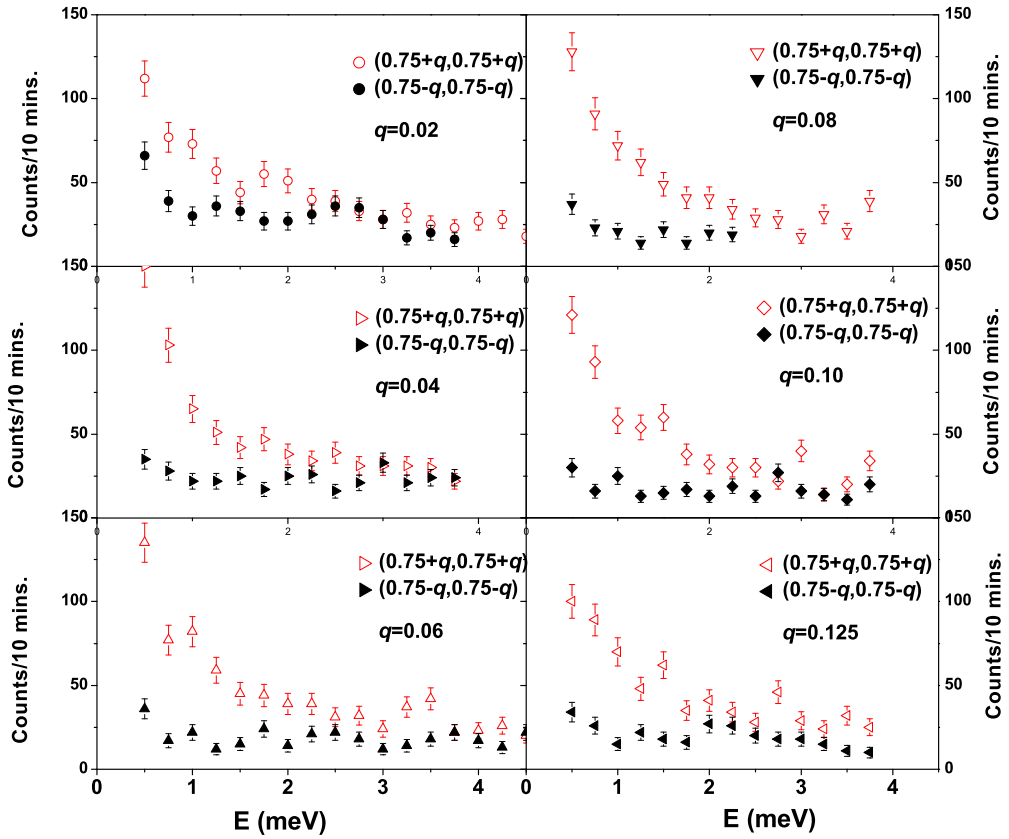

Figure 4.10: Magnetic excitations are measured toward the two boundaries from the zone center. In the direction where the ICM exists (open red symbols), there is a diffuse scattering that is not observed in the opposite direction where there is no ICM magnetic fluctuation (solid black symbols).

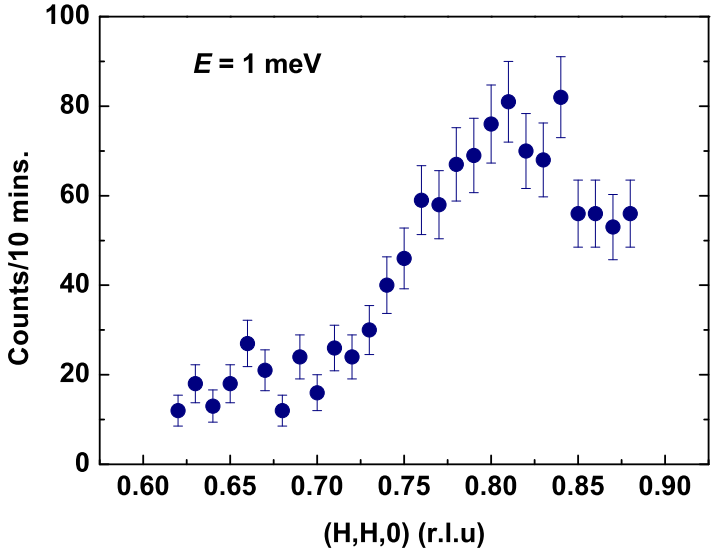

Figure 4.11: Constant-E scans at E=1 meV for PCMO (x=0.35) shows that the diffuse scattering occurs only on the ICM side of the magnetic Brillouin zone.

Chapter 5

Crystalline electric field excitations of Ce^{3+} in $CeFeAsO_{1-x}F_x$

5.1 Introduction and motivation

The rare-earth (R) oxypnictides with general formula RFeAsO (R = La, Sm, Ce, Nd, and Pr) are currently attracting much attention due to the discovery of high-transition temperature (high-T_c) superconductivity in these materials upon chemical doping [27–29,106,107]. Although superconductivity in electron doped LaFeAsO appears at a moderate superconducting temperature of 28 K [106], replacing La with other rare earth ions increases T_c up to 55 K [27–29], making the rare-earth oxypnictides a new class of high-T_c superconductors with critical temperatures only surpassed by high-T_c copper oxides. Since superconductivity in these rare-earth oxypnictides appears after electron-doping to suppress the static antiferromagnetic (AF) order in their parent compounds [108–112], it is important to determine the influence of magnetic interactions on the superconducting properties. Compared to LaFeAsO, where Fe is the only possible ion carrying a significant magnetic moment, the rare-earth oxypnictide with unpaired $4f$ electrons such as Ce^{3+} in CeFeAsO offers an unique opportunity to study the interplay between the rare-earth and Fe magnetic ions. In particular, by using neutron scattering to study the crystal-electric-field (CEF) excitations of the rare-earth in RFeAsO and their doped superconductors, one can determine the electronic ground state of the R ions and therefore understand the low temperature

thermodynamic and magnetic properties of these materials [113, 114]. Furthermore, since the R ions are situated near the superconducting FeAs layer, CEF excitations at the R sites are sensitive to the electronic properties of the FeAs layer, and can be used as a probe to study the influence of superconductivity on spin fluctuations in the FeAs plane [119–121].

In this chapter, I report inelastic neutron scattering studies of the Ce^{3+} CEF excitations in the AF ordered CeFeAsO and superconducting $CeFeAsO_{0.84}F_{0.16}$ ($T_c = 41$ K) [109]. For CeFeAsO, we find that the Ce^{3+} CEF levels are composed of three magnetic doublets at $\hbar\omega = 0, 18.63$, and 67.67 meV in the paramagnetic state. When the Fe long range AF order sets in, these doublets are split into six singlets. In the case of $CeFeAsO_{0.84}F_{0.16}$, although the three doublets are no longer split, the intrinsic linewidth Γ and the peak position of the $\hbar\omega_1 = 18.7$ meV mode show a clear anomaly below T_c. These results suggest that the linewidth and position of the CEF transitions in the rare-earth oxypnictides are sensitive to the Fe spin ordering, and can be used as a direct probe of the spin dynamics in the nearby FeAs planes.

5.2 Experimental details

Our experiments were carried out using the MERLIN chopper spectrometer at ISIS facility, Rutherford-Appleton Laboratory, Didcot, UK [122]; the BT4 Filter Analyzer Neutron Spectrometer (FANS) at the NIST center for neutron research (NCNR) [123]; and the NG4 Disk-chopper time-of-flight spectrometer (DCS) at NCNR, Gaithersburg, Maryland. MERLIN is a high count rate, medium energy resolution, direct geometry chopper spectrometer with a large solid angle of position sensitive detectors. FANS is a high count instrument to measure inelastic excitations on powders and DCS is a cold neutron direct geometry chopper spectrometer. Our CeFeAsO and $CeFeAsO_{0.84}F_{0.16}$ samples were prepared using methods described in Ref. [27] and their structural/magnetic properties are discussed in Ref. [109]. For MERLIN measurements, a low temperature ^{4}He cryostat and closed cycle He-gas refrigerator were used for the temperature variable. The incident beam energies were $E_i = 7, 10, 31, 73, 105, 312$ meV. To separate the CEF magnetic scattering from phonon excitations, we also measured LaFeAsO and $LaFeAsO_{0.92}F_{0.08}$ samples [108] as reference materials for phonon subtraction from the Ce samples. The La samples did

not reveal any clear change in phonon spectra below and above T_C, hence allowed us to use these samples to subtract the phonon in the Ce-samples. The data for $CeFeAsO_{1-x}F_x$ and $LaFeAsO_{1-x}F_x$ were converted to absolute units of mb/sr/meV/f.u. by normalizing the scattering from vanadium measurements made with the same incident energies. For the DCS measurements, we used a ^{4}He cryostat and an incident beam energy of 3.55 meV and for the FANS measurements we used a top-loading He-gas refrigerator.

5.3 Structure and CEF of Ce^{3+} in $CeFeAsO_{1-x}F_x$

Figure 5.1(a) shows the position of the Ce ion in the crystal structure environment of CeFeAsO. Relative to the Fe sublattice, the Ce^{3+} ions are located alternately above and below the (AF ordered) Fe layers as shown in Fig. 5.1(b). Figures 5.1(c) and 5.1(d) summarize the Ce CEF excitation energies determined from our inelastic neutron scattering experiments for CeFeAsO and $CeFeAsO_{0.84}F_{0.16}$, respectively. According to neutron powder diffraction experiments [109], both CeFeAsO and $CeFeAsO_{0.84}F_{0.16}$ have a tetragonal (space group $P4/nmm$) crystal structure at room temperature. However, on cooling, CeFeAsO first exhibits a structural phase transition, changing the crystal symmetry from tetragonal to orthorhombic (space group $Cmma$), and then orders antiferromagnetically with a spin structure as shown in Figs. 1a and 1b [108, 109]; $CeFeAsO_{0.84}F_{0.16}$ maintains the tetragonal structure for all temperatures and does not order magnetically above 4 K. In the tetragonal structure, the Ce atoms are located at the $2c$ crystallographic site which has C_{4v} point symmetry. This gives three non-zero CEF parameters in the crystal field Hamiltonian and its form in Stevens operators formalism is

$$H_{CEF}(C_{4v}) = B_2^0 O_2^0 + B_4^0 O_4^0 + B_4^4 O_4^4 \tag{5.1}$$

. In the case of the low-temperature orthorhombic structure of CeFeAsO, the Ce atoms are at the $4g$ $(0, 1/4, z)$ site which gives local point symmetry of $mm2$ (C_{2v}). The resulting Hamiltonian then involves five non-zero crystal field parameters as

$$H_{CEF}(C_{2v}) = B_2^0 O_2^0 + B_2^2 O_2^2 + B_4^0 O_4^0 + B_4^2 O_4^2 + B_4^4 O_4^4 \tag{5.2}$$

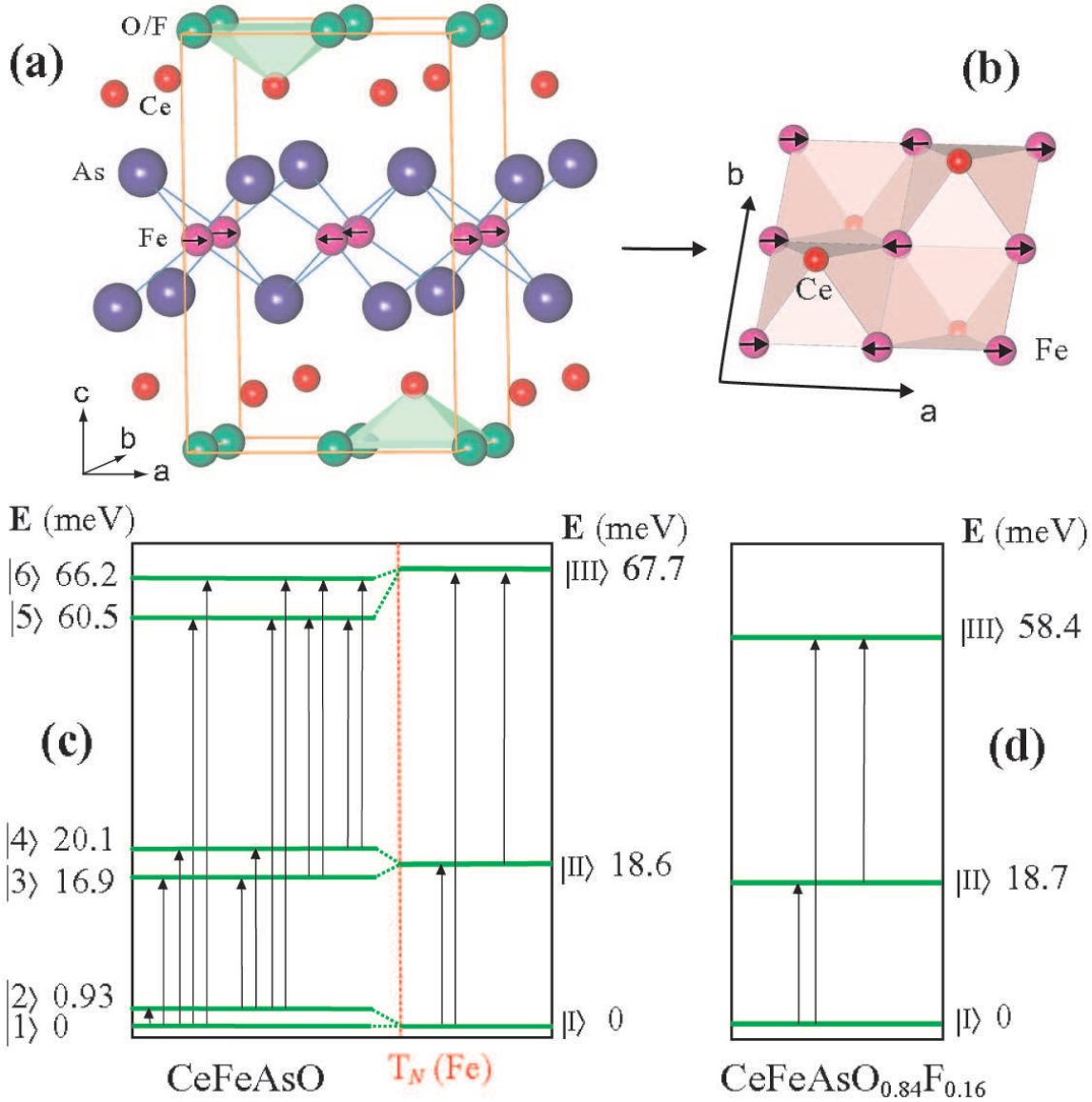

Figure 5.1: Summary of the CeFeAsO crystal/magnetic structure and CEF levels determined from our inelastic neutron scattering experiments. (a) The Fe spin ordering in the CeFeAsO chemical unit cell. (b) The Fe spins in CeFeAsO with respect to the Ce positions. The Fe moments lie in the a-b plane along the a-axis and form an antiferromagnetic collinear spin structure. (c) Ce^{3+} CEF levels in CeFeAsO for temperatures above and below the Fe AF Néel temperature of $T_N = 140$ K [109]. The arrows indicate possible transitions. (d) Ce^{3+} CEF levels in superconducting $CeFeAsO_{0.84}F_{0.16}$ at low temperature.

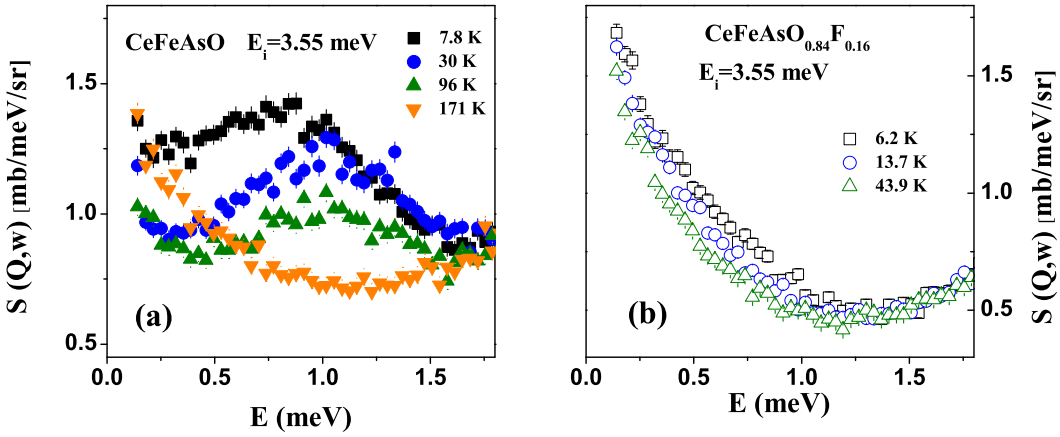

Figure 5.2: Temperature dependence of the CEF excitations in CeFeAsO and $CeFeAsO_{0.84}F_{0.16}$ integrated over $0 < Q < 4$ Å^{-1} and our model determination of the CEF levels. (a) The raw DCS data integrated over $0 < Q < 2.2$ Å^{-1} in arbitrary units as a function of temperature without the LaFeAsO phonon subtraction. (b) The 0.7 meV excitation seen in CeFeAsO is missing in $CeFeAsO_{0.84}F_{0.16}$. Error bars represent one standard deviation.

, where B_n^m's are the CEF parameters to be determined from the experimental data; and O_n^m's are operator equivalents obtained using the angular momentum operators [113].

5.4 CEF levels in superconducting $CeFeAsO_{0.84}F_{0.16}$

We collected neutron scattering data on CeFeAsO and $CeFeAsO_{0.84}F_{0.16}$ on MERLIN and DCS spectrometers with different incident beam energies to search for Ce^{3+} CEF excitations. To eliminate phonon scattering, we carried out identical scans using LaFeAsO and $LaFeAsO_{0.92}F_{0.08}$ as reference materials. We have checked two methods of phonon sub-

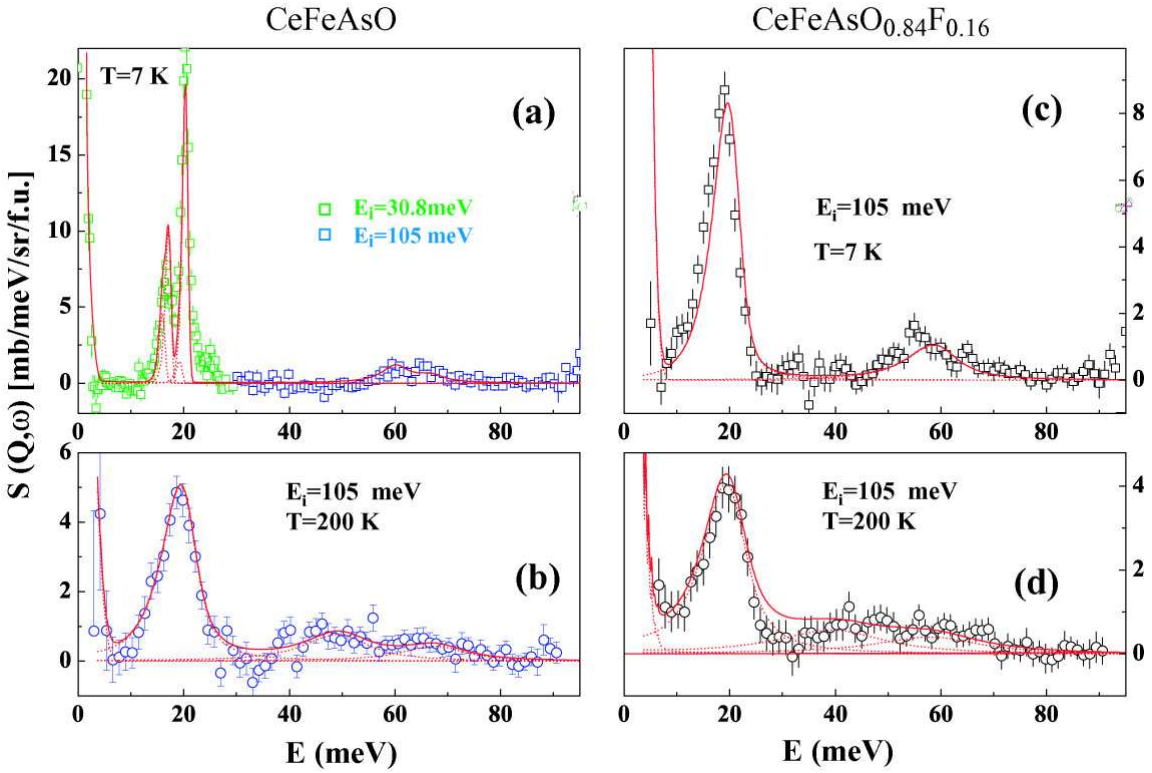

Figure 5.3: Temperature dependence of the CEF excitations in CeFeAsO and $CeFeAsO_{0.84}F_{0.16}$ integrated over $0 < Q < 4$ Å^{-1} and our model determination of the CEF levels. (a) Ce CEF magnetic excitations in absolute units after subtracting the LaFeAsO phonons. The green square denotes the data with E_i=30.8 meV to show the splitting. The solid line is our model fit with parameters listed in Table I. (b) Ce CEF excitations at 200 K; solid line is our model calculation. (c-d) CEF excitations and their temperature dependence for $CeFeAsO_{0.84}F_{0.16}$. The solid lines are model calculations.

Table 5.1: Refined B_n^m CEF parameters for CeFeAsO and $CeFeAsO_{0.84}F_{0.16}$.

	$CeFeAsO_{0.84}F_{0.16}$	CeFeAsO ($> T_N$)	CeFeAsO ($< T_N$)
B_2^0	2.545 ± 0.089	3.155 ± 0.120	3.012 ± 0.102
B_4^0	-0.045 ± 0.005	-0.029 ± 0.007	0.031 ± 0.002
B_2^2			1.972 ± 0.365
B_4^2			-0.061 ± 0.045
B_4^4	0.641 ± 0.026	0.710 ± 0.044	0.440 ± 0.041

tractions : (1) scaling the La data by the total cross-section and then subtracting off from the Ce, i.e.: $S(q,\omega)_{magnetic}$=S(q, $\omega)_{Ce}$- S(q, $\omega)_{La}\times\sigma_{CeFeAsOF}/\sigma_{LaFeAsO}$, and (2) scaling method: where high-Q data of the Ce-where scaled down to low-Q and then subtracted off: $S(q,\omega)_{magnetic}$= $S(q,\omega)_{Ce-low-Q}$- $S(q,\omega)_{Ce-high-Q}/(S_{La-high-Q}/S_{La-low-Q})$. Both methods gave very similar results for 30meV data, but Method (2) gave better subtraction of 35meV phonon peak, so we used this method (2) in Fig2. Method (1) is justified by the fact that the LaFeAsO and CeFeAsO have the same crystal structure, and thus the same phonon contribution to the INS cross section is expected, after taking into account the difference in the coherent cross section of La and Ce. Method (1) is used to get the accurate linewidths at different temperatures as in figs. 4 and 6.

Figures 3(a) and (b) show the phonon subtracted energy scans for CeFeAsO at 7 K and 200 K on MERLIN obtained with E_i = 30.8 meV and E_i = 105 meV. Fig. 5.2(a) plots similar data taken on DCS with E_i = 3.55 meV. Identical scans taken for $CeFeAsO_{0.84}F_{0.16}$ are shown in Figs. 3(c) and (d). We first discuss results on the superconducting sample as there are no complications of structural distortion and Fe magnetic order. To obtain the B_n^m's CEF parameters in the $H_{CEF}(C_{4v})$ Hamiltonian, we first used the FOCUS program, which has a Monte Carlo search routine, to fit the observed two CEF excitations at 18.7 meV and 58.4 meV in Figs. 2(c). We then fit many spectra simultaneously with different incident energies and temperatures using a CEF fit program and the results are plotted as solid lines in Figs. 2(c) and (d) for 7 K and 200 K, respectively. Tables I and II summarize the B_n^m's CEF parameters and wave functions for $CeFeAsO_{0.84}F_{0.16}$ obtained from those fits.

5.5 CEF levels in the antiferromagnetically ordered CeFeAsO

Comparing to the superconducting $CeFeAsO_{0.84}F_{0.16}$, the Ce CEF excitations in CeFeAsO near 19 and 65 meV have clear double peaks at low temperature that become a single peak at 200 K [Figs. 2(a) and (b)]. In addition, the low-energy spectra in the inset of Fig. 5.2(a) shows a clear peak around 0.9 meV that is not present at 171 K. To understand this phenomenon, we carried out careful temperature dependence measurements of the ∼19 meV CEF excitation. Figure 5.3(a) shows the raw $S(Q,\omega)$ spectra of CeFeAsO collected

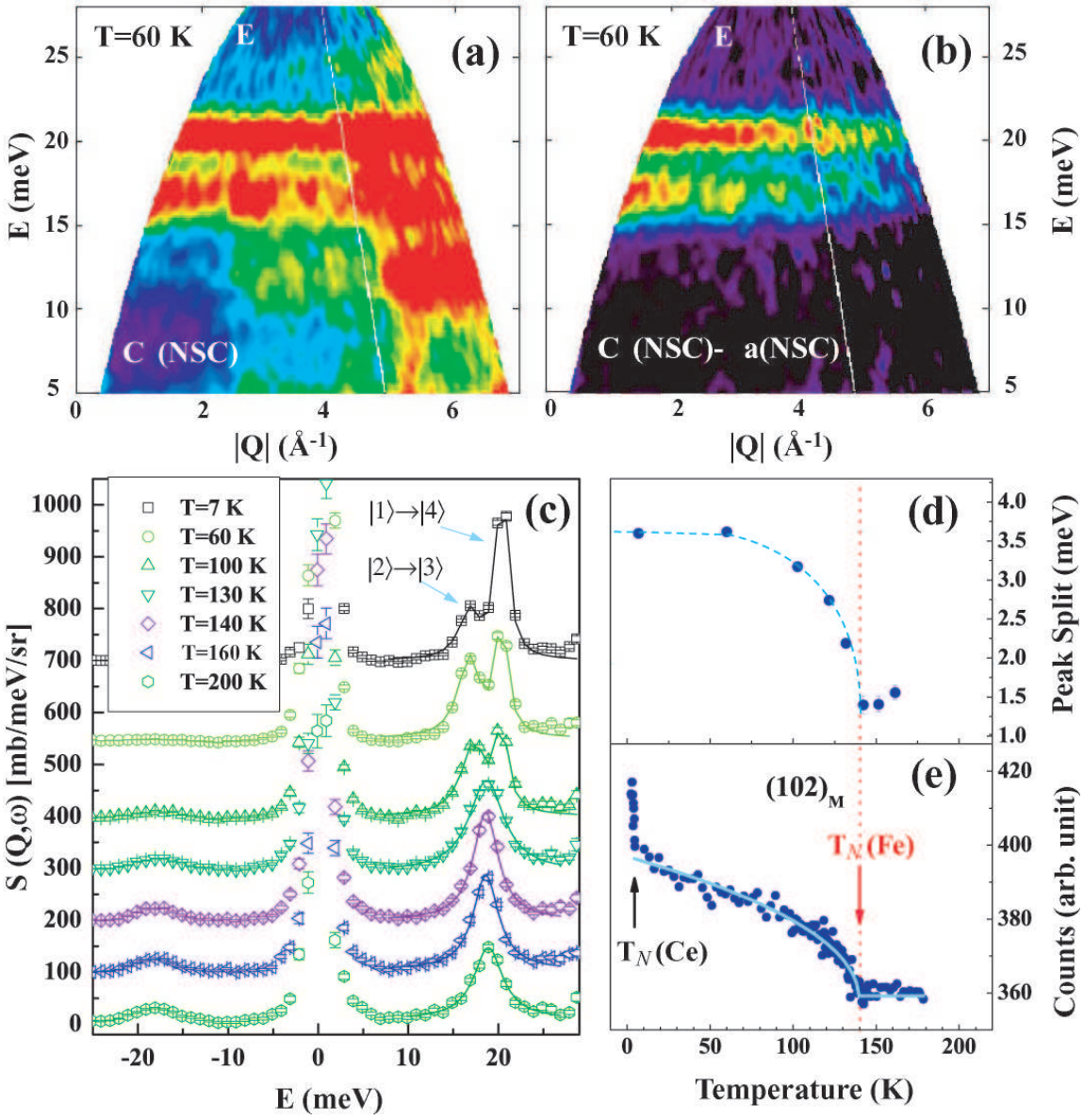

Figure 5.4: (a) Raw $S(Q,\omega)$ spectra of CeFeAsO at 60 K and $E_i = 30$ meV on MERLIN. (b) Ce CEF excitations after subtraction of the LaFeAsO background. (c) Temperature dependence of the 18.7 meV excitations. The peaks around 18 meV at 7 K are fitted with 2 lorentzians, the widths of which were fixed for fittings at all higher temperatures. Although this ignores the broadening of linewidths upon warming and gives illusionary finite peak separation above T_N, the net splitting solely caused by molecular field can be monitored by abrupt change of this separation which happens below 140 K, the T_N of Fe as shown in (e).

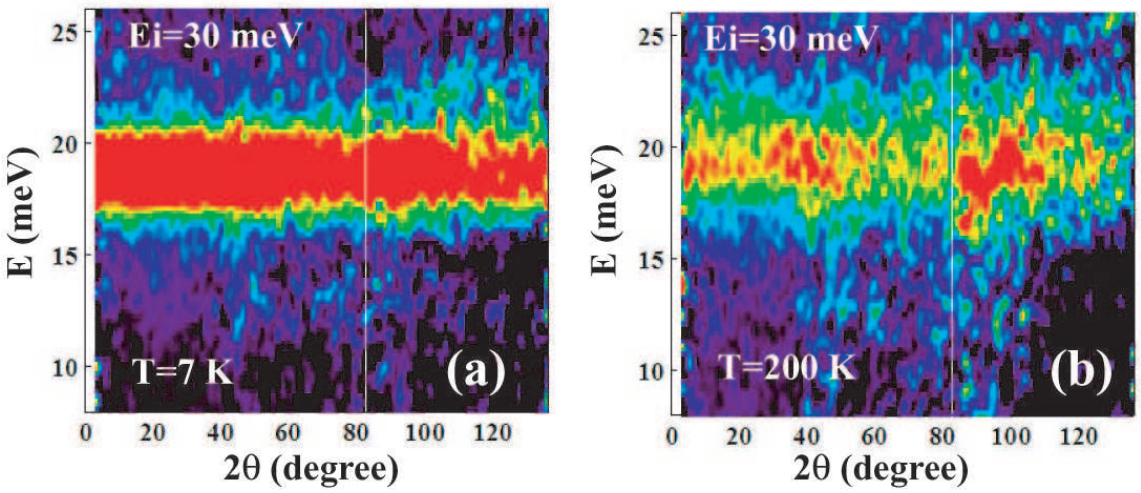

Figure 5.5: The $S(Q,\omega)$ spectra of $CeFeAsO_{0.84}F_{0.16}$ with E_i=30.8 meV after phonon subtraction at (a) 7 K and (b) 200K.

on MERLIN at 60 K using $E_i = 30.8$ meV. After subtracting the phonon scattering background collected using LaFeAsO, the Ce CEF level shows two clear bands of excitations at 16.9 and 20.1 meV [Fig. 5.3(b)]. Figure 5.3(c) shows the detailed temperature dependence of the ∼19 meV excitations and Figure 5.3(d) plots splitting of the two low temperature peaks. Comparison of these figures with the Néel ordering temperature of CeFeAsO in Figure 5.3(e) makes it immediately clear that the CEF splitting is due to the long range AF Fe ordering [109].

In principle, the orthorhombic structural distortion that precedes the AF ordering in CeFeAsO can have an effect on the Ce CEF levels. However, neutron powder diffraction data [109] showed that the Ce local environment is not much affected by the lattice distortion. The first principle calculation [118] shows that the crystal distortion is too small to give any new set of Bkm parameters. It changes them only 0.2 percent. Even if there is a remarkable change of local symmetries, the new set of Bkm numbers for T$< T_N$ cannot split the Kramer degenerate states by themselves. Hence a molecular field is needed for a Zeeman term to split the doublets. Usually, the Zeeman term is a small perturbation. The splitting of the ground state at $\sim$ 0.9 meV puts a very rigid constraint on the field that one can have. We started fitting the low temperature spectra using the CEF parameters for tetragonal geometry, then added the effect of the molecular field of the Fe spins in the pres-

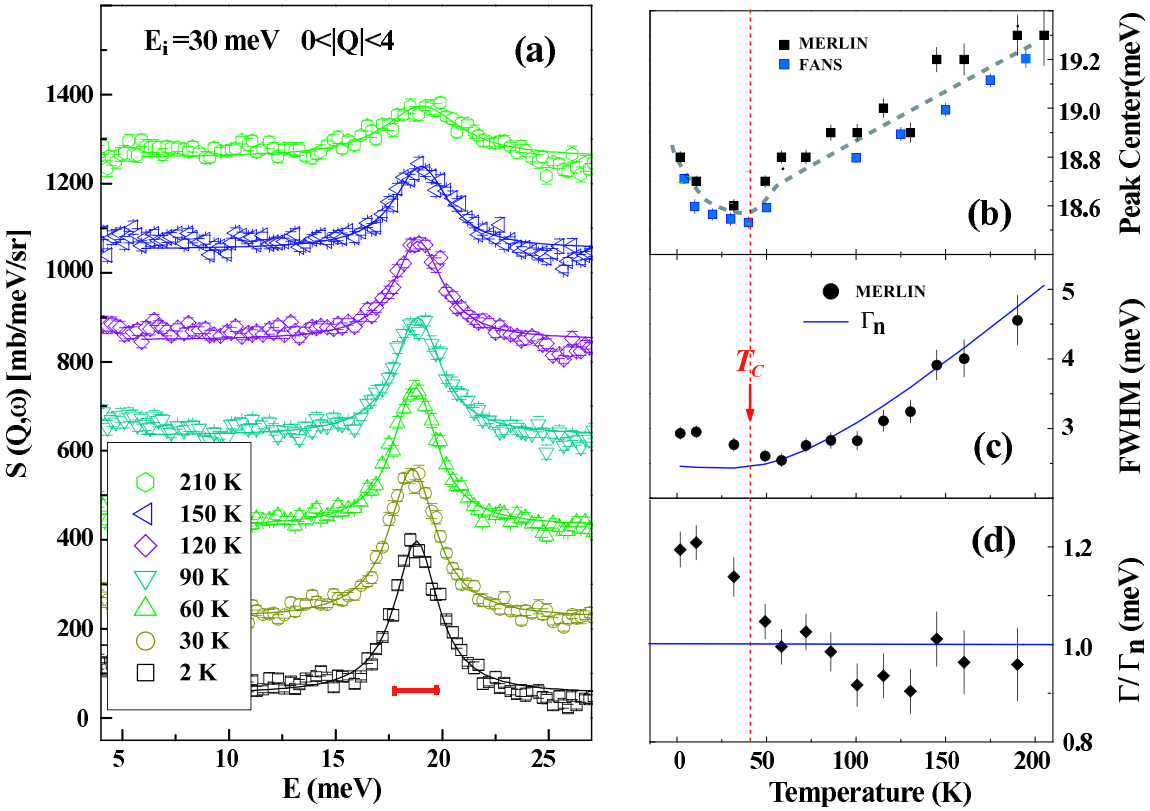

Figure 5.6: Temperature dependence of the $\hbar\omega_1 = 18.7$ meV Ce CEF excitation for $CeFeAsO_{0.84}F_{0.16}$. (a) MERLIN measurements using $E_i = 30.8$ meV at different temperatures. The instrumental energy resolution is 2.1 meV at elastic position (horizontal bar). (b) The peak position as a function of temperature for the 18.7 meV CEF level. The solid squares are MERLIN data while blue squares are FANS data, both show clear anomaly at T_c. (c) The intrinsic linewidth $\Gamma(T)$ as a function of temperature. The solid line shows the expected $\Gamma_n(T)$ assuming noninteracting Fermi liquid. $\Gamma(T)$ deviates from $\Gamma_n(T)$ near T_c. (d) $\Gamma(T)/\Gamma_n(T)$ shows a clear anomaly near T_c, consistent with (c).

ence of the orthorhombic structural distortion. The solid line in Fig. 5.3(a) shows our fit to the data, and the CEF parameters for temperatures above and below T_N are also given in Table I. Although the splittings of the doublets and their transition intensities can be reproduced using orthorhombic point symmetry with molecular field H_x=H_z=1.129±0.13 meV, the thus obtained CEF parameters for T< T_N given in table are not of a unique set. Since Ce ions reside at the center of Fe-squares, a resultant molecular field on the Ce site is not expected unless Fe ions have additional anisotropic interaction such as Fe-Ce exchange interaction.

Since we already know the direction of the Ce moment, which is in the $a-b$ plane and along the a-direction, we can fix the sign of B_2^0 as positive because the magneto crystalline anisotropy energy is given by

$$E_a = K_1 sin2\theta \tag{5.3}$$

where

$$K_1 = -\frac{3}{2}[\alpha A_2^0 < R_2 >] < 3J_z - J(J+1) > \tag{5.4}$$

and

$$B_2^0 = \alpha J A_2^0 < r_2 > . \tag{5.5}$$

For Ce^{3+}, αJ = -5.71 $\times 10^{-2}$. When sign of A_2^0 is known one can easily predict the easy magnetization direction of the RE moment. Moment is parallel to c when αJ and A_2^0 have different sign, i.e. negative B_2^0, and the moment is parallel to the ab-plane when αJ and A_2^0 have the same sign, namely positive B_2^0.

Assuming that the $|\mathrm{I}\rangle$, $|\mathrm{II}\rangle$, and $|\mathrm{III}\rangle$ doublets in the paramagnetic state of CeFeAsO split into $|1\rangle$ to $|6\rangle$ singlets in the AF state as shown in Fig. 5.1(c), the observed excitations near 19 meV should be composed of 4 possible transitions $|1\rangle \rightarrow |3\rangle$, $|1\rangle \rightarrow |4\rangle$, $|2\rangle \rightarrow |3\rangle$, and $|2\rangle \rightarrow |4\rangle$. Since the transition probabilities $|\langle 1| J_z |3\rangle|^2$ and $|\langle 2| J_z |4\rangle|^2$ are rather small, the observed excitations at 16.8 and 20.4 meV in Fig. 5.2(a) actually arise from $|1\rangle \rightarrow |4\rangle$ and $|2\rangle \rightarrow |3\rangle$, and are controlled by the thermal population of $|1\rangle$ and $|2\rangle$, respectively. This is consistent with the temperature dependence of these two excitations, where the

Table 5.2: Wave functions of different CEF levels for $CeFeAsO_{0.84}F_{0.16}$ and CeFeAsO above T_N.

	$CeFeAsO_{0.84}F_{0.16}$	CeFeAsO ($> T_N$)
$\|\mathrm{I}\rangle$	$\|\mp 1/2\rangle$	$\|\mp 1/2\rangle$
$\|\mathrm{II}\rangle$	$-0.5\left\|\mp\frac{5}{2}\right\rangle + 0.866\left\|\pm\frac{3}{2}\right\rangle$	$-0.43\left\|\mp\frac{5}{2}\right\rangle + 0.902\left\|\pm\frac{3}{2}\right\rangle$
$\|\mathrm{III}\rangle$	$0.866\left\|\mp\frac{5}{2}\right\rangle + 0.5\left\|\pm\frac{3}{2}\right\rangle$	$0.902\left\|\mp\frac{5}{2}\right\rangle + 0.43\left\|\pm\frac{3}{2}\right\rangle$

16.8 mode decreases and the 20.1 meV excitation increases with decreasing temperature [Fig. 5.3(c)].

5.6 Linewidth change and superconductivity

In rare-earth substituted high-T_c copper oxides such as $Tm_{0.1}Y_{0.9}Ba_2Cu_3O_{6+x}$ [119] and $Ho_{0.1}Y_{0.9}Ba_2Cu_3O_7$ [120], the intrinsic linewidth Γ and peak position of the rare-earth CEF excitations are used to probe the local magnetic response of the CuO_2 planes and the formation of a superconducting energy gap. The CEF excitations of Ho and Er have also been used to study pseudogap and order-parameter symmetry in the underdoped superconducting $HoBa_2Cu_4O_8$ and $Er_2Ba_4Cu_7O_{14.92}$, respectively [121]. To see if the $\hbar\omega_1 = 18.7$ meV CEF excitation in $CeFeAsO_{0.84}F_{0.16}$ is also sensitive to the occurrence of superconductivity, we carefully probed the temperature dependence of its intrinsic linewidth Γ [Figs. 4(a), 4(c)] and peak positions [Fig. 5.4(b)]. Figure 5.4(a) shows the phonon subtracted data at different temperatures obtained on MERLIN with $E_i = 30.8$ meV. Figure 5.4(b) plots the peak position as a function of temperature, which shows a clear anomaly around T_c. Inspection of Fig. 5.4(c) reveals that the linewidth decreases with decreasing temperature. For the case when the CEF levels do not overlap, the temperature dependence of the linewidth $\Gamma(T)$ of the transition between the ground state ($|1\rangle$) and the first excited state ($|2\rangle$) in Fig. 5.1(c) can be accurately estimated using Eq.(1) in [120]:

$$\Gamma = 2J_{ex}^2[M_{01}^2 coth(\beta\hbar\omega_1/2)\chi''(\omega_1) + \sum_{t>1}(M_{0t}^2\frac{\chi''(\omega_t)}{e^{\beta\hbar\omega_t}-1} + M_{1t}^2\frac{\chi''(\omega_t-\omega_1)}{e^{\beta\hbar(\omega_t-\omega_1)}-1})] \qquad (5.6)$$

where $\hbar\omega_t$ is the energy of level t relative to the ground state, M_{ij}^2 is the squared matrix element of the angular momentum operator, J_{ex} is the exchange constant between the localized $4f$ moment and the quasiparticles, $\beta = 1/k_BT$. $\chi''(\omega)$ is the same local susceptibility as used in nuclear relaxation, namely, the Brillouin zone sum of $|A(q)|^2 \chi''(\mathbf{q},\omega)$, where $\chi''(\mathbf{q},\omega)$ is the dynamic susceptibility probed by neutron scattering and $A(\mathbf{q})$ is a geometrical factor which takes account of the local structure around the RE ion. To first order, this can be written as $\Gamma(T) \propto \chi''(\hbar\omega_1)\coth(\frac{\hbar\omega_1}{2k_BT})$. To understand $\Gamma(T)$, we calculate the linewidth $\Gamma_n(T)$ below 150 K using this equation assuming a noninteracting Fermi liquid normal state [120], even though this is still under discussion. The solid line in Fig. 5.4(c) shows the outcome of our calculation. The observed linewidth starts to deviate from the expected values near T_c, as shown more clearly in $\Gamma(T)/\Gamma_n(T)$ [Figure 5.4(d)]. The most natural interpretation of Figs. 4(c) and (d) is that the local integrated magnetic susceptibility $\chi''(\hbar\omega_1)$ from the Fe spin fluctuations at 18.7 meV increases dramatically below T_c. Since the temperature dependence of this excitation and its energy are rather similar to that of the neutron spin resonance recently observed in $Ba_{0.6}K_{0.4}Fe_2As_2$ [124], we speculate that the observed linewidth change might be related to the spin resonance in $CeFeAsO_{0.84}F_{0.16}$.

5.7 Conclusions

We use inelastic neutron scattering to study the crystalline electric field (CEF) excitations of Ce^{3+} in $CeFeAsO_{1-x}F_x (x = 0, 0.16)$. For nonsuperconducting CeFeAsO, the Ce CEF levels have three magnetic doublets in the paramagnetic state, but these doublets split into six singlets when Fe ions order antiferromagnetically. For superconducting $CeFeAsO_{0.84}F_{0.16}$ ($T_c = 41$ K), where the static AF order is suppressed, the Ce CEF levels have three magnetic doublets at $\hbar\omega = 0, 18.7, 58.4$ meV at all temperatures. Careful measurements of the intrinsic linewidth Γ and the peak position of the 18.7 meV mode reveal clear anomaly at T_c, consistent with a strong enhancement of local magnetic susceptibility $\chi''(\hbar\omega)$ below T_c. These results suggest that CEF excitations in the rare-earth oxypnictides can be used as a probe of spin dynamics in the nearby FeAs planes.

Chapter 6

Crystal field levels in the filled skutterudite $PrOs_4As_{12}$

In this chapter, neutron study on the Pr^{3+} crystalline electric field (CEF) excitations in the filled skutterudite $PrOs_4As_{12}$ is presented. By comparing the observed levels and their strengths under neutron excitation with the theoretical spectrum and neutron excitation intensities, the Pr^{3+} CEF levels are identified and the ground state is determined to be a magnetic $\Gamma_4^{(2)}$ triplet. The excited states Γ_1, $\Gamma_4^{(1)}$ and Γ_{23} are at 0.4, 13 and 23 meV, respectively. A comparison of the observed CEF levels in $PrOs_4As_{12}$ with the heavy fermion superconductor $PrOs_4Sb_{12}$ reveals the microscopic origin of the differences in the ground states of these two filled skutterudites.

6.1 Introduction and Motivation

The Pr-based filled skutterudites (FS) have the formula PrT_4X_{12}, where T is one of the transition metals Fe, Ru, or Os, and X is a pnictogen (P, As, or Sb) [125–127]. The notably mounting interests and efforts in the study of the FS compounds are motivated by the remarkable diversity of their electronic and magnetic ground states, including multipole ordering [19, 128], small gap insulators [129, 130], conventional superconductivity [15, 131], unconventional superconductivity [132, 133] and magnetic ordering [134–138]. Despite the large differences in their physical properties, these compounds are governed by only a few

parameters, including the interaction between the conduction and the $4f$ shell electrons (the c-f coupling) and the effect of the crystalline electric field (CEF) potential on the Pr^{3+} $4f$ electrons [**?**,19,128–130,132–138]. For example, transport and bulk magnetic measurements on the heavy Fermion superconductor $PrOs_4Sb_{12}$ suggested either a Γ_1 singlet ground state or a Γ_3 nonmagnetic doublet ground state [132, 133]. Inelastic neutron scattering experiments on $PrOs_4Sb_{12}$ showed that the Pr^{3+} CEF levels include a Γ_1 singlet ground state and a low-lying $\Gamma_4^{(2)}$ magnetic triplet excited state at 0.6 meV [21–23]. This rules out the quadrupolar Kondo effect, which arises only from a nonmagnetic doublet ground state [139], as the microscopic origin for the observed heavy-fermion superconductivity.

The FS compounds belong to the space group $Im\bar{3}$ [127]. The rare earth atoms are located at the corners and body-center of the cubic lattice, each of which is surrounded by a simple cube of 8 transition metal atoms at the 8c sites [Fig. 6.1(a)] and by an icosahedron of 12 pnictogen atoms at the 24g Wyckoff sites [Fig. 6.1(c)]. Owing to their unique structure, a subtle modification on composition can result in a different CEF scheme and thus a completely different ground state. However, a general understanding is desirable as to how the compositions influence the CEF levels. In $PrOs_4As_{12}$, in which the pnictogen Sb in $PrOs_4Sb_{12}$ is replaced by As, the material displays quite different correlated electron properties [136,137]. The temperature dependence of the electrical resistivity reveals Kondo lattice behavior, which is not observed in $PrOs_4Sb_{12}$ [24]. Specific heat measurements indicate an enhanced electronic specific heat coefficient of $\gamma \approx 1$ J/mol K^2 for $T \leq 1.6$ K and $0 \leq H \leq 1.25$ T [136]. The compound exhibits several ordered phases at temperatures below 2.3 K and fields below about 3 T [140]. The ground state has been determined to be antiferromagnetic (AF) by neutron scattering experiments [137]. A determination of the Pr^{3+} CEF level scheme in $PrOs_4As_{12}$ and its microscopic origin is crucial for understanding why its ground state is different from that in $PrOs_4Sb_{12}$. The outcome will lead to a more general understanding of how the structures and compositions in Pr-based FSs can influence their CEF levels and ground states.

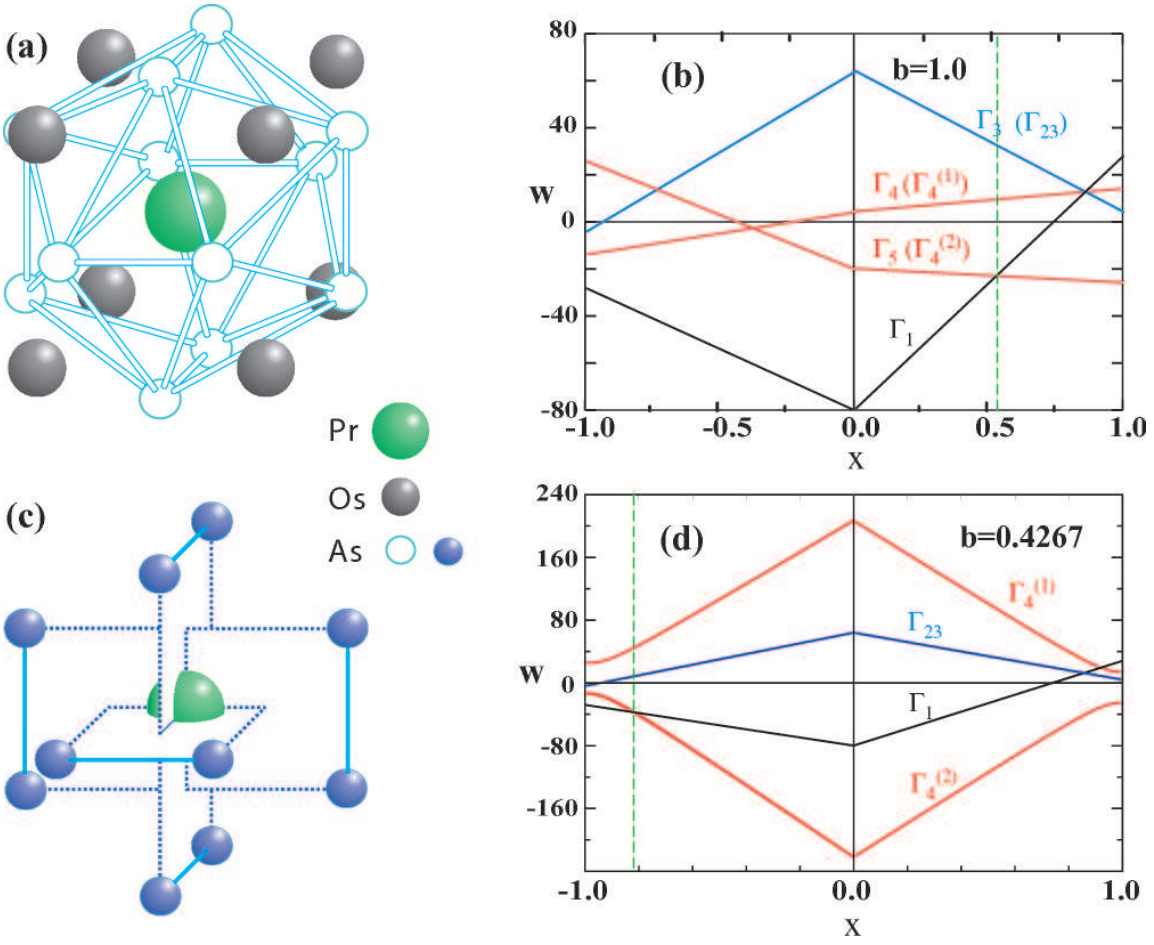

Figure 6.1: (a) The cube of 8 Os ions surrounding the central Pr^{3+} ion in $PrOs_4As_{12}$. These give an O_h-symmetric CEF. (b) The corresponding spectrum of O_h-symmetry Pr^{3+} CEF levels. (black=singlet, blue=doublet, red=triplet). The relative coupling x that gives singlet-triplet degeneracy is shown by a dashed vertical. (c) The 12 nearest-neighbor As ions surrounding the central Pr^{3+} in $PrOs_4As_{12}$, giving a reduced symmetry (T_h) CEF. (d) The corresponding As-only T_h-symmetry Pr^{3+} CEF spectrum in $PrOs_4As_{12}$.

6.2 Experimental details

Single crystals of $PrOs_4As_{12}$ were grown with elements of purity higher than 99.9 percent at high temperatures and pressures. After the majority of the flux has been removed with distillation, tiny single crystals with dimension of ∼0.5 mm were collected and cleaned to further remove Pr impurities from the surface. Powder sample was prepared by grinding the single crystals for powder diffraction measurement and CEF measurement. Our neutron scattering experiments were carried out on the cold neutron triple-axis spectrometer SPINS at the NIST Center for Neutron Research (NCNR) and on the HET chopper spectrometer at ISIS (Rutherford Appleton Laboratory), as described previously [141]. We reference positions in reciprocal space at wave vector $\mathbf{Q} = (q_x, q_y, q_z)$ in Å^{-1} using (H, K, L) reciprocal lattice units (r.l.u.) notation, where $(H, K, L) = (q_x a/2\pi, q_y a/2\pi, q_z a/2\pi)$ for the cubic $PrOs_4As_{12}$ unit cell ($a = 8.5319$ Å) [136]. We used a ^{3}He-^{4}He dilution refrigerator for the field-dependent experiments. The nature of observed CEF excitations were confirmed in a large temperature (0.08 K-200 K) and magnetic field (0 T-11 T) range.

6.3 Results of CEF measurements

Figure 6.2 summarizes the neutron scattering intensity from $PrOs_4As_{12}$ on HET at temperatures between 1.5 K and 200 K. Since the CEF magnetic scattering decreases with increasing Q whereas the intensity of phonons increases with Q, a comparison of the neutron intensities in the low- and high-angle detectors can distinguish between magnetic and phonon scattering. Figure 6.2(a) shows the scattering function at $T = 1.5$ K and $T = 200$ K with an incident neutron beam energy of $E_i = 32$ meV. Comparison of the low- and high-angle data reveals two clear CEF excitations at 13 meV and 23 meV, with phonons at $\sim$ 20 meV. Measurements with $E_i = 12$ and 50 meV showed no evidence of additional CEF excitations at energy transfers between 2 and 8 meV or above 25 meV [Figs. 2(b) and 2(c)].

To search for CEF excitations at energies below 2 meV, we carried out high resolution measurements using SPINS. At $T = 0.32$ K, energy scans at $Q = (1.2, 0, 0)$ showed a clear peak at 0.4 meV; this mode decreases and becomes broader on warming to 2.5 K and

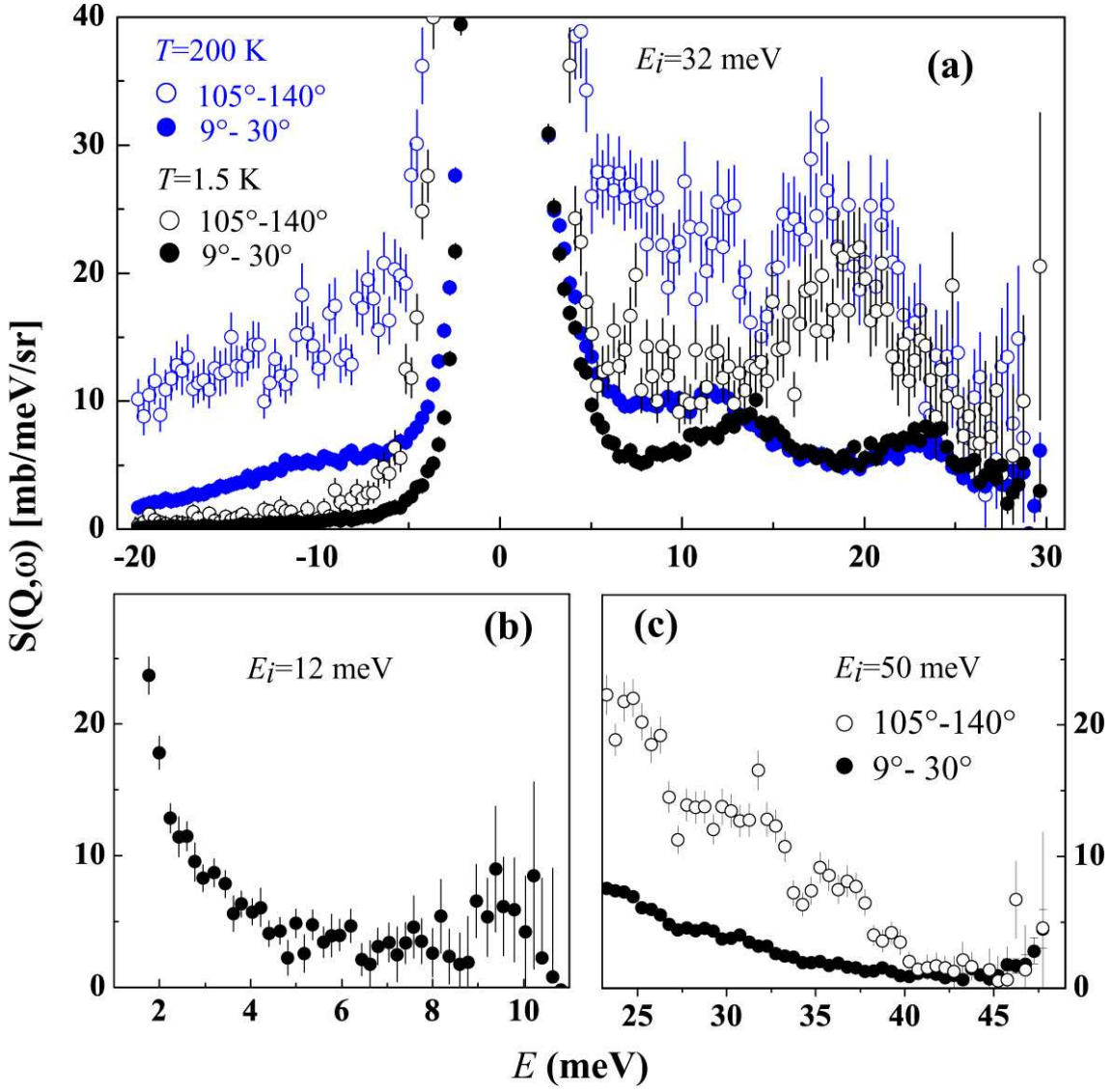

Figure 6.2: (a) Neutron inelastic scattering at $T = 1.5$ K and $T = 200$ K with $E_i = 32$ meV, integrated over scattering angles from 9° to 30° (low-angle detectors) and from 105° to 140° (high-angle detectors). (b) The same at $E_i = 12$ meV; (c) $E_i = 50$ meV. The scattering function $S(Q, \omega)$ was normalized by comparison to a vanadium standard.

6 K [Fig. 6.3(a)]. Figure 6.3(b) shows that the energy of the ∼0.4 meV mode has weak Q-dependence and decreases in intensity with increasing Q, thus confirming its magnetic nature. Figure 6.3(d) reveals that the elastic intensity also decreases on warming from 0.08 K to 4 K. This reduction of intensity in the elastic channel with increasing temperature is also observed in the HET data, evidencing the ground state is a magnetic multiplet.

Figures 6.4(a)-(d) show the temperature dependence of the low-angle scattering for $E_i = 32$ meV. The CEF peak intensities do not change significantly with temperature between 1.5 K and 5 K. At 50 K the intensity in the elastic channel has undergone a substantial decrease, and the 13 meV peak has shifted to 10 meV. On further increasing the temperature to 100 K and 200 K the intensities at 0 meV, 13 meV and 23 meV continue to decrease, whereas the scattering at 10 meV increases.

The theoretical description of the Pr^{3+} CEF levels in $PrOs_4As_{12}$ is complicated by the presence of important contributions from two sets of neighboring ions, Os and As. The Pr^{3+} ion in Pr-based FS has a $4f^2$ configuration, which in Russell-Saunders coupling has a ninefold degenerate $^3H_4$ ground state. This degeneracy is lifted by the CEF interaction, which we assume to be dominated by the 12 nearest neighbor pnictogens (As) and the 8 next nearest neighbor Os ions; the distances to these ions are $d_{Pr-As} = 3.23$ Å and $d_{Pr-Os} = 3.69$ Å respectively.

6.4 Single-charge model with separate ions

Os ions form a simple cube around the Pr ions and they alone give an O_h symmetric CEF. The arrangement of the 12 pnictogens (As) around Pr^{3+} forms 3 orthogonally intersected planes where the As-As bonds are shown as solid lines with length L and W is the length of the dashed lines in Fig. 6.1(c) ($b = W/L = 0.4267 \neq 1$). When the 4 pnictogen atoms in each of the 3 orthogonally intersected planes form a square, *i.e.,* $b = W/L = 1$, the fourfold rotational symmetry is recovered and the point group symmetry becomes O_h with the simple cubic CEF potentials [Fig. 6.1(c)] [144]. This O_h case is treated by Lea, Leask, and Wolf (LLW) [144] (see their Fig. 9); we have rederived their excitation spectrum as shown in Fig. 6.1(b).

Both O_h and T_h CEF interactions split the Pr^{3+} $^3H_4$ ground state into a singlet,

a doublet and two triplets [143]. In the $b \neq 1$ T_h-symmetry case, these multiplets are referred to as Γ_1 (a singlet), Γ_{23} (a nonmagnetic doublet), and $\Gamma_4^{(1)}$ and $\Gamma_4^{(2)}$ (magnetic triplets). These two triplets are linear combinations of the O_h-symmetry triplets, mixed by the new T_h CEF interaction [143]; this mixing modifies the excitation spectrum and leads to b-dependent neutron transition intensities.

The T_h-symmetry CEF excitation spectrum has not been considered in detail in the literature, and the corresponding neutron transition intensities between T_h CEF levels have not been considered at all. To aid in the interpretation of our neutron scattering data we carried out these CEF calculations using a point charge model. We assumed an expansion of the perturbing CEF potential in spherical harmonics,

$$V(\Omega) = \sum_{\ell=4,6} g_\ell \sum_{m=-\ell}^{\ell} M_{\ell m} Y_{\ell m}(\Omega), \tag{6.1}$$

where the interaction strengths g_4 and g_6 are treated as free parameters. The spherical harmonic moments $\{M_{\ell m}\}$ are determined by the positions of the 12 As ions, which we assigned the (scaled) coordinates $\vec{x} = (\pm 1, \pm b, 0)$, $(0, \pm 1, \pm b)$, $(\pm b, 0, \pm 1)$. The nonzero independent moments for $\ell = 4, 6$ are $M_{40} = 21(1 - 3b^2 + b^4)/2\sqrt{\pi}(1 + b^2)^2$, $M_{60} = 3\sqrt{13}(2 - 17b^2 + 2b^4)/8\sqrt{\pi}(1 + b^2)^2$ and $M_{66} = -15\sqrt{3003}b^2(1 - b^2)/16\sqrt{\pi}(1 + b^2)^3$. The nonzero M_{66} for $b \neq 1$ (T_h symmetry) confirms the presence of the B_t^6 terms of Takegahara *et al.* [Eq.(7) of Ref. [143]], in addition to the usual B_c^4 and B_c^6 O_h-symmetry terms. (Note that the T_h-allowed moment M_{66} vanishes at the O_h-symmetry point $b = 1$.) We also confirmed that the other nonzero moments satisfy the ratios quoted in Eq.(7) of Ref. [143]. Unlike Takegahara *et al.* [143], we do not introduce a new parameter y for the T_h-symmetry terms, because they are completely determined by g_6 and the lattice parameter b in the point charge model. This was previously noted by Goremychkin *et al.* [21].

Diagonalization of this T_h CEF interaction within the Pr^{+3} $^3H_4$ nonet gives our results for the spectrum of CEF levels and their associated eigenvectors. These eigenvectors depend only on the ratio g_6/g_4 and the lattice parameter b; the energies in addition have an arbitrary overall scale. Our results for the spectrum for $b = 1$ (O_h symmetry) and $b = 0.4267$ ($PrOs_4As_{12}$ geometry) are shown in Figs. 1(b) and 1(d), using LLW normalization conventions [144]. (These conventions set our two Hamiltonian parameters in Eq.(1) to

$g_4 = (968\pi/21)x$ and $g_6 = (-5808\pi/221)(1 - |x|)$.) Note that the $b = 1$ and $b = 0.4267$ level schemes differ qualitatively, which demonstrates the importance of the T_h terms in this problem.

We find that the O_h singlet and doublet energy eigenvectors are unmodified by the T_h interaction, consistent with Takegahara *et al.* [143]. The singlet eigenvector (in a J_z^{tot} basis) is $|\Psi_1\rangle = \sqrt{7/12}|0\rangle + \sqrt{5/24}(|4\rangle + |-4\rangle)$ and the two doublet states are $|\Psi_{23a}\rangle = -\sqrt{5/12}|0\rangle + \sqrt{7/24}(|4\rangle + |-4\rangle)$ and $|\Psi_{23b}\rangle = \sqrt{1/2}(|2\rangle + |-2\rangle)$, consistent with earlier (numerical) results [143,144]. The singlet and doublet energy eigenvalues in our conventions are modified by the T_h interaction. In terms of the LLW variable x [144] and our parameter b they are $E_1 = -(16/13(1 + b^2)^2)(91x(1 - 3b^2 + b^4) - 20(1 - |x|)(2 - 17b^2 + 2b^4))$ and $E_{23} = -(16/13(1+b^2)^2)(13x(1-3b^2+b^4)+16(1-|x|)(2-17b^2+2b^4))$. The corresponding analytic results for the two T_h triplet states for general b are quite complicated, so we only present numerical results for these states.

The neutron transition intensities are defined by $I_{if} = |\langle f|J_z^{tot}|i\rangle|^2$, as introduced by Birgeneau [117]. (There is an implicit sum over initial and final magnetic quantum numbers.) Our T_h-symmetry results for these quantities are shown in Fig. 6.5(a). The values in the limits $x = \pm 1$ (no $\ell = 6$ term, hence O_h symmetry) implicitly check Birgeneau's numerical O_h results; see the off-diagonal entries in his Table 1(e). These O_h limits are indicated on the vertical axis of Fig. 6.5(a).

Next we compare the observed CEF levels and their neutron excitation intensities to the well-known LLW CEF results for O_h symmetry [Fig. 6.1(b)] and our calculated CEF predictions for $PrOs_4As_{12}$ under T_h symmetry [Fig. 6.1(d) and Fig. 6.5(a)]. Both O_h and T_h CEF spectra have x values that can accommodate a magnetic triplet ground state and a nearly degenerate singlet first excited state [vertical lines in Figs. 6.1(b) and (d)]. However, it is evident that the O_h scheme cannot explain the data because the observed 0.4 meV transition $\Gamma_4^{(2)} \rightarrow \Gamma_1$ is incorrectly predicted to have zero intensity due to the O_h symmetry. While in the T_h scheme the relative neutron excitation strengths of the higher levels (at 13 and 23 meV) predicted in Fig. 6.1(d) seem to be in good agreement with observation at low temperatures, the As CEF alone predicts an incorrect spectrum of levels [Fig. 6.1(d)], with the triplet $\Gamma_4^{(1)}$ being the highest excitation. The calculated neutron transition intensity shown in Fig.6.5(a) can not explain the observed intensity at

higher temperatures. As temperature increases, the excited states get populated and the excitations start to decrease in intensities. Meanwhile the new excited-state transitions start to increase. If $\Gamma_4^{(1)}$, instead of Γ_{23}, is the highest level, the intensity at 12.6 meV would not increase but that at 22.6 meV would, because the Γ_1 to Γ_{23} transition is not allowed even in T_h symmetry. Goremychkin *et al.* [21] showed that the highest level in the similar Sb material is the Γ_{23} doublet.

6.5 Combined Os-As CEF model

The twin constraints of having the Γ_{23} level at the top of the spectrum *and* having a large $\Gamma_4^{(2)} \leftrightarrow \Gamma_1$ neutron excitation strength requires both Os and As terms in the CEF interaction. We therefore introduce a combined Os-As Hamiltonian,

$$H = H(Os) + H(As). \tag{6.2}$$

Although this model nominally has four parameters ($g_4^{Os}, g_6^{Os}, g_4^{As}$ and g_6^{As}), only three are independent; g_4^{Os} and g_4^{As} cannot be distinguished because they are summed into a single coefficient of the O_h-symmetry $\ell = 4$ interaction. For this reason we introduce combined O_h-symmetry Os-As coefficients $g_4 = g_4^{Os} + g_4^{As}$ and $g_6 = g_6^{Os} + g_6^{As}$, which we normalize according to LLW conventions. As the $\ell = 6$ T_h-symmetry terms from $H(As)$ in the CEF are proportional to g_6^{As} alone, the strengths g_6^{Os} and g_6^{As} can be distinguished. We parametrize these two $\ell = 6$ interactions using the total O_h-symmetry g_6 and a T_h/O_h relative strength r_6, which is the ratio of the coefficients of Y_{62} to Y_{60} in the CEF potential. The energy levels of this Hamiltonian are $E_{4(2)} = -6g_4 - 8g_6 - f$, $E_1 = 28g_4 - 80g_6$, $E_{4(1)} = -6g_4 - 8g_6 + f$ and $E_{23} = 4g_4 + 64g_6$, where $f = ((20g_4 + 12g_6)^2 + 960\, r_6^2 g_6^2)^{1/2}$. For $r_6 = 0$ these reduce to the familiar LLW O_h spectrum. In the pure As model, r_6 is determined by CEF theory if we assume point As ions, and is given by $(11\sqrt{105}/4)b^2(1 - b^2)/(1+b^2)(1-(17/2)b^2+b^4)$. For $PrOs_4As_{12}$ we have $b = 0.4267$, which gives a rather large $r_6 = -6.901$. This drives strong level repulsion between the two triplets, which explains why the pure As spectrum of Fig.6.1(d) differs so greatly from the O_h (pure Os) symmetry spectrum of Fig.6.1(b).

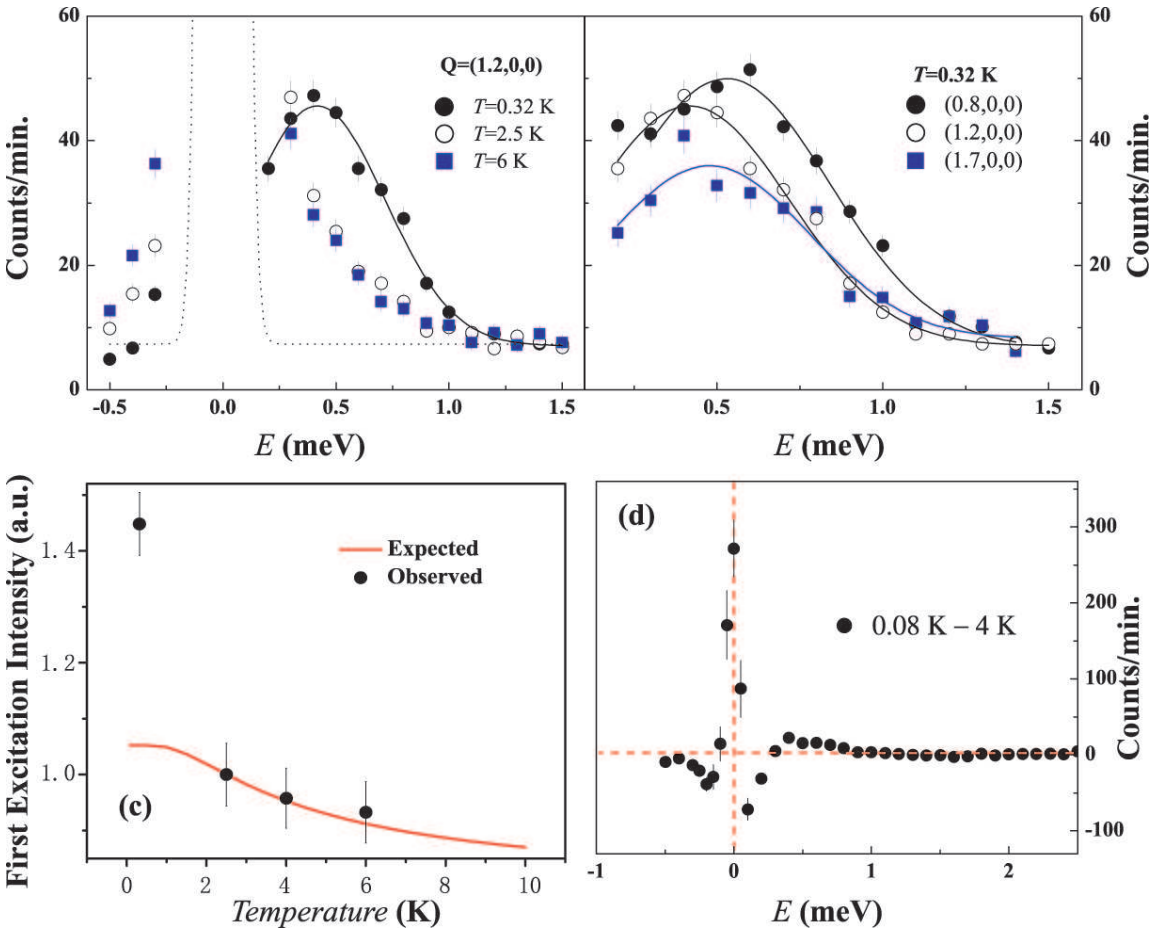

Figure 6.3: (a) Low energy spectrum of CEF excitations observed at $T = 0.32$, 2.5 and 6.0 K using the SPINS spectrometer at NCNR. (b) The wave vector dependence of the excitations at $Q = (0.8, 0, 0)$, $Q = (1.2, 0, 0)$, and $Q = (1.7, 0, 0)$. (c) The expected and observed temperature dependence of the intensity of the 0.4 meV mode. (d) The temperature difference spectrum between 0.08 K and 4 K, showing clear reduction in magnetic elastic scattering.

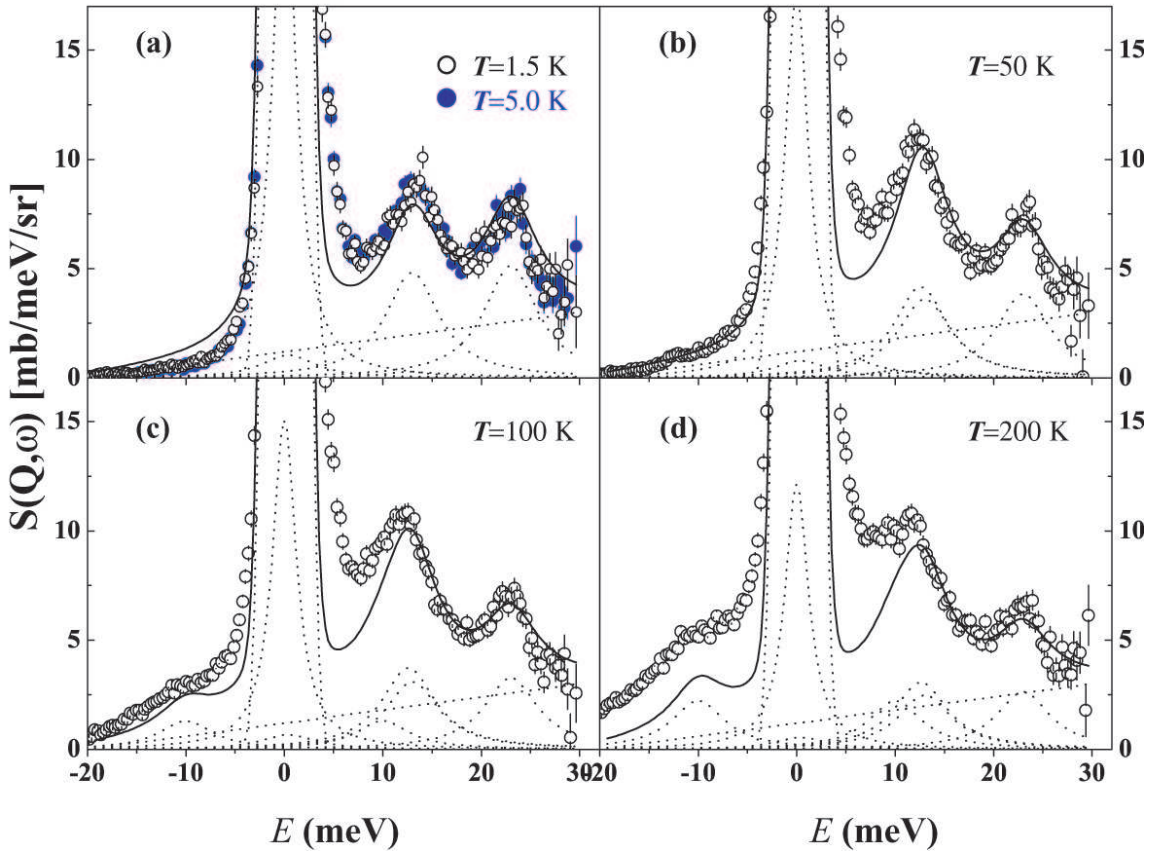

Figure 6.4: The temperature dependence of the excitations observed on HET with $E_i = 32$ meV at (a) $T = 1.5$ K, 5 K; (b) 50 K; (c) 100 K, and (d) 200 K. The lines are theoretical results for neutron excitation intensities, from the combined Os-As CEF model, with an arbitrary overall scale factor.

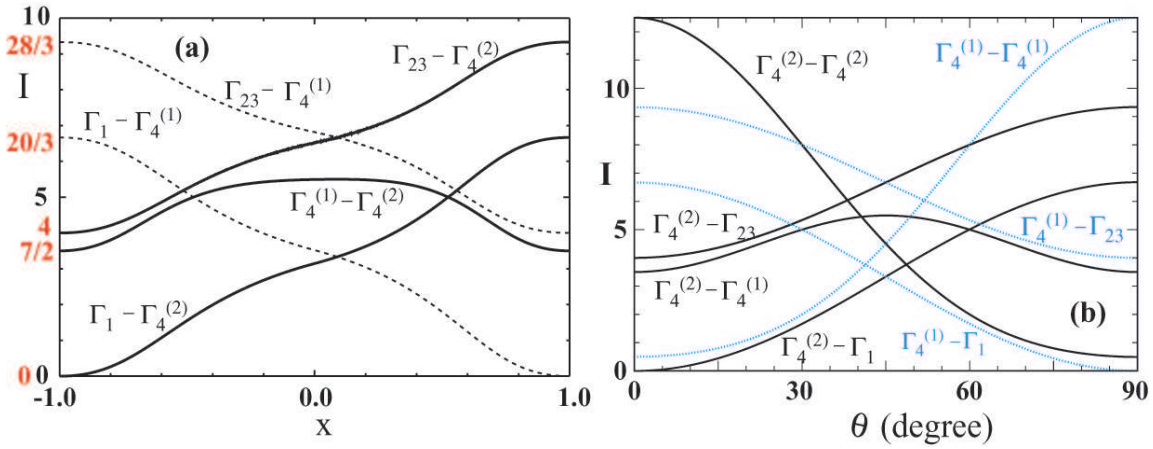

Figure 6.5: (a) The theoretical neutron transition intensity for As CEF alone with b=0.4267. (b) Neutron excitation intensities predicted by the combined Os-As CEF model.

Our experimentally observed CEF levels are close to but not exactly consistent with the predictions above of the mixed Os-As model, since the gap ratio $(E_{4(1)} - E_{4(2)})/(E_{23} - E_{4(2)}) \approx 0.57$ is slightly *below* the theoretical lower bound of 7/12. The parameters we estimate from the measured gaps are $g_4 \approx 0.24$ meV and $g_6 \approx 0.20$ meV. The value of r_6 is not determined by the measured energies due to the inconsistency mentioned above, although $r_6 \lesssim 0.5$ appears plausible. A more sensitive determination of r_6 is possible through the measurement of the inelastic neutron excitation intensities we discuss below.

The neutron excitation intensities in this combined Os-As Hamiltonian depend only on a single parameter θ, which is the mixing angle of the triplet energy eigenvectors when expanded in an O_h-symmetry $|3\rangle, |3'\rangle$ basis,

$$\begin{aligned} |4(1)\rangle &= +\sin(\theta)|3\rangle + \cos(\theta)|3'\rangle \\ |4(2)\rangle &= +\cos(\theta)|3\rangle - \sin(\theta)|3'\rangle. \end{aligned} \tag{6.3}$$

This mixing angle is related to the Hamiltonian parameters by $\tan(2\theta) = 2\sqrt{15}\, r_6/(5(g_4/g_6)+3)$. The singlet and doublet O_h energy eigenvectors are unchanged. The nonzero neutron excitation intensities in terms of $s = \sin(\theta)$ and $c = \cos(\theta)$ are $\Gamma_4^{(2)} \leftrightarrow \Gamma_1 = (20/3)s^2$, $\Gamma_4^{(2)} \leftrightarrow \Gamma_4^{(1)} = 7/2 + 8c^2s^2$, $\Gamma_4^{(2)} \leftrightarrow \Gamma_{23} = 4 + (16/3)s^2$, $\Gamma_1 \leftrightarrow \Gamma_4^{(1)} = (20/3)c^2$, $\Gamma_4^{(1)} \leftrightarrow \Gamma_{23} = 28/3 - (16/3)s^2$, $\Gamma_4^{(2)} \leftrightarrow \Gamma_4^{(2)} = (25/2)(1 - (4/5)s^2)^2$, and $\Gamma_4^{(1)} \leftrightarrow \Gamma_4^{(1)} = (1/2)(1 + 4s^2)^2$.

The calculated neutron scattering intensity of different transitions as a function of θ is shown in Fig. 6.5(b). We recover the O_h-symmetry results of Birgeneau (Table 1(e) of Ref. [117]) for $s = 0, c = 1$.

We carried out a least-squares fit of our neutron excitation data at 1.5 K, 50 K, 100 K and 200 K (Fig. 6.4) to the theoretical intensities given above, which gives an estimate of the triplet mixing angle θ in $PrOs_4As_{12}$,

$$\theta \approx 22.5^{\circ}. \tag{6.4}$$

When combined with the values of g_4 and g_6 from the spectrum, this θ corresponds to $r_6 \approx 1.2$. In this fit the relatively isolated $\Gamma_4^{(2)} \rightarrow \Gamma_4^{(1)}$ peak at 23 meV was used to infer the background, which was taken to be constant plus linear. The assumed lineshapes were Lorenzians with a common linewidth, fixed by the 23 meV peak. The calculated intensities of the individual transitions (dotted lines) and the total intensity (solid lines) for each temperature are shown in Figs. 4(a)-(d). We note that the intensity reduction at 0.4 meV on warming from 0.32 K to 2.5 K is larger than that expected from the CEF model [Fig. 6.3(c)], thus suggesting Pr-Pr interactions below T_N (=2.3 K) are important. On the other hand, the large difference between the calculated and expected intensity around 8 meV in the 200 K data is presumably due to thermally populated phonons (Fig. 6.2(a)).

6.6 Field effect on the CEF gap

If the ground state of $PrOs_4As_{12}$ is indeed the $\Gamma_4^{(2)}$ triplet, application of a magnetic field should Zeeman split it, resulting in a field dependent energy gap. There should also be a reduction in the intensity of the zero-energy $\Gamma_4^{(2)} \rightarrow \Gamma_4^{(2)}$ magnetic scattering. Figure 6.6 shows that these expectations are indeed qualitatively satisfied. The first excited state at 0.4 meV shifts toward higher energies as the applied field increases. The field-dependent transition energy is linear only at higher fields (between 6 T and 11 T). The drop of intensity in the elastic channel is almost constant for all applied fields, as shown in the inset of Fig. 6.6(b). Figure 6.6(c) shows that the wave vector dependence is also present with applied magnetic field ($H = 9\ T$). Normally the field-splitting of the ground state multiplet would

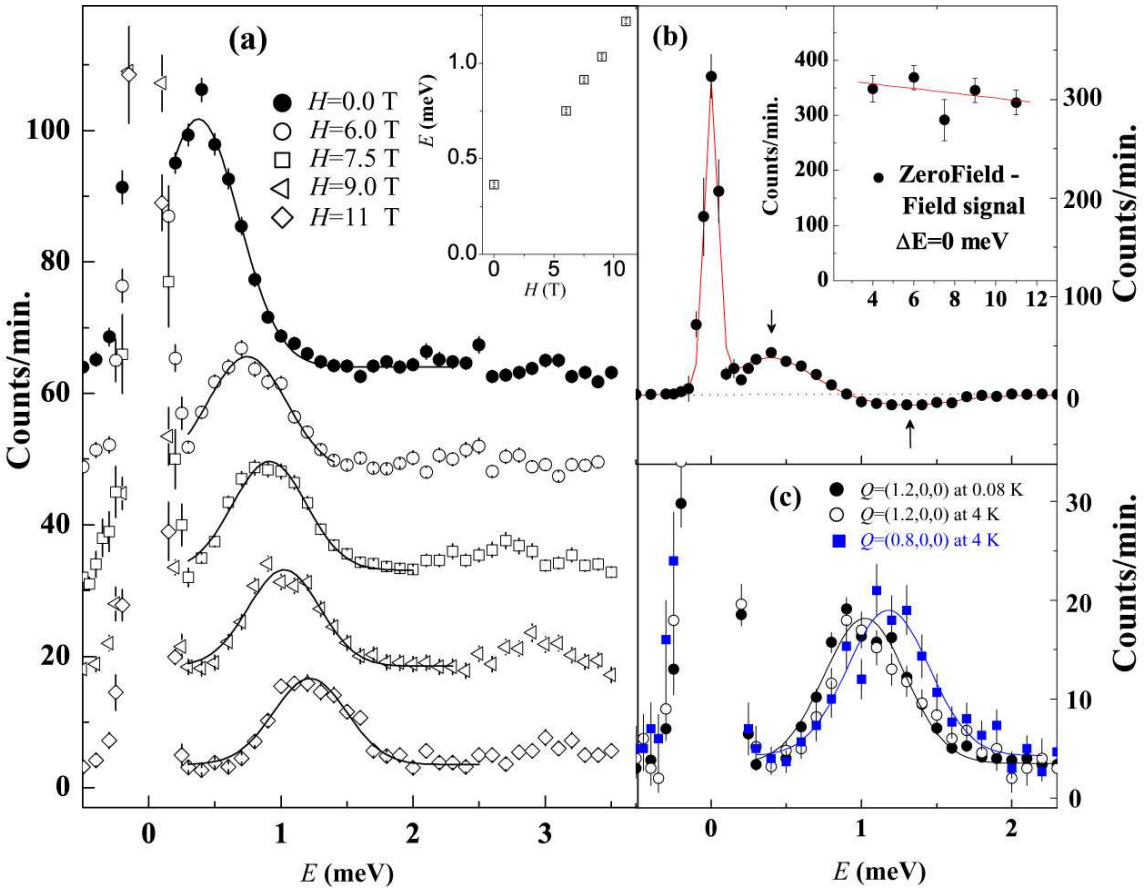

Figure 6.6: (a) The magnetic field dependence of the low-lying CEF excitations at $Q = (1.2, 0, 0)$ and $T = 0.08$ K. The inset shows the field dependence of the first excited state. (b) The difference spectrum between 0 T and 11 T at $Q = (1.2, 0, 0)$ and $T = 0.08$ K. The effect of an applied field is to suppress intensity at $\hbar\omega = 0$ meV, and to split the spin-triplet ground state; the latter results in the field dependence of the 0.4 meV peak in (a), which may involve an intra-triplet transition. The elastic intensity suppression effect essentially disappears for fields above 4 T. (c) The field-induced CEF excitation at ≈ 1.1 meV is weakly wave vector dependent, and shows essentially no temperature dependence between $T = 0.08$ K and 4 K.

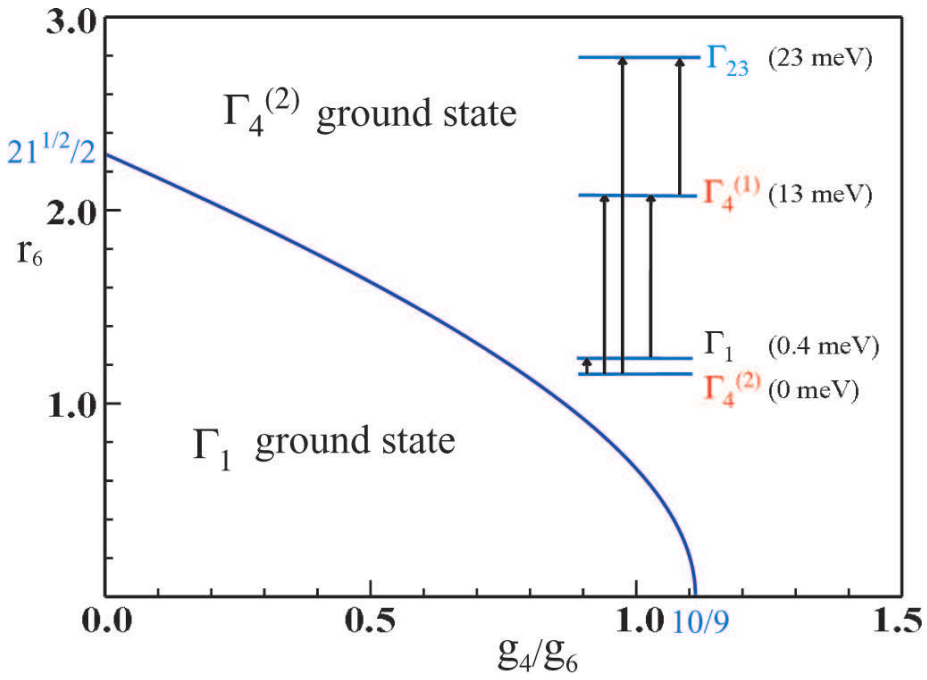

Figure 6.7: The boundary between singlet and triplet ground states in skutterudites ($E_1 = E_4^{(2)}$) as a function of r_6 and g_4/g_6, and the observed $PrOs_4As_{12}$ spectrum.

be a very clear test of our $\Gamma_4^{(2)}$ triplet assignment for the ground state. However, $PrOs_4As_{12}$ is complicated by the near degeneracy of the $\Gamma_4^{(2)}$ and Γ_1 levels, which mix strongly under an applied field. This results in a more complicated spectrum of low-lying states, with several low-field level crossings and neutron scattering intensities that are also modified by their field-induced $\Gamma_4^{(2)}$-Γ_1 mixing.

Our determination of the CEF levels in $PrOs_4As_{12}$ reveals the reasons for the wide range of behaviors in different FS. The spectrum of CEF levels is largely determined by the O_h symmetry field of the eight nearest neighbor ions, and for Os the near equality of the $\ell = 4$ and $\ell = 6$ strengths g_4 and g_6 implies nearly degenerate low-lying singlet (insulator) and triplet (AF) levels. The low temperature magnetic properties are determined by which of these phases happens to be the true ground state. In the CEF model, this is specified by the two parameters g_4/g_6 and r_6 (Fig. 6.7); in $PrOs_4As_{12}$, which has a triplet ground state, we estimate $g_4/g_6 \approx 1.15$ and $r_6 \approx 1.2$. The T_h symmetry pnictogen CEF (proportional to r_6) acts to stabilize the triplet state, and can itself lead to a triplet ground state if r_6 is sufficiently large to cross the phase boundary shown in Fig. 6.7.

In principle, one can extend our approach to calculate the ground states of other Pr-FS by determining its crystal structure and g_4/g_6 ratio. The necessity of using the T_h-symmetry of As rather than the O_h-symmetry pure Os form to explain the observed excitations shows that the detailed pnictogen geometry is important in determining the CEF levels. Indeed, the AF-ordered ground state in $PrOs_4As_{12}$ can arise from a $\Gamma_4^{(2)}$ triplet magnetic ground state, while the superconducting $PrOs_4Sb_{12}$ has nonmagnetic Γ_1 singlet ground state. The nearly degenerate first excited state Γ_1 at 0.4 meV ($\sim$ 4 K), and its temperature and field dependence (Figs. 4 and 6), may explain the presence of multiple transitions in the specific heat (in $C(T)/T$ versus T) and its field dependence [136,137,140].

6.7 conclusions

To understand the observed Pr^{3+} CEF levels, one must incorporate the As ions' contribution to the CEF Hamiltonian [142, 143], in addition to the usual Os cubic field terms. A comparison of our CEF calculations using this more general Hamiltonian with our experimental results shows that the Pr^{3+} CEF level scheme in $PrOs_4As_{12}$ consists of a $\Gamma_4^{(2)}$ magnetic triplet ground state, a nearly degenerate Γ_1 singlet excitation, and higher $\Gamma_4^{(1)}$ magnetic triplet and Γ_{23} nonmagnetic doublet excited states. We find that contributions in the CEF Hamiltonian due to As are important in determining the neutron excitation intensities in $PrOs_4As_{12}$; our results differ qualitatively from the predictions of the conventional CEF Hamiltonian [117, 144], and therefore provide a microscopic understanding for its AF ground state.

Chapter 7

Magnetic structure and Field-induced magnetic transitions in $PrOs_4As_{12}$

In this chapter, I present the elastic neutron scattering study on the nuclear and magnetic structure of the $PrOs_4As_{12}$ single crystals and effect of external magnetic field on the magnetic properties.

7.1 Introduction and motivations

As described in the introduction of the previous chapter, the Pr-base filled skutterudite (FS) compounds exhibit a great variety of ground state, such as multipole ordering, small gap insulators, conventional superconductivity, unconventional superconductivity and magnetic ordering. $PrOs_4As_{12}$ is the only one, so far, that has been found with antiferromagnetic ground state [136, 137]. It is also revealed the existence of a second phase at temperatures below 2.3K and in field below approximately 3T [137]. The field induced phases have been observed in various FS compounds. The mechanism of the induced phases also varies from compound to compound. P. Ho *et al.* [140] further studied the field-induced transitions with susceptibility measurement and found that the AFM phase is suppressed by application of magnetic field and undergoes a transformation to the paramagnetic-metal (PMM) phase.

This process is reported to actually consist 3 or 4 meta-magnetic transitions, a magnetic-field induced first-order phase transition from the paramagnetic to the ferromagnetic state. The field position of these transitions strongly depends on the orientation of the crystals in the field.

In light of the low temperature behavior of other Pr-based skutterudites such as $PrFe_4P_{12}$, it is likely that the second phase has either a magnetic or a quadrupolar nature. Based on our CEF measurements as described in the previous chapter, which support a scheme with magnetic $\Gamma_4^{(2)}$ as the ground state, we can almost certainly rule out the possibility of a quadrupolar ordering because that requires a non-magnetic doublet Γ_{23} to be the ground state. It is therefore important to unambiguously determine the magnetic structure of the $PrOs_4As_{12}$ compound and its change when magnetic field is applied.

7.2 Experimental details

The method of crystal growth is described in the previous chapter. To determine the exact spin orientation of $PrOs_4As_{12}$ and the nature of the other field-induced phases, 381 pieces of tiny $PrOs_4As_{12}$ single crystals of total weight of $\sim$700 mg have been co-aligned and glued with on two Al plates. The typical shape of the crystals, the method of coalignment and the orientations of the sample holders are shown in fig. 7.1. The quality of the single crystal array is checked with triple-axis spectrometer BT7 at the NIST Center for Neutron Research. The sample array is aligned in the (h, h, l) scattering plane and mounted on a He3 cryostat. The mosaic in the (H, H, L) scattering plane is found to be 1.4° for (0,0,2) and 1.3° for (2,2,0), which is quite acceptable for elastic neutron scattering experiment. The powder diffraction was carried out on the high resolution powder diffractometer. The elastic neutron scattering on single crystal assembly was conducted on BT7 and BT9. The sample array is aligned in the (H, H, L) and $(H, 0, L)$ scattering planes, and mounted on a He3 cryostat. The field effect measurements were carried out with a 7T ^{3}He cryostat.

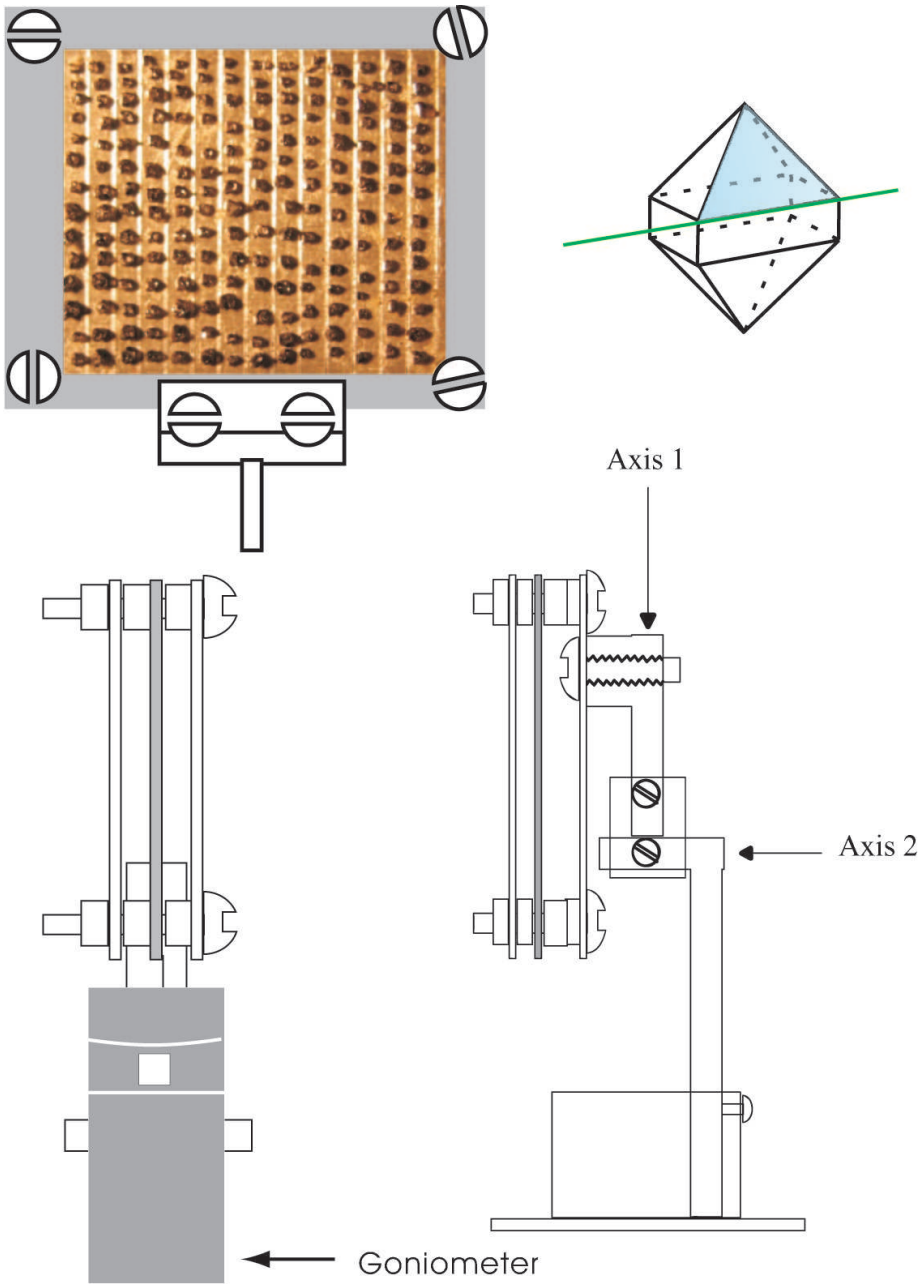

Figure 7.1: 381 pieces of tiny single crystals of 0.67 gram were co-aligned onto both sides of a Al plate. The single crystal array was then sandwiched by two other Al plates for protection, and aligned to (H,H,L) and (H,K,0) zones using the two assemblies for elastic neutron scattering measurements.

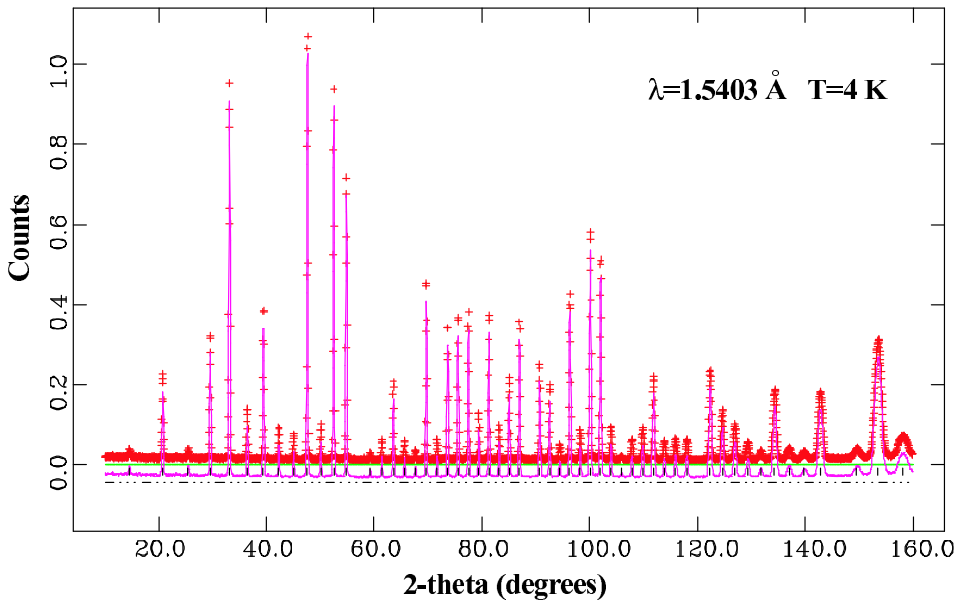

Figure 7.2: The observed and calculated (solid line) neutron powder diffraction profiles for the $PrOs_4As_{12}$ sample. The lower sold lines show the difference profiles and the tick marks show the reflection positions.

7.3 Determination of nuclear and magnetic structures

The neutron diffraction patterns were analyzed by the Rietveld method using GSAS (fig. 7.2) and showed single phase $PrOs_4As_{12}$ with no observable impurity phases.. The structural refinement shows that the unit cell of the crystal examined has the $LaFe_4P_{12}$ structure ($Im-3$ space group). A unit cell parameter a=8.5319 $\AA$ was determined. The refined parameters and fractional coordinates for T=4 K are shown in Table 1. There is no structural change or transition at low temperatures (T<15 K).

The magnetic reflection is obtained by subtracting the 6 K spectrum from the 0.63 K one. Fig. 7.3 shows the outcome the this subtraction and clearly, there are magnetic intensities at positions consistent with $(h+0.5,k,l)$, where h,k and l are miller indices of the cubic unit cell. The observed magnetic peak suggested a magnetic unit cell that doubles the structural unit cell along one axis. This is clear indication that $PrOs_4As_{12}$ has A-type magnetic structure, i.e., spins of the Pr^{3+} ions are aligned ferromagnetically in one of the cubic planes while the alternate planes have opposite spin direction. The order parameters were determined by measuring the temperature dependence of the magnetic peak at 2θ=17.9°. The Néel temperature was determined be 2.28 K.

Table 7.1: Refined lattice parameters and fractional coordinates

Atom	x	y	z	U_{eq} ($\mathring{A}^2 \times 10^3$)	occupancy factor
Pr	0	0	0	2	0.9223
Os	0.25	0.25	0.25	8	1
As	0	0.348429	0.148129	24	1

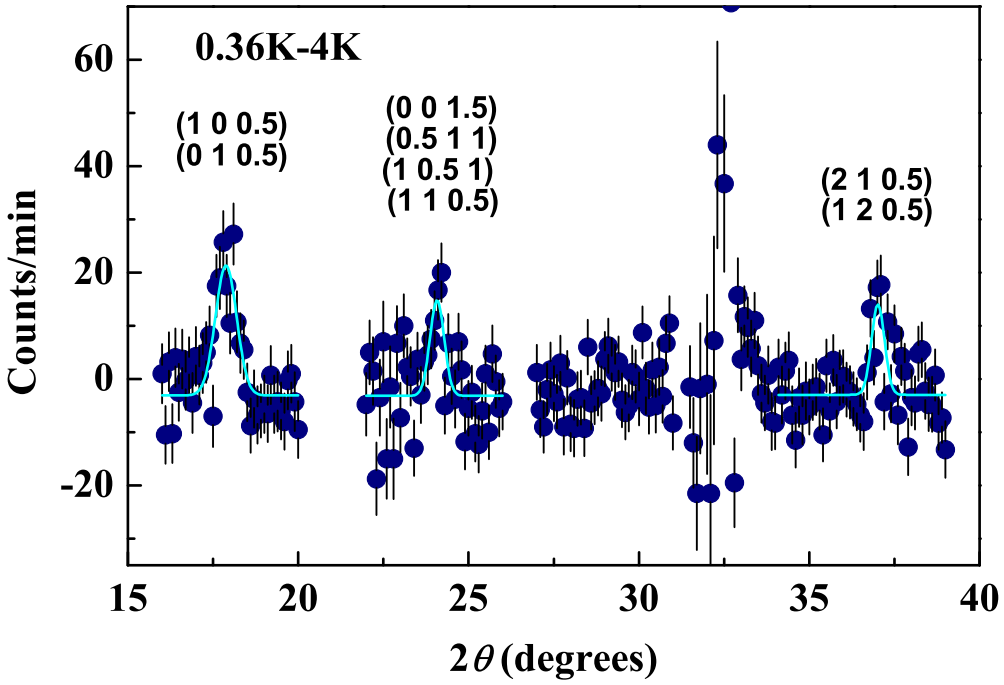

Figure 7.3: Intensity spectrum at 0.63K after the subtraction of 4K spectrum. The fluctuation of the intensity at $2\theta \sim 30^\circ$ is the result of imperfect subtraction of nuclear peak that shifts with temperature change.

In order to determine the exact direction of the Pr^{3+} moment, the single crystal array was used for elastic neutron scattering measurements. The array is aligned in the (H, H, L) scattering plane and mounted on a ^{3}He cryostat at 0.36 K and 4 K respectively in 2-axis mode. Rocking scans are carried out for nuclear as well as the magnetic peaks. Some probed positions and observed magnetic peaks are shown in fig.7.4 No peak has been observed in the [0,0,L] direction. The second panel on the left shows identical scans at 0.36 K (solid square) and 4 K (open square), and the rest panels show scans at 0.36 K. The temperature dependence of the (1,1,0.5) magnetic peak is shown in figure 7.5, which gives T_N=2.28 K and confirms the powder measurement.

The absence of the $(0,0,L/2)$ magnetic peaks suggests that the Pr^{3+} moment has no perpendicular component when it is probed at these positions. In other words, the moment is along the [0,0,L] direction. This is just a speculation, however, that needs to be proved. The integrated intensities of the rocking scans of all the magnetic peaks have been used to fit for the exact spin orientation of the Pr^{3+} ions.

As depicted in fig. 7.6(a), the blue arrow $\vec{S}$ represents the Pr^{3+} moment and the green arrow represents the reciprocal space vector. The angle between the vector and the [0,0,L] direction is α, and the angle between the moment and the [0,0,L] direction is β. For every magnetic peak, α is known. β is then used as a variable to calculate the relative intensities of the magnetic peaks and fit to the observed data. The resultant value of β gives the spin direction of the Pr^{3+} ions. The least square fitting of the intensities as functions of α and β gives β=2.4°, very close to zero.

7.4 Field effect on the magnetic scatterings: $H//[1, \bar{1}, 0]$

The L-scans and H-scans were carried out in the (H, H, L) scattering plane, as shown in figure 7.7. The black solid circles in Figs. 7(a), (b) and (c) show clear magnetic peaks at (1,1,0,5), (1,1,1.5), (1,1,2.5), (2,2,0.5) and (2,2,1.5) positions. These peaks disappear when magnetic field $H = 1.8\ T$ is applied, as shown by the red circles.

In this scattering zone, when a vertical field is applied, the sample is in a field along $[1, \bar{1}, 0]$ direction. Figure 7.8 summarizes the effect of magnetic field on the magnetic peak as well as the nuclear peak. At T=0.5 K the intensity of (1,1,0.5) goes through two bumps

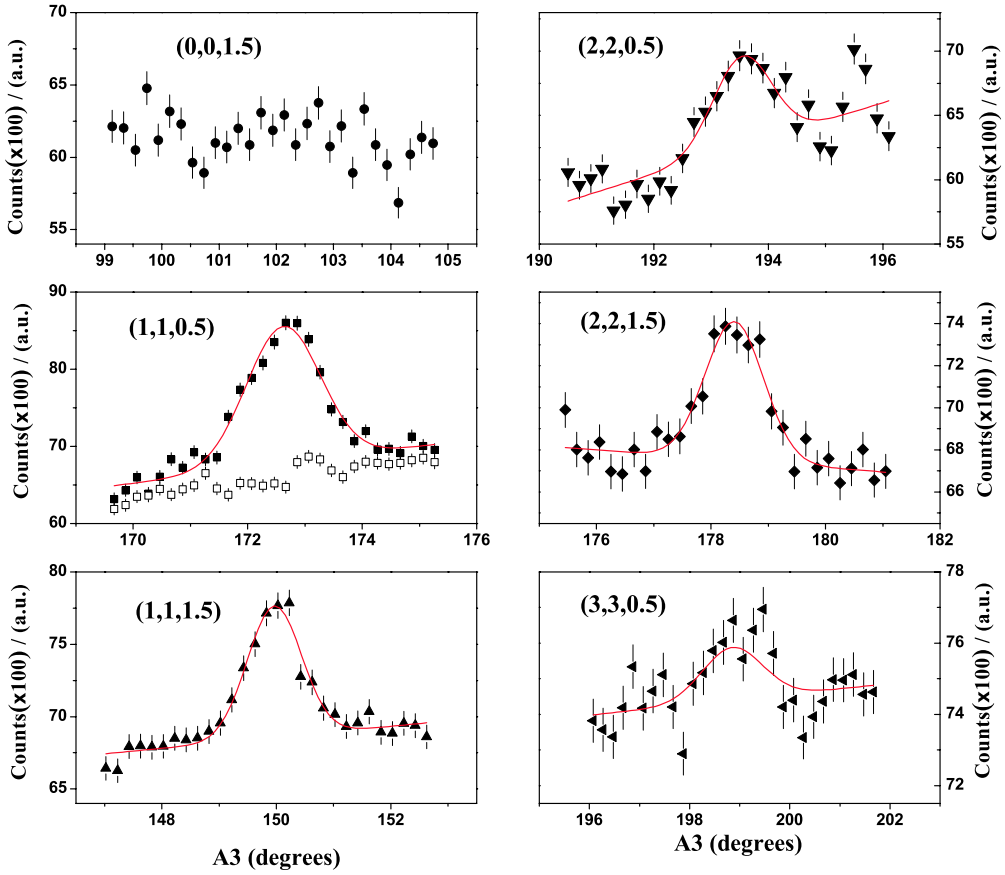

Figure 7.4: Rocking scans of some typical magnetic positions in the (H, H, L) scattering plane. The open square in the 2nd panel represents scan at 4 K. All others are scans conducted at 0.36 K.

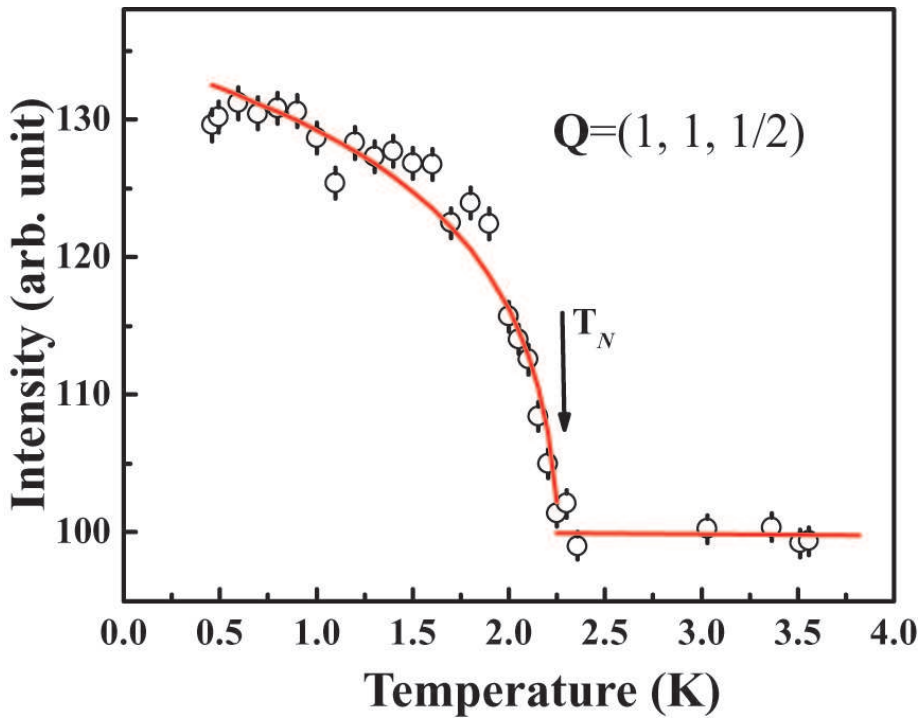

Figure 7.5: Temperature dependence of the intensity of (1,1,0.5) magnetic peak.

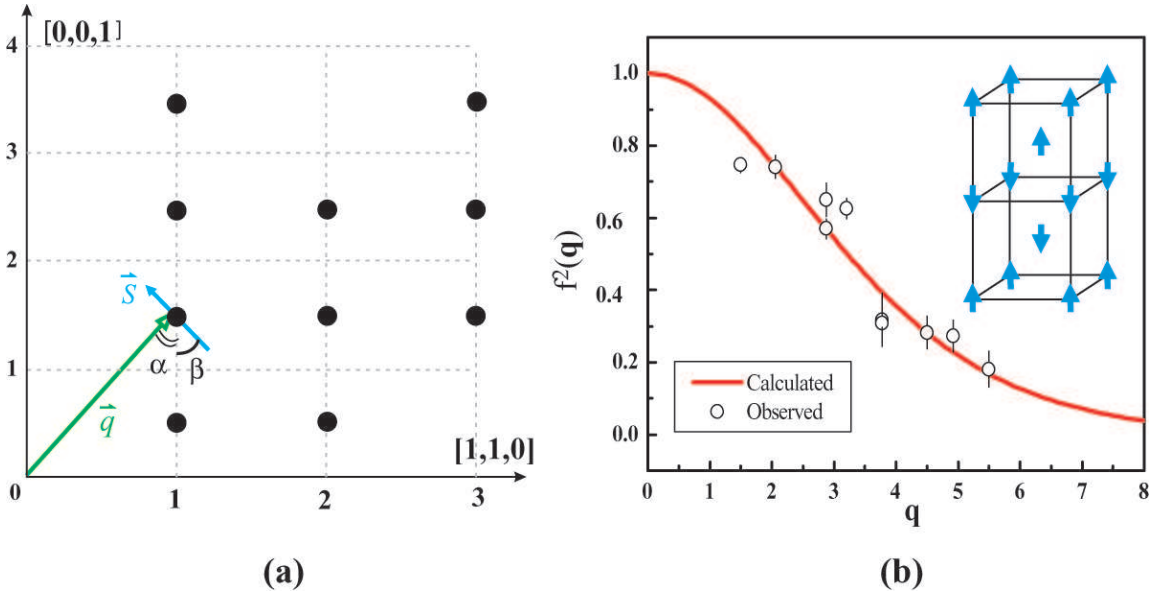

Figure 7.6: (a) Schematic view of the observed magnetic peaks and angles between the moment direction and the wave vector in reciprocal space. (b) The integrated intensities of the observed magnetic peaks are fit to the generic magnetic form factor of Pr^{3+}

before it vanishes at H=1.5 T, as shown in fig. 7.8(a). The complete disappearance of the magnetic peak at H=1.5 T corresponds to a sharp peak in the susceptibility measurement [140]. As of the two bumps, only the one at ∼1meV has a counterpart in the susceptibility measurements [140]. As temperature rises the critical field decreases gradually and becomes 0.75 T at T=1.9 K. However the bumps remains the universal feature for the entire temperature range. Throughout the fixed-temperature field swipe, the intensity at the (0,0,1.5) position has been monitored. Other than the background increase, no new peaks have been observed when field is applied (fig. 7.8(d)). This indicates that the transition at the critical field is first order, and that there is no canting of the spins at the field values where (1,1,0.5) shows two maxima. Fig. 7.8(b) shows the resultant H-T phase diagram of the AFM ground state, and it is the paramagnetic metallic phase outside the transitions. Fig. 7.8(c) shows the change of intensity of the nuclear peak position (1,1,0). At $T = 0.5\ K$, the intensity starts to increase when the applied field reaches $\sim 0.75\ T$. The increase remain linear up to $H = 2\ T$. Above T_N at $T = 2.5\ K$, the increase starts as soon as field is applied and the total intensity gain is less than that of $T < T_N$. Figure 7.9 shows the rocking scans of the magnetic peaks at $H = 0.4\ T$ and $H = 1\ T$. Except the high-Q peaks (2,2,1.5) and (2,2,2.5) whose intensities are too weak, all other magnetic peaks show field-dependent intensity that is consistent with fig. 7.8(a): the maximum integrated intensity occurs at $H = 0.4\ T$.

7.5 Field effect on the magnetic scatterings: $H//[0,1,0]$

Considering the nuclear structure alone, $(H,K,0)$ zone, $(0,K,L)$ and $(H,0,L)$ scattering planes are equivalent because of the cubic symmetry. One defines the scattering plane to be $(H,0,L)$ by letting L to bear the half integer of the magnetic peak. When the sample is aligned in the $(H,0,L)$ zone and field applied to the $[0,L,0]$ direction. The field dependent intensity of (1,0,-0.5) magnetic peak is similar to that of the (1,1,0.5). At $T = 0.5\ K$ with increasing field, it increases to a maximum at $H \approx 0.5\ T$, then drops and vanishes at critical field $H \approx 1.2\ T$. Identical measurement on the (2,0,-0.5) magnetic peak confirms the critical field, as shown in fig 7.10(a). The critical field decreases systematically with increasing temperature (fig. 7.10(b)). At $T = 1.9\ K$, the critical field becomes $H = 0.8\ T$.

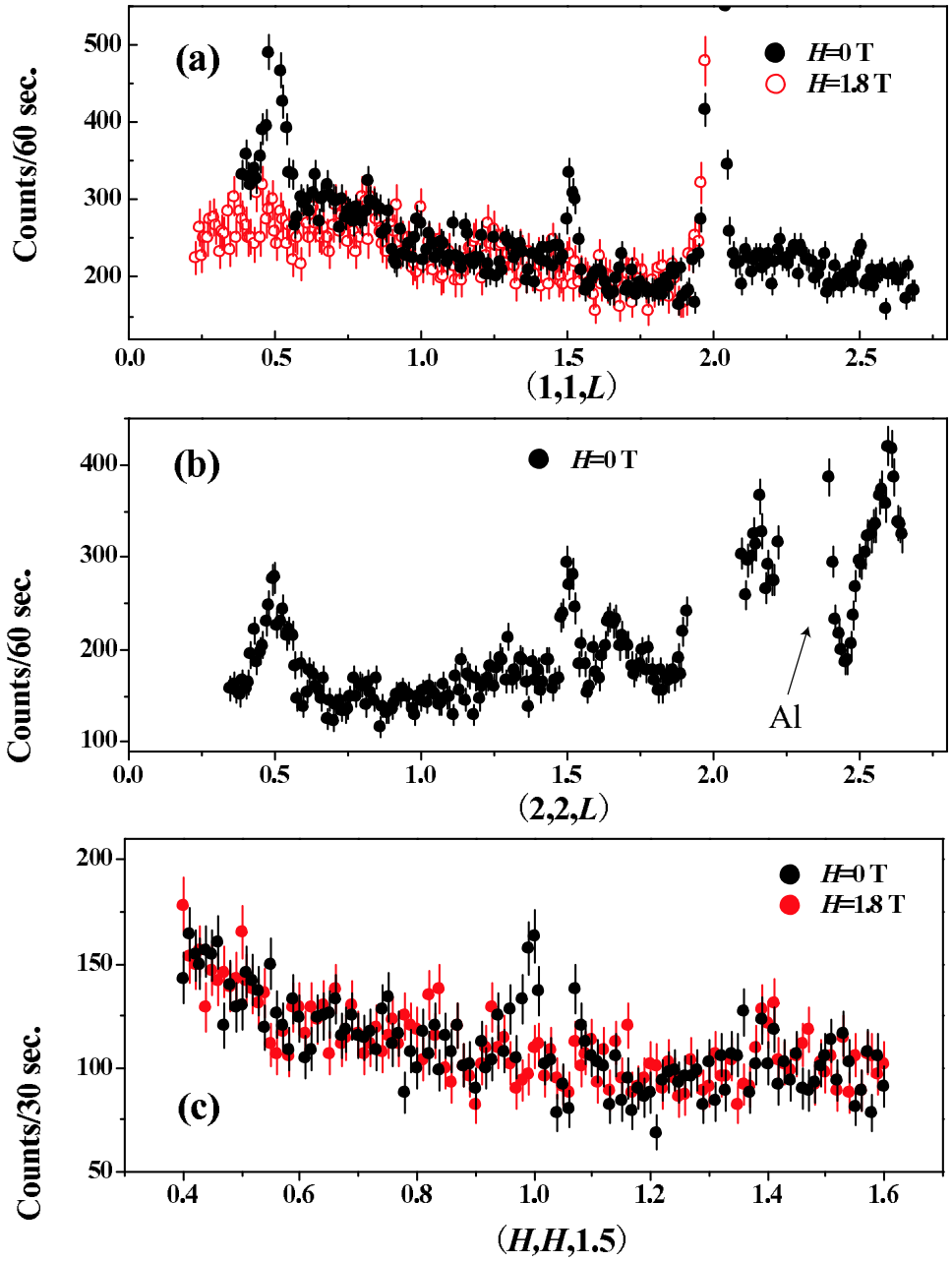

Figure 7.7: (a) The [1,1,L] scans with (red open circles) and without (black solid circles) magnetic field; (b) The [2,2,L] scans and (c) The [H, H,1.5] scans with and without field.

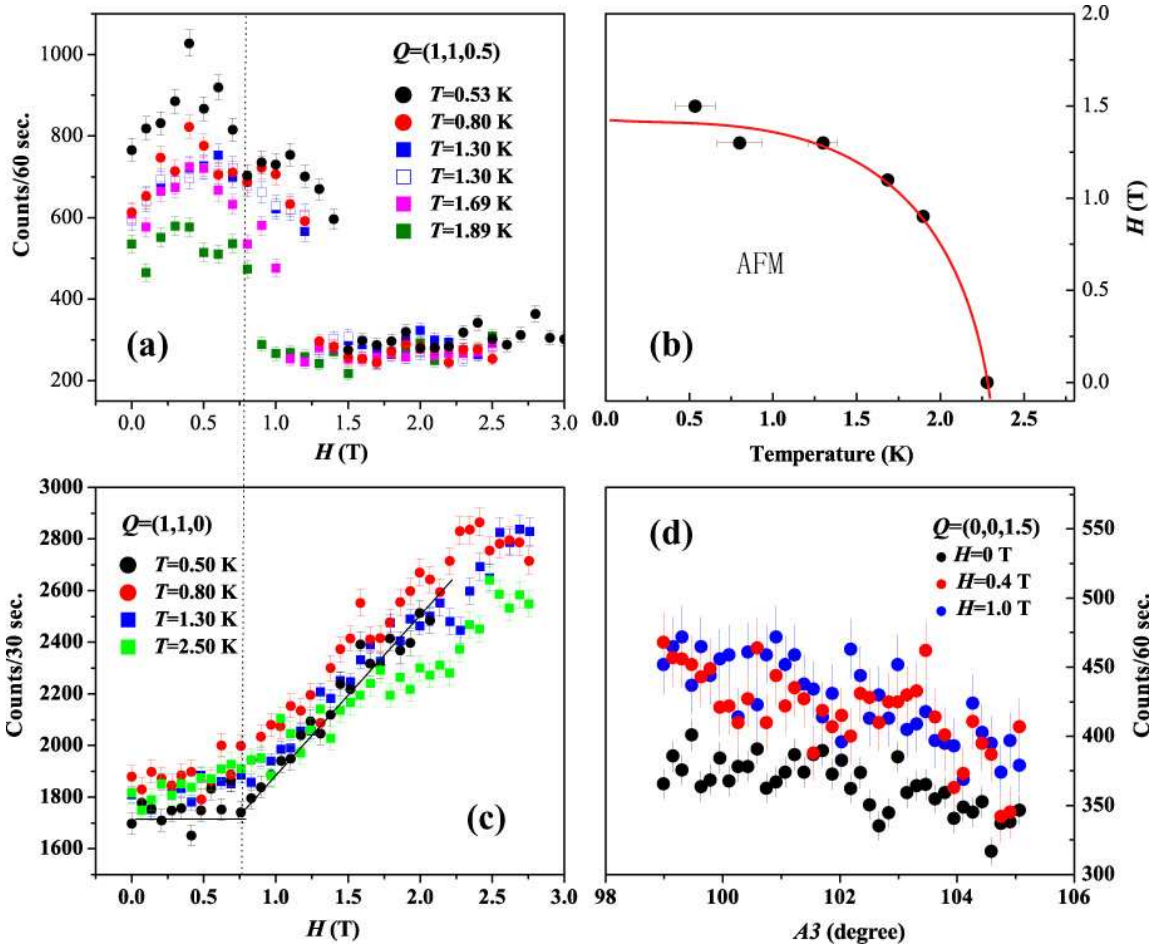

Figure 7.8: (a) The effect of magnetic field on the intensity of (1,1,0.5) at different temperatures. (b) Field-temperature phase diagram. The region outside the transition is the paramagnetic metallic phase. (c) The effect of field on the intensity of nuclear peak (2,0,0) at different temperatures. (d) No peak at (0,0,1.5) position has been observed under any magnetic field.

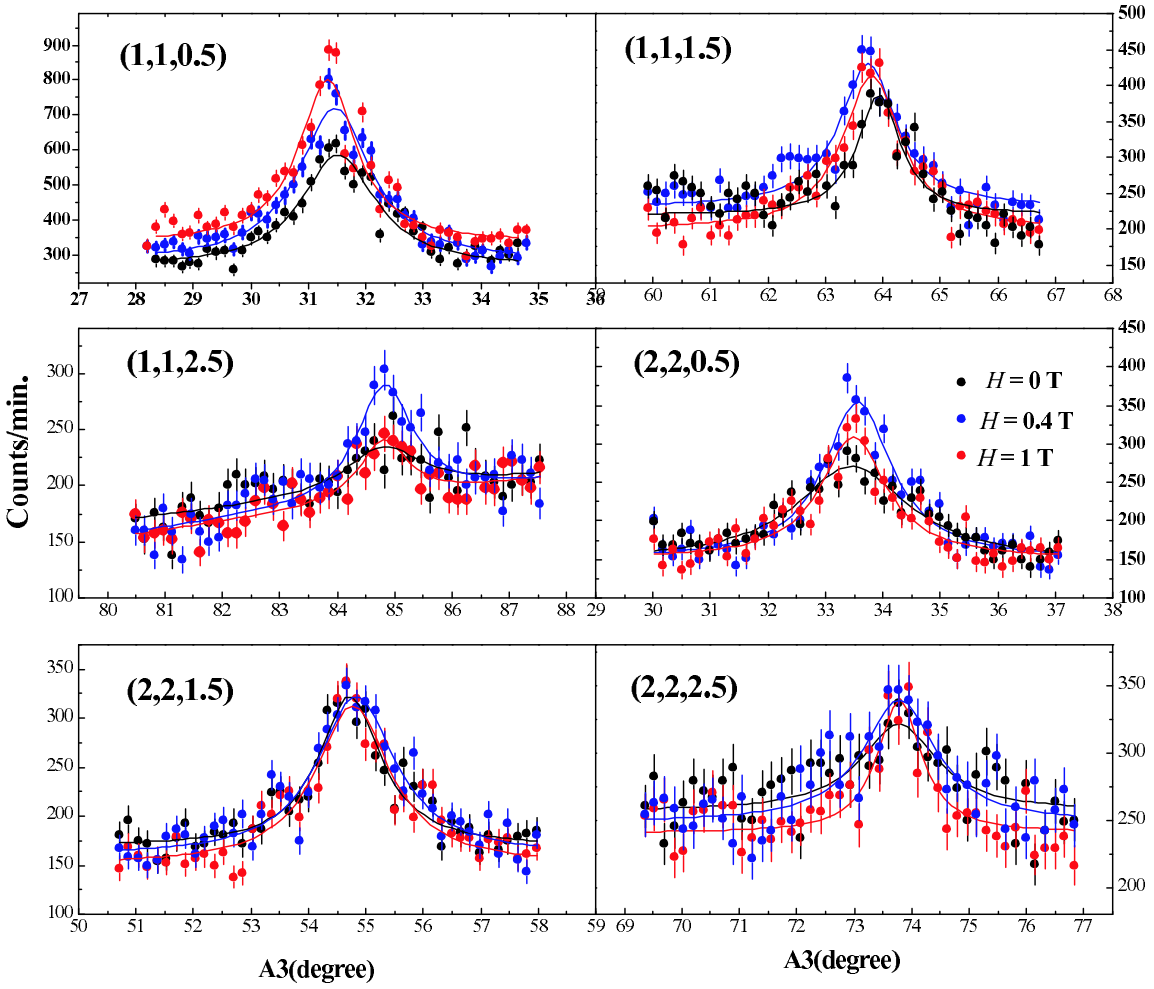

Figure 7.9: (a) The effect of magnetic field on the intensity of (1,1,0.5) at different temperatures. (b) Field-temperature phase diagram. (c) The effect of field on the intensity of nuclear peak (2,0,0) at different temperatures. (d) No peak at (0,0,1.5) position has been observed under any magnetic field.

As shown in fig. 7.10(c), the intensities at nuclear peak positions have different behavior than that with $H//[1,\bar{1},0]$. Both (2,0,0) and (2,0,2) drop in intensity as soon as the field is applied, and reach the minimum at $H \sim 0.6\ T$ then stabilizes. The $H-T$ phase diagram has similar shape with $H//[1,\bar{1},0]$, but lower critical field.

7.6 Field effect on the magnetic scatterings: $H//[0,0,1]$

Although the alignment is defined to be in the $(H,0,L)$ zone with the field along the b-direction, there is still a way to probe the effect of c-direction field on the magnetic scattering without changing the configuration. The idea is to change the scattering plane by tilting the goniometer so that a high-Q magnetic peak position can be reached. The procedure is the following: (1) define the scattering plane to be in the $(H,K,0]$ zone; (2) find the (4,0,0) peak; (3) tilt the $7T$-magnet about the b-axis (7.125°) to reach the (4,0,0.5) position; (4) redefine this position as (0,0,4.0311) and carry out rocking scan for this peak. This field dependence and rocking scans are summarized in figure 7.11. As the figure shows, when the field is applied along the c-direction, the magnetic peak intensity starts to decrease as soon as the magnetic field is turned on and is completely suppressed at $H = 0.6\ T$.

7.7 Discussions and Conclusions

The initial increase of magnetic intensities when small field is applied in [1,-1,0] and [0,1,0] direction is not likely caused by the re-orientation of the spins due to the following 3 reasons: (1) (0,0,1.5) peak remained its zero intensity when the (1,1,0.5) and (1,0,0.5) reach their maximum intensities at H=0.4T and H=0.6T; (2) The rocking scans of most magnetic peaks show increase at $H = 0.4\ T$, no peak is suppressed in intensity which can not be explained if spin direction is changed; (3) our calculation shows that that canting can only diminish the magnetic intensities of all the magnetic peaks. In addition, it is quite surprising to find out that the critical field ($H_C = 0.6\ T$)for field along the spin direction ($H//[0,0,1]$) is much smaller than those when fields are perpendicular to the spin direction ($H_C = 1.5\ T$ for $H//[1,\bar{1},0]$ and $H_C = 1.2\ T$ for $H//[0,1,0]$). We believe it is the change

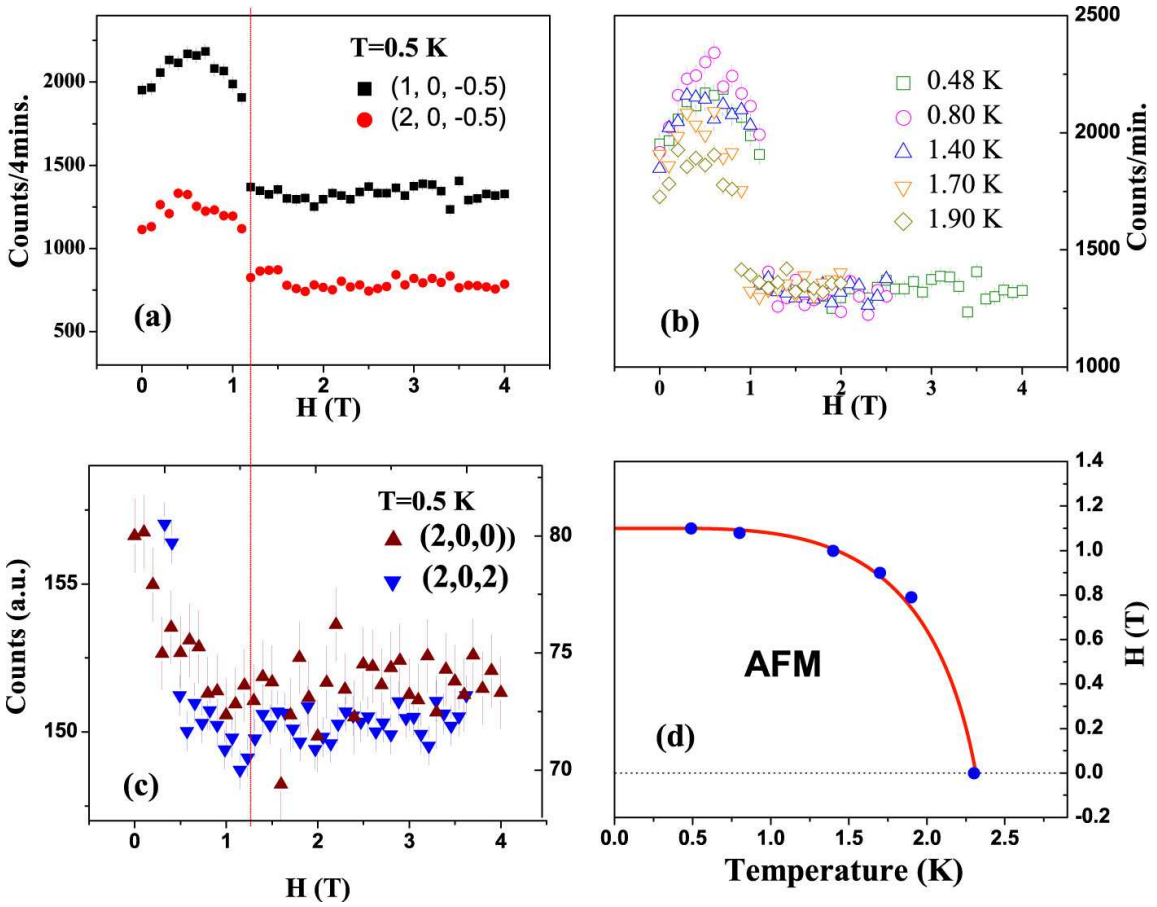

Figure 7.10: (a) The effect of magnetic field on the intensity of (1,0,-0.5) and (2,0,-0.5). (b) Suppression of magnetic scattering at (1,0,-0.5) with applied magnetic field at different temperatures. (c) The effect of field on the intensity of nuclear peak (2,0,0) and (2,0,2) at different temperatures. (d) Field-temperature phase diagram.

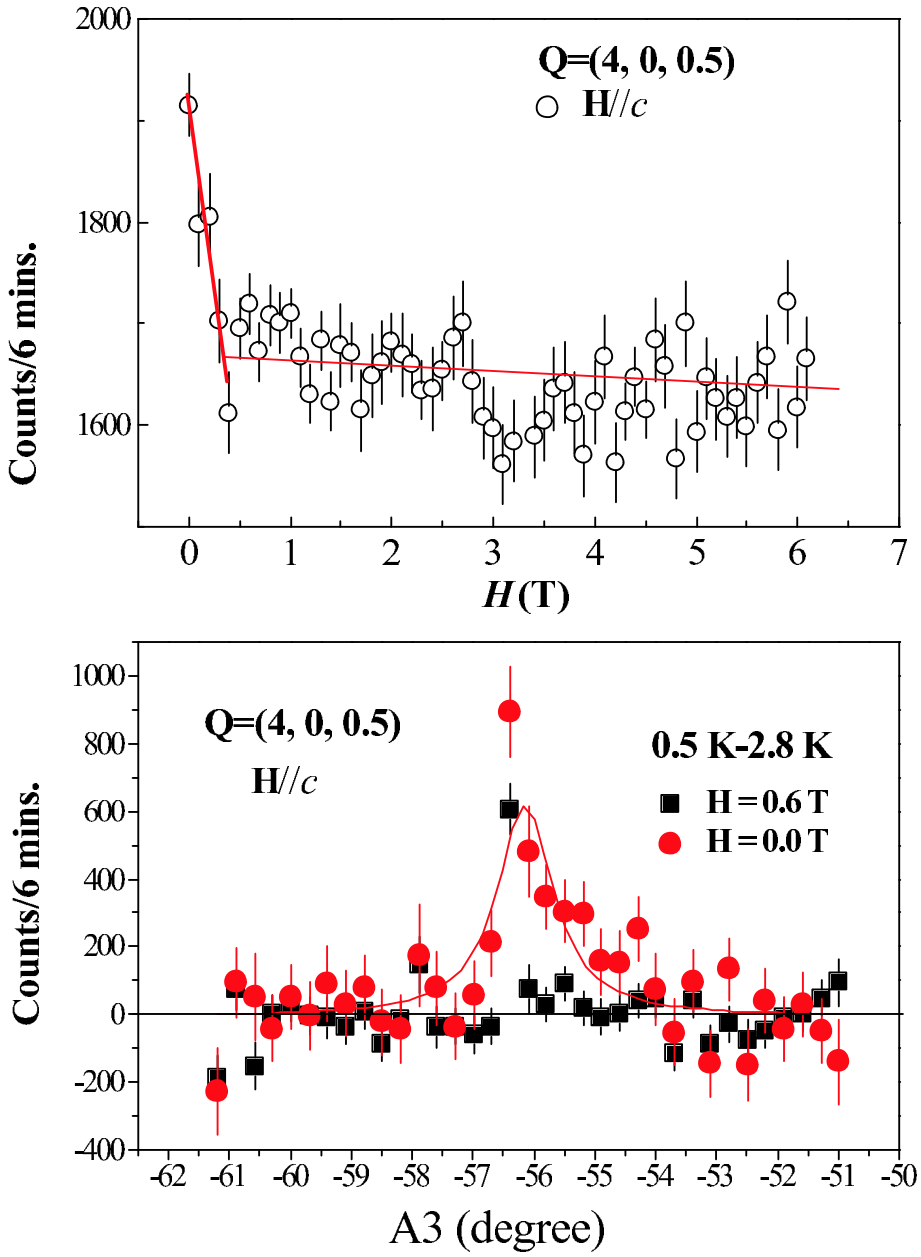

Figure 7.11: (a) The field dependence of the intensity of (4,0,0.5) peak when $H//c$. (b) The rocking scans of the (4,0,0.5) peak at $H = 0$ and $H = 0.6T$.

of Pr^{3+} magnetic moment at CEF level crossing that gives rise to the change of magnetic Bragg intensities. As mentioned above, the first CEF ES lies only 0.4 meV above the triplet GS. As introduced in Chapter 6, we have measured the Zeeman effect on the CEF levels for high fields ($4\ T < H < 11\ T$) on SPINS. As shown in the inset of fig. 6.6 in chapter 6, the first excited state at 0.4 meV shifts toward higher energies as the applied field increases. However the field-dependent transition energy is linear only at higher fields (between 4 T and 11 T). The field-splitting of the ground state multiplet would results in level crossing between the $\Gamma_4^{(2)}$ and the Γ_1 singlet. However, the $PrOs_4As_{12}$ system is complicated by the near degeneracy of the ground state and 1st excited state, which mix strongly under an applied field. With additional level repulsion between different states [145], this leads to a more complicated spectrum of low-lying states, with several low-field level crossings and neutron scattering intensities that are also modified by their field-induced level crossing.

In summary, we have determined the magnetic structure and spin orientation of the antiferromagnetically ordered FS compound $PrOs_4As_{12}$ using neutron scattering with powder and co-aligned single crystals. The magnetic structure is A-type, where the magnetic unit cell doubles the nuclear one along one-axis (say c-axis) with Pr^{3+} spins point to opposite directions with their neighbors in this direction. All spins lie in the doubling-axis (c-) direction. When external magnetic field is applied perpendicular to the Pr^{3+} moment ($H//[1,\bar{1},0]$ and $H//[0,1,0]$), the intensities of magnetic peaks first become enhanced before completely suppressed at the critical field of $H_C = 1.5\ T$ and $H_C = 1.2\ T$ respectively. The AFM order is easier to suppress when field is along the Pr^{3+} moment with $H_C = 0.6\ T$. The Zeeman effect that causes the low-lying CEF level crossing may be responsible for the field dependence of the $PrOs_4As_{12}$ compound.

Conclusions

The interplay between ferromagnetically ordered metallic state and the co-operatively ordered (charge, orbital and spins) insulating state in doped perovskite manganites is essential to the CMR effect. It has been shown that aligning spins by magnetic field or spontaneous magnetic order results in the metal-to-insulator transition [146–148]. In comparison to the well-studied FM metallic state, the complex relations among charge, orbital, spin and lattice in the insulating state is less understood. As hole concentration approaches half-doping, a delicately balanced phase, the CE-phase, is formed. This seemingly stable phase can transit to a good variety of other phases (such as FM, A-,C- and G-type AFM) as doping or ionic size changes. Therefore studying the evolution of the CE-phase should provide valuable insight into the nature of the phase-competition that is responsible for the CMR effect.

$Pr_{1-x}Ca_{1+x}MnO_4$ (PCMO) is orthorhombic, as opposed to tetragonal for $La_{1-x}Sr_{1+x}MnO_4$ (LSMO). The intrinsic orthorhombicity in the single-layered PCMO, together with small $A_{1-x}A'_{1+x}$ ionic radius, gives rise to some unique characteristics that have not been observed in any other manganites. First, in half-doped PCMO a strong spin-lattice coupling is established near T_N, which competes with and suppresses the orthorhombic strain induced by $CO-OO$. Second, in the under-doped PCMOs ($x < 0.5$), a coexistence of commensurate (CM) and incommensurate (ICM) magnetic fluctuations has been discovered. Third, corresponding to the CM and ICM magnetic reflections, two types of magnetic excitations, a dispersive magnon and a localized excitation, have been observed in the nearly half-doped PCMO ($x = 0.45$). By studying the structural and dynamic properties of the half- and under-doped PCMO, we are able to follow the evolution of a typical CE-phase as concentration of carriers changes.

In half-doped PCMO on cooling, the system enters the charge- and orbital-ordered state near $T_{CO} = 300K$, then the checkerboard-like AF order is established below $T_N = 130K$. The charge, orbital and spin ordering in PCMO is very similar to that of LSMO. However the c-axis static correlation in PCMO is long-ranged in contrast to the short-range c-axis correlation in LSMO [37]. It seems the orthorhombic strain promotes 3-dimensional order in PCMO. As the system enter CO/OO, the orthorhombicity shows an abrupt increase. At temperature above T_N but below T_{CO}, the appearance of short-range AF spin correlations suppresses the CO/OO induced orthorhombic strain. It is still unclear why the spin-lattice coupling is particularly strong in PCMO. Our speculation is that the small Pr/Ca ionic sizes and the resultant greater distortion enhance the AF exchange coupling between the FM zig-zag chain, making the overall magnetic exchange coupling more isotropic which favors a more tetragonal CE structure.

As extra electrons ($x < 0.5$) are introduced in the prefect CE-phase, the characteristic wavevectors associated with the CE-type AF order retain. The long-range AF correlations in the $x = 0.5$ system are suppressed though. What is remarkable is the appearance of additional ICM magnetic scattering near the generic CE-AF peak positions. The magnetic nature of these scatterings have been confirmed by their Q- and T-dependence. The incommensurability δ, defined as the distance from the ICM peaks to their corresponding CM peaks, shows obvious doping-dependence.

In the underdoped PCMO systems, perfect CE-arrangement is broken into patches of smaller CE-domains in two directions: along horizontal direction and along the zig-zag chain direction. The resultant CE patches (or domains) contribute to the conventional CE-AF reflections, while the correlations between the CE domains bring about the ICM scatterings. The excess electrons congregate at the domain boundary and form another electric phase. We provide 3 pieces of evidence to support the above drawn picture. First, Fourier transformation successfully reproduces the observed peaks. Second, the temperature dependence measurements with different neutron resolutions reveals glassy feature for both CM and ICM sites, which is consistent with the phase separation scenario. Last but not least, our inelastic neutron measurements show two types of magnetic excitations in the slightly underdoped PCMO ($x = 0.45$): one dispersive magnon that bears a great resemblance to that of the half-doped PCMO and the other localized excitation at $\sim$1

meV. The magnon in the $x = 0.45$ system, obviously originating from the CE-clusters, exhibits linewidth broadening and noticeable softening at the magnetic zone boundary. The localized mode appears only on the ICM side and its intensity increases as the wave vector approaches the ICM peak positions. We argue that the localized mode is the result of domain wall mobility because of its absence in the PCMO $x = 0.35$ system.

Inelastic neutron scattering (INS) is an ideal tool to study the crystal electric field (CEF) levels because it probes both the eigenvalues through transition energies and eigenfunctions through transition intensities. Studies of CEF potential in iron oxypnictides and filled skutterudite with two different approaches were also presented.

We studied the CEF excitations of Ce^{3+} in $CeFeAsO_{1-x}F_x(x = 0, 0.16)$ and analyzed the data with the 'Stevens operator equivalents' approach. For nonsuperconducting CeFeAsO, the Ce CEF levels have three magnetic doublets in the paramagnetic state, but these doublets split into six singlets when Fe ions order antiferromagnetically. For superconducting $CeFeAsO_{0.84}F_{0.16}$ ($T_c = 41$ K), where the static AF order is suppressed, the Ce CEF levels have three magnetic doublets at $\hbar\omega = 0, 18.7, 58.4$ meV at all temperatures. Careful measurements of the intrinsic linewidth Γ and the peak position of the 18.7 meV mode reveal clear anomaly at T_c, consistent with a strong enhancement of local magnetic susceptibility $\chi''(\hbar\omega)$ below T_c. These results suggest that CEF excitations in the rare-earth oxypnictides can be used as a probe of spin dynamics in the nearby FeAs planes.

The filled skutterudite compounds (RT_4X_{12}) exhibit remarkable variety of interesting physical phenomenon. Owing to their unique structure, a subtle modification on composition can result in a completely different CEF scheme, which can reveal the microscopic origin of many electronic and magnetic ordering properties. Although the traditional Steve's Operator Equivalent method simplifies the calculations, its output parameters do not carry straightforward physical insights. Therefore in the study of CEF schemes in $PrOs_4As_{12}$, we introduced a new computational approach. It not only combines sublattices of different point groups, but also quantitatively analyzes the contribution to the CEF potential from each. The Pr^{3+} CEF levels are identified and the ground state is determined to be a magnetic $\Gamma_4^{(2)}$ triplet. The excited states Γ_1, $\Gamma_4^{(1)}$ and Γ_{23} are at 0.4, 13 and 23 meV, respectively. Our results reveal that the ratio b in the As rectangular positions and the g4/g6 ratio determined the magnetic ground state of $PrOs_4As_{12}$, in contrast to the nonmagnetic

ground state of $PrOs_4Sb_{12}$. Extending our approach to other Pr-based filled compounds means that we might be able to determine the ground state of a system by accurately determination its atomic structure, and using 1st principle atomic physics calculation to determine the g4/g6 ratio.

A great effort has been made to assemble a single crystal array, which was used to study the magnetic structure and field-induced phase transition. The magnetic structure is *A*-type with moment lying in the doubling-axis (*c*-) direction. When external magnetic field is applied perpendicular to the Pr^{3+} moment ($H//[1,\bar{1},0]$ and $H//[0,1,0]$), the intensities of magnetic peaks first become enhanced before completely suppressed at the critical field of $H_C = 1.5\ T$ and $H_C = 1.2\ T$ respectively. The AFM order is easier to suppress when field is along the Pr^{3+} moment with $H_C = 0.6\ T$. The Zeeman effect that causes the low-lying CEF level crossing may be responsible for the field dependence of the $PrOs_4As_{12}$ compound.

Bibliography

Bibliography

[1] R. M. Kusters *et. el*, Physica (Amsterdam) **155B**, 362 (1989).

[2] R. von Helmolt *et. el*, Phys. Rev. Lett. **71**, 2331 (1993).

[3] S. Jin *et. al*, Science, **264** 413 (1994).

[4] G. C. Xiong *et. al*, Appl. Phys. Lett. **67**, 3031 (1995).

[5] H. Y. Hwang *et. al*, Phys. Rev. B **52**, 15046 (1995).

[6] G. M. Jonker *et. al*, Physica (Utrecht) **16**, 337 (1950).

[7] A. J. Millis, Nature (London) **392**, 147 (1998).

[8] A. J. Millis *et. al*, Phys. Rev. Lett. **74**, 5144 (1995).

[9] C. Zener *et. al*, Phys. Rev. **82**, 403 (1951).

[10] P. W. Anderson and H. Hasegawa: Phys. Rev. **100**, 675 (1955).

[11] M. B. Salamon *et. al*, Rev. Mod. Phys. **73**, 583 (2001).

[12] Y. Tokura *et. al*, J. Magn. Magn. Mater. **200**, 1 (1999).

[13] M. B. Maple *et. al*, J. Phys. Soc. Jpn. **71**, Suppl., 23 (2002).

[14] H Sato, *et. al*, Phys. Rev. B **62**, 15125 (2002).

[15] N. Takeda *et. al*, J. Phys. So. Jpn. **69**, 868 (2000).

[16] I. Shirotani *et. al*, Phys. Rev. B **56**, 7866 (1997).

[17] E.D.Bauer *et. al*, Phys. Rev. B **65**, 100506 (2002).

[18] M. B. Maple *et. al*, J. Magn. Magn. Mater. **310**, 182 (2007).

[19] H. Sugawara *et. al*, Phys. Rev. B **66** 220504 (2002).

[20] K. Kuwahara *et. al*, J. Phys. Soc. Jpn. **73**, 1438 (2004).

[21] E. A. Goremychkin *et. al*, Phys. Rev. Lett. **93**, 157003 (2004).

[22] K. Kuwahara, K. Iwasa, M. Kohgi, K. Kaneko, S. Araki, N. Metoki, H. Sugawara, Y. Aoki and H. Sato, J. Phys. Soc. Jpn. **73**, 1438 (2004).

[23] K. Kuwahara, K. Iwasa, M. Kohgi, K. Kaneko, N. Metoki, S. Raymond, M. -A. Méasson, J. Flouquet, H. Sugawara, Y. Aoki, and H. Sato, Phys. Rev. Lett. **95**, 107003 (2005).

[24] Y. Aoki, T. Namiki, S. Ohsaki, S. R. Saha, H. Sugawara, and H. Sato, J. Phys. Soc. Jpn.**71**, 2098 (2002).

[25] Y. Kamihara *et. al*, J. Am. Chem. Soc. **130**, 3296 (2008).

[26] C. de la Cruz, Q. Huang, J. W. Lynn, J. Li, W. Ratcliff II, J. L. Zarestky, H. A. Mook, G. F. Chen, J. L. Luo, N. L. Wang, and P. Dai, Nature **453**, 899 (2008).

[27] X. H. Chen, T. Wu, G. Wu, R. H. Liu, H. Chen, and D. F. Fang, Nature (London) **453**, 761 (2008).

[28] G. F. Chen *et al.*, Phys. Rev. Lett. **100**, 247002 (2008).

[29] Zhi-An Ren *et al.*, Europhys. Lett. **83**, 17002 (2008).

[30] J. Zhao *et. al*, Nature Material, Published online: 26 October 2008.

[31] T. Sato *et. al*, J. Phys. Soc. Jpn. **77**, 063708 (2008).

[32] H. Q. Yuan *et. al*, arXiv:0807.3137.

[33] M. Rotter *et. al*, Phys. Rev. Lett. 101, 107007 (2008).

[34] Y. Mizuguchi *et. al*, arXiv:0807.4315.

[35] Y. Moritomo, A. Asamitsu, H. Kuwahara, and Y. Tokura, Nature (London) **380**, 141 (1996)

[36] H. Y. Hwang S-W. Cheong, P. G. Radaelli, M. Marezio, and B. Batlogg, Phys. Rev. Lett. **75**, 914 (1995).

[37] B. J. Sternlieb, J. P. Hill, U. C. Wildgruber, G. M. Luke, B. Nachumi, Y. Moritomo, and Y. Tokura, Phys. Rev. Lett. **76**, 2169 (1996).

[38] Y. Murakami, H. Kawada, H. Kawada, M. Tanaka, T. Arima, Y. Moritomo, and Y. Tokura, Phys. Rev. Lett. **80**, 1932 (1998)

[39] Z. Jirak et al., J. Magn. Mat. **53**, 153 (1985).

[40] D. Senff, F. Krüger, S. Scheidl, M. Benomar, Y. Sidis, F. Demmel, and M. Braden, Phys. Rev. Lett. **96**, 257201 (2006).

[41] A. daoud-Aladine *et. al*, Phys. Rev. Lett. **89**, 097205 (2002).

[42] M. Imada, A. Fujimori, and Y. Tokura, Rev. Mod. Phys. **70**, 1039 (1998).

[43] J. M. Tranquada, B. J. Sternlieb, J. D. Axe, Y. Nakamura,and S. Uchida, Nature **375**, 561 (1995).

[44] M. Fujita, H. Goka, K. Yamada, J. M. Tranquada, and L. P. Regnault, Phys. Rev. B **70**, 104517 (2004).

[45] E. O. Wollan and W. C. Koehler, Phys. Rev. **100**, 545 (1955).

[46] J. B. Goodenough, Phys. Rev. **100**, 564 (1955).

[47] P. Dai, Jiandi Zhang, H. A. Mook, S.-H. Liou, P. A. Dowben, and E. W. Plummer, (1996) *Phys. Rev. B* **54**, R3694.

[48] P. G. Radaelli, D. E. Cox, M. Marezio, and S-W. Cheong, (1997) Phys. Review B **55**, 3015.

[49] Z. Jirák, S. Krupicka, Z. Simsa, M. Dlouha, and S. Vratislav, J. Magn. Magn. Mater. **53**, 153 (1985).

[50] A. Daoud-Aladine, J. Rodriguez-Carvajal, L. Pinsard-Gaudart, M. T. Fernandez-Diaz, and A. Revcolevschi, Phys. Rev. Lett. **89**, 097205 (2002).

[51] F. Ye, J. A. Fernandez-Baca, Pengcheng Dai, J. W. Lynn, H. Kawano-Furukawa, H. Yoshizawa, Y. Tomioka, and Y. Tokura, Phys. Rev. B **72**, 212404 (2005).

[52] S. Larochelle, A. Mehta, L. Lu, P. K. Mang, O. P. Vajk, N. Kaneko, J. W. Lynn, L. Zhou, and M. Greven, Phys. Rev. B **71**, 024435 (2005).

[53] I. V. Solovyev and K. Terakura, Phys. Rev. Lett. **83**, 2825 (1999).

[54] J. van den Brink, G. Khaliullin, and D. Khomskii, Phys. Rev. Lett. **83**, 5119 (1999).

[55] S. Yunoki, T. Hotta, and E. Dagotto, Phys. Rev. Lett. **84**, 3714 (2000).

[56] T. Mutou and H. Kontani, Phys. Rev. Lett. **83**, 3685 (1999).

[57] D. Khomskii and J. van den Brink, Phys. Rev. Lett. **85**, 3329 (2000).

[58] Y. Murakami, H. Kawada, H.Kawata, M. Tanaka, T. Arima, Y. Moritomo, and Y. Tokura, Phys. Rev. Lett. **80**, 1932 (1998).

[59] S. S. Dhesi, A. Mirone, C. De Nadai, P. Ohresser, P. Bencok, N. B. Brookes, P. Reutler, A. Revcolevschi, A. Ragliaferri, O. Toulemonde, and G. van der Laan, Phys. Rev. Lett. **92**, 056403 (2004).

[60] Y. Tokura, Rep. Prog. Phys. **69**, 797 (2006).

[61] The average A-site ionic radius for LSMO is $r_{ave} = 1.2865$ Å, while it is $r_{ave} = 1.1798$ Å for PCMO. This is a rather large reduction.

[62] M. Ibarra, R. Retoux, M. Hervieu, C. Autret, A. Maignan, C. Martin, and B. Raveau, J. Solid State Chem. **170**, 361 (2003).

[63] R. Mathieu and Y. Tokura, J. Phys. Soc. Japan **76**, 124706 (2007).

[64] T. Kimura, R. Kumai, Y. Tokura, J. Q. Li, and Y. Matsui, Phys. Rev. B **58**, 11081 (1998).

[65] D. N. Argyriou, H. N. Bordallo, B. J. Campbell, A. K. Cheetham, D. E. Cox, J. S. Gardner, K. Hanif, A. dos Santos, and G. F. Strouse, Phys. Rev. B **61**, 15269 (2000).

[66] D. Senff *et al.*, Phys. Rev. Lett. **96**, 257201 (2006).

[67] The exchange coupling constants are obtained based on the Hamiltonian similar as that reported in Ref. [66], F. Ye, Songxue Chi, J. A. Fernandez-Baca, J. W. Lynn, Y.Kaneko, Roland Mathieu, Y. Tokura, and Pengcheng Dai, (unpublished).

[68] R. Kajimoto *et al.*, Phys. Rev. B **66** 180402(R) (2002).

[69] T. G. Perring *et al.*, Phys. Rev. Lett. **77**, 711 (1996).

[70] H. Y. Hwang *et al.*, Phys. Rev. Lett. **80**, 1316 (1998).

[71] M. Coey, Nature (London) **430**, 155 (2004).

[72] S. Grenier *et al.*, Phys. Rev. B **69**, 134419 (2004).

[73] Y. S. Lee *et al.*, Phys. Rev. B **75**, 14407 (2007).

[74] C. H. Chen *et al.*, Phys. Rev. Lett. **83**, 4792 (1999).

[75] M. Zimmermann *et al.*, Phys. Rev. B **64**, 195133 (2001).

[76] S. Larochelle *et al.*, Phys. Rev. Lett. **87**, 095502 (2001).

[77] J. Brink *et al.*, Phys. Rev. Lett. **83**, 5118 (1999).

[78] K. Rościszewski *et al.*, J. Phys. Condens. Matter **19** 186223 (2007).

[79] Songxue Chi *et al.* PNAS **104**, 10796 (2007).

[80] A. Moreo, S. Yunoki, and E. Dagotto, Science **283**, 2034, (1999).

[81] J. Burgy, A. Moreo, and E. Dagotto Phys. Rev. Lett. **92**, 097202, (2004).

[82] E. Dagotto, Science **309**, 257, (2005).

[83] Y. Tomioka A. Asamitsu, H. Kuwahara, Y. Moritomo, and Y. Tokura, Phys. Rev. B **53**, R1689 (1996).

[84] G. C. Milward, M. J. Calderon, and P. B. Littlewood, Nature **433**, 607 (2005).

[85] A. Daoud-Aladine, J. Rodríguez-Carvajal, L. Pinsard-Gaudart, M. T. Fernández-Díaz, and A. Revcolevschi, Phys. Rev. Lett. **89**, 097205 (2002).

[86] V. Ferrari, M. Towler, and P. B. Littlewood, Phys. Rev. Lett. **91**, 227202 (2003).

[87] G. Zheng and C. H. Patterson, Phys. Rev. B **67**, 220404 (2003).

[88] D. V. Efremov, J. Van Den Brink, and D. I. Khomskii, Nature Materials **3**, 853 (2004).

[89] J. C. Loudon, S. Cox, A. J. Williams, J. P. Attfiled, P. B. Littlewood, P. A. Midgley, and N. D. Mathur, Phys. Rev. Lett. **94**, 097202 (2005).

[90] Explain why sdw would produce the symmetric saellite peaks with same spectral weight.

[91] J. M. Tranquada, B. J. Sternlleb, J. D. Axe, Y. Nakamura, and S. Uchida, Nature **375**, 561, (1995).

[92] T. Hotta, Adrian Feiguin, and E. Dagotto, Phys. Rev. Lett. **86** 4922, (2001).

[93] T. Hotta, Reports on Progress in Phyiscs **69** 2061, (2006).

[94] G. Alvarez, H. Aliaga, C. Sen, and E. Dagotto, Phys. Rev. B **73** 224426, (2006).

[95] S. Larochelle, A. Mehta, N. Kaneko, P. K. Mang, A. F. Panchula, L. Zhou, J. Arthur, and M. Greven, Phys. Rev. Lett. **87**, 095502 (2002).

[96] T. V. Ramakrishnan *el al*, Phys. Rev. Lett. **92**, 157203 (2004).

[97] O. Cépas *et al.*, Phys. Rev. B **73** 035218 (2006).

[98] G. Milward *et al.*, Nature (London) **433**, 607 (2005).

[99] L. Brey *et al.*, Phys. Rev. Lett. **95** 117205 (2005).

[100] T. Hotta *et al.*, Phys. Rev. Lett. **84** 2477 (2000).

[101] Songxue Chi *et al.*, Proc. Natl. Acad. Sci. **104**, 10796 (2007).

[102] B. J. Sternlieb *et al.*, Phys. Rev. Lett. **76**, 2169 (1996).

[103] F. Ye *et al.*, elastic $x < 0.5$, to be published (2008).

[104] F. Ye *et al.*, inelastic $x = 0.5$, to be published (2008).

[105] R. Mathieu *et al.*, EPL **80** 37001 (2007).

[106] Y. Kamihara, T. Watanabe, M. Hirano, and H. Hosono, J. Am. Chem. Soc. **130**, 3296 (2008).

[107] H. H. Wen *et al.*, Europhys. Lett. **82**, 17009 (2008).

[108] C. de la Cruz *et al.*, Nature (London) **453**, 899 (2008).

[109] J. Zhao *et al.,* arxiv.org/abs/0806.2528.

[110] M. A. McGuire *et al.* arxiv.org/abs/0806.3878.

[111] Y. Chen *et al.*, arxiv.org/abs/0807.0662.

[112] Q. Huang *et al.*, arxiv.org/abs/0806.2776.

[113] P. Fulde and M. Loewenhaupt, Advances in Phys. **34**, 589 (1986).

[114] J. Moset and A. Furrer, Journal of Superconductivity **10**, 623 (1997).

[115] Stevens K. W. H., Proc. Phys. Soc. Lond. **A65**, 209 (1952).

[116] M. T. Hutchings, Solid state Physics, Vol. 16, eds F. Seitz and D. Turnbull (Academic, NY) p. 227 (1964)

[117] R. J. Birgeneau, J. Phys. Chem. Solids **33**, 59 (1972).

[118] T. Yildirim (unpublished)

[119] R. Osborn and E. A. Goremychkin, Physica C **185-189**, 1179 (1991).

[120] A. T Boothroyd *et al.*, Phys. Rev. Lett. **77**, 1600 (1996).

[121] J. Mesot, G. Böttger, H. Mutka, and A. Furrer, Europhys. Lett. **44**, 498 (1998).

[122] R. Bewley *et al.*, Physica B **385-386**, 1029 (2006).

[123] T. J. Udovic *et al.*, Nucl. Instr. Meth. **A517**, 189 (2004).

[124] A. D. Christianson *et al.*, arxiv.org/abs/0807.3932.

[125] G. S. Nolas and G. Fowler, Ann. Rev. Mater. Sci. **29**, 89 (1999).

[126] B. C. Sales, in *Handbook on the Physics and Chemistry of Rare Earths*, Vol 33, Ch. 211, pp.1-34. (eds. K. A. Gschneidner, Jr., J.-C. G. Bünzli and V. K. Pecharsky) (Elsevier Science, 2003).

[127] B. C. Chakoumakos and B. C. Sales, J. Alloys and Compounds **407**, 87 (2006).

[128] Y. Aoki, T. Namiki, T. D. Matsuda, K. Abe, H. Sugawara, and H. Sato, Phys. Rev. B **65**, 064446 (2002).

[129] C. Sekine, T. Uchiumi, I. Shirotani, and T. Yagi, Phys. Rev. Lett. **79**, 3218 (1997).

[130] M. Matsunami, L. Chen, H. Okamura, T. Nanba, C. Sekine and I. Shirotani, J. Magn. Magn. Mater. **272-276**, E39 (2004).

[131] M. Yogi, H. Kotegawa, Y. Imamura, G. -q. Zheng, Y. Kitaoka, H. Sugawara, and H. Sato, Phys. Rev. B **67** 180501 (2003).

[132] E. D. Bauer, N. A. Frederick, P. -C. Ho, V. S. Zapf, and M. B. Maple, Phys. Rev. B **65** 100506(R) (2002).

[133] M. B. Maple, E. D. Bauer, V. S. Zapf, E. J. Freeman, N. A. Frederick and R. P. Dickey, Acta Phys. Pol. B **32**, 3291 (2001).

[134] E. D. Bauer, St. Berger, Ch. Paul, M. Della Mea, G. Hilscher, H. Michor, M. Reissner, W. Steiner, A. Grytsiv, P. Rogl, and E. W. Scheidt, Phys. Rev. B **66**, 214421 (2002).

[135] N. P. Butch, W. M. Yuhasz, P. -C. Ho, J. R. Jeffries, N. A. Frederick, T. A. Sayles, X. G. Zheng, M. B. Maple, J. B. Betts, A. H. Lacerda, F. M. Woodward, J. W. Lynn, P. Rogl, and G. Giester, Phys. Rev. B **71**, 214417 (2005).

[136] W. M. Yuhasz, N. P. Butch, T. A. Sayles, P. -C. Ho, J. R. Jeffries, T. Yanagisawa, N. A. Frederick, M. B. Maple, Z. Henkie, A. Pietraszko, S. K. McCall, M. W. McElfresh, and M. J. Fluss, Phys. Rev. B **73**, 144409 (2006).

[137] M. B. Maple, N. P. Butch, N. A. Frederick, P. -C. Ho, J. R. Jeffries, T. A. Sayles, T. Yanagisawa, W. M. Yuhasz, Songxue Chi, H. J. Kang, J. W. Lynn, Pengcheng Dai, S. K. McCall, M. W. McElfresh, M. J. Fluss, Z. Henkie, and A. Pietraszko, PNAS **103**, 6783 (2006).

[138] D. T. Adroja, J. -G. Park, E. A. Goremychkin, N. Takeda, M. Ishikawa, K. A. McEwen, R. Osborn, A. D. Hillier, and B. D. Rainford, Physica B **359-361**, 983 (2005).

[139] D. L. Cox and A. Zawakowski, Adv. Phys. **47**, 599 (1998).

[140] Pei-chun Ho, J. Singleton, M. B. Maple, H. Harima, P. A. Goddard, Z. Henkie, and A. Pietraszko, New J. Phys. **9**, 269 (2007).

[141] S. D. Wilson, Pengcheng Dai, D. T. Adroja, S. -H. Chung, J. W. Lynn, N. P. Butch, and M. B. Maple, Phys. Rev. Lett. **94**, 056402 (2005).

[142] K. Takegahara, J. Phys. Soc. Jpn. **69**, 1572 (2000).

[143] K. Takegahara, H. Harima, and A. Yanase, J. Phys. Soc. Jpn. **70**, 1190 (2001).

[144] K. R. Lea, M. J. M. Leask, and W. P. Wolf, J. Phys. Chem. Solids **23**, 1381 (1962).

[145] Y. Kuramoto, J. Otsuki, A. Kiss and H. Kusunose, Progress of Theoretical Physics Supplement No 160, (2005).

[146] C. P. Adams *et al.*, Phys. Rev. Lett. **85**, 3954 (2000).

[147] S. Shimomura *et al.*, Phys. Rev. Lett. **83**, 4389 (1999).

[148] F. M. Woodward *et al.*, Phys. Rev. B **70**, 174433 (2004).

Vita

Songxue was born on Febuary 5, 1972 and raised in Suihua, Heilongjiang Province, China. In the summer of 1993, he completed his undergraduate career at Yanbian University (China) with a B.S. in Physics. He studied in the Pukyong National University (South Korea) from 1999 to 2001 and received his M.S. in Physics. He matriculated at the University of Tennessee in the fall of 2003 and graduated with the degree of Doctor of Philosophy in experimental Condensed Matter Physics in the fall of 2008. During the rest of his time when he was not a student, he was a teacher. He taught in Yanbian University for nearly four years and Swaneng Hill School, a Botswana high school, for more than 2 years.